Towards Photocatalytic Overall Water Splitting via Small Organic Shuttles

Jacob Sommers

April 20, 2016

Thesis submitted to the

Faculty of Graduate and Postdoctoral Studies

University of Ottawa

For MSc degree in chemistry

Faculty of Science

Ottawa-Carleton Chemistry Institute

Abstract

This thesis studies the development of a new method for photochemical overall water splitting using a small organic shuttle.

In Section 2, $BiVO_4$, was studied to determine the CO_2 reduction mechanism and how catalytic activity decays. $BiVO_4$ catalysts were capable of producing a maximum of 200 μmol of methanol per gram of catalyst from CO_2 in basic media, and later decomposed by $BiVO_4$. The decay of $BiVO_4$ was studied by x-ray diffraction and scanning electron microscopy, demonstrating reversible decomposition of $BiVO_4$. $BiVO_4$ is etched, leeching vanadium into solution, while nanoparticles of bismuth oxide are deposited on the surface of $BiVO_4$.

In Section 3, ferrocyanide salts, an aqueous, cheap, and abundant photocatalyst was used for the first time to dehydrogenate aqueous formaldehyde selectively into formate and hydrogen. The catalyst is capable of record turnovers and turnover frequencies for formaldehyde dehydrogenation catalysts. A preliminary mechanism was proposed from experimental and computational data.

Acknowledgements

First, I would like to acknowledge my supervisor, Dr. Sandro Gambarotta. His guidance, supervision and insight has not only allowed me to produce the data in this thesis, but he helped mould me into the scientist I am. Dr. Gambarotta has provided ample opportunity to hone my technical, critical and communication skills. I am supremely grateful to Dr. Gambarotta for taking me on as a graduate student and encouraging me to take on ambitious and potentially important projects.

Thank you to all of my former supervisors: Christian Prud'homme, Dr. John Arnason, and Dr. Deryn Fogg. Working for each of you propelled my enjoyment of science and guided me towards graduate research. Thank you to the wonderful Dr. Kathy-Sarah Focsaneanu, Dr. Christian Clavette, and Dr. Rashmi Venkateswaran who have helped me become a better TA, and actually enjoy teaching.

I would also like to thank all of my fellow lab mates who have helped guide my scientific career so far. I am very grateful to Dr. Nick Alderman and Camilo Viasus, who have been mentors, friends, and colleagues from the moment we began working together in the Gambarotta lab. I would also like to thank Laura and the super undergrad Christine for helping me with my research and their friendship. I would also like to thank Joanna for helping me get started in my graduate studies, and being a wonderful ambassador for the lab. Thank you to Dr. Justin Lummiss and Carolyn for teaching me how to be a chemist, and all the patience and trust you exhibited with a novice, recent undergrad who had barely done any research. I would also like to thank Bianca, Ben, Gwen, Jen, Ahmed, and Salimah for teaching me so much during my time

alongside you all. I would also like to acknowledge the other wonderful undergraduates, James, Devon, Adrian, and David.

Thank you to all of the staff at uOttawa who's hard work has been undeniably crucial for not only my research but everyone at the university. Through all of the troubleshooting and confusion, it was wonderful and fun to work with Dr. Sharon Curtis on the GC-MS, and then to learn form you in your wonderful class. Thank you to Dr. Yun Liu for your training and support with all of my SEM needs. Thank you Don, Lee and Ian for your advice, assistance and general awesome-ness.

Thank you to my non-lab friends. You are too many to name, but thank you for preserving my sanity and embiggening my somewhat cromulent humor. Sophie, you have supported me through the fun times and the tough times, I cannot thank you enough. Finally, and most importantly, I would like to thank my parents and siblings and all of my wonderful extended family for their ongoing support. I wouldn't have gotten where I am now without any of you. Thank you for always being there for me.

Table of Contents

List of Figures

List of Tables

List of Abbreviations

acac	Acetylacetone
AQY	Apparent quantum yield
bpy	2,2'-Bipyridine
CB	Conduction band
CIGS	$Cu(In_xGa_{1-x})(S_ySe_{1-y})_2$
CTAB	Hexadecyltrimethylammonium bromide
DFT	Density functional theory
DHBP	Dihydroxy-2,2'-bipyrimidine
DMF	Dimethylformamide
dppe	1,1-Bis(diphenylphosphino)ethane
dppm	1,1-Bis(diphenylphosphino)methane
DS	Dye-sensitized
e^-	Electron
EDS	Energy dispersive spectroscopy
E_g	Energy/Band gap
ESR	Electron spin resonance
FA	Formic acid
FID	Flame ionization detector
GC	Gas chromatography
g-C_3N_4	Graphitic carbon nitride
GO	Graphene oxide

h^+	Hole
h-$BiVO_4$	Hyperbranched monoclinic bismuth vanadate
HCOOH	Formic Acid
HEC	Hydrogen evolution catalyst
HER	Hydrogen evolution reaction
HT	Hydrothermal
IMes	1,3-bis(2,4,6-trimethylphenyl)-imidazol-2-ylidene
LOHC	Liquid organic hydrogen carrier
MACHO	Bis[2-(diphenylphosphinoethyl)amine]
m-$BiVO_4$	Monoclinic bismuth vanadate
NHC	*N*-heterocyclic carbene
NMR	Nuclear magnetic resonance
p-$BiVO_4$	Polyhedral monoclinic bismuth vanadate
PC	Polymerizable complex
PC	Propylene carbonate
PCET	Proton-coupled electron transfer
p-FA	Paraformaldehyde
PNN	Tridentate phosphine-amine-amine ligand
PNP	Tridentate phosphine-amine-phosphine ligand
PP_3	Tris[2-(diphenylphosphino)ethyl]phosphine
PSII	Photosystem II
RGO	Reduced graphene oxide

Ru-MACHO	Carbonylchlorohydrido{bis-[2-(diphenylphosphinomethyl)ethyl]amino}ruthenium(II)
Ru-MACHO	Carbonylhydrido(tetrahydroborato){bis-[2-(diphenylphosphinomethyl)ethyl]amino}ruthenium(II)
SEM	Scanning electron microscopy
SHE	Standard hydrogen electrode
SPR	Surface plasmon resonance
SSR	Solid state reaction
STH	Solar-to-hydrogen
TBA	Tetrabutylammonium
TCD	Thermal conductivity detector
THBPM	Tetrahydroxy-2,2'-bipyrimidine
TOF	Turnover frequency
TON	Turnover number
TPPTS	*meta*-Trisulfonated triphenylphosphine
$trop_2dad$	*N,N*-bis(5-*H*-dibenzolo[*a,d*]cycloheptene-5-yl)-1,4-diazabuta-1,3-diene
VB	Valence band
VOC	Volatile organic chemical
WOC	Water oxidation catalyst
XPS	X-ray photoelectron spectroscopy
XRD	X-ray diffraction
ZIF	Zeolitic imidiazole framework

Chapter 1: Introduction

1.1.1 Background

Photocatalytic water splitting to produce hydrogen (and oxygen) is an active area of research focused on providing a renewable fuel, and replacing methane reformation as the major source of industrial hydrogen worldwide.[1–6]

Most approaches to photocatalytic water splitting utilize photosemiconductors to absorb sunlight, and use the photo-generated electron/hole pairs to oxidize and reduce water into O_2 and H_2, respectively. This typically is done using either a single semiconductor, or two separate semiconductors connected via an electron mediator (known as Z-scheme catalysis).

In addition to the production of hydrogen, the storage (and release) of the potential energy source is an active area of research.[7–9] We will explore the current state of the literature for the release of hydrogen from hydrogen dense liquid organic hydrogen carriers (LOHCs), namely methanol, formaldehyde and formic acid. As it will be shown, releasing hydrogen from the above LOHCs often produces CO_2 (or carbonate) along with hydrogen. As a result, we will also explore research into photocatalytically recovering LOHCs from CO_2.[8]

1.1.2 Photosemiconductor Theory

When a photon is absorbed by a semiconducting material, an electron in the highest energy ground state (the valence band, VB) may be excited into the next higher energy excited state (the conducting band, CB). This occurs when the energy of the incident photon is greater than or equal to the energy gap between the VB and the CB (the band gap, E_g).[6] If $h\nu \geq E_g$, an electron (e^-) will be excited into the CB, while a hole (h^+) where the electron previously resided will exist

in the VB. The photoinduced e^-/h^+ pair are now able to perform reduction and oxidation reactions, respectively (Figure 1.1.2.1).

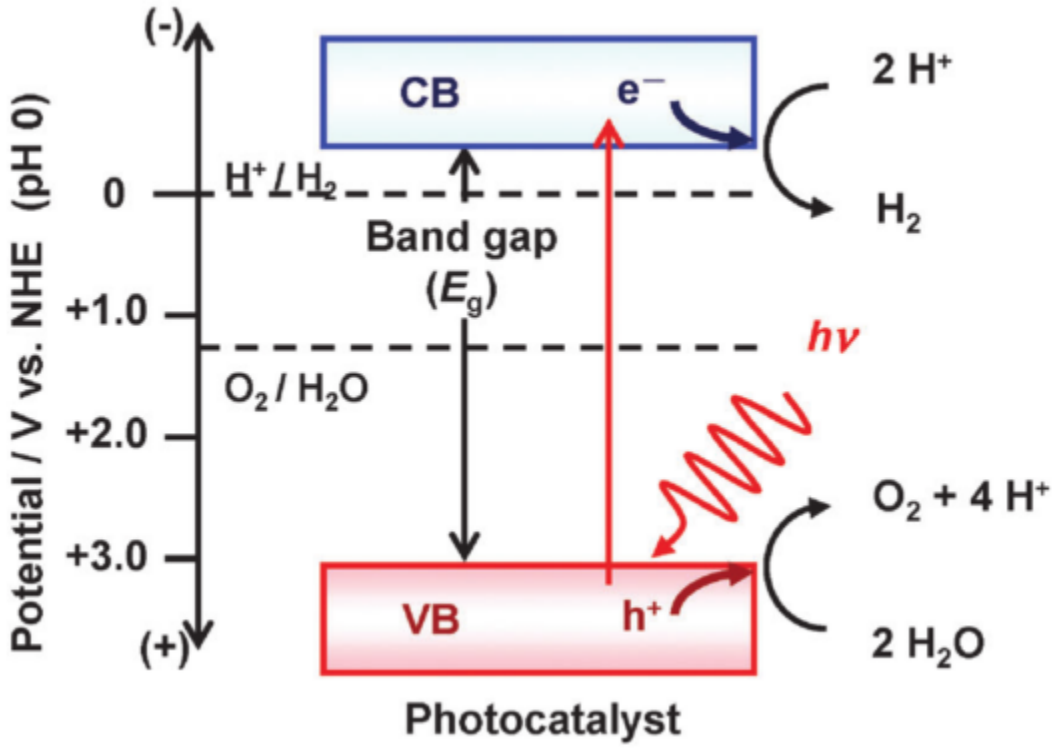

Figure 1.1.2.1. Energy diagram of semiconductor catalysts, highlighting the band gap (E_g) and reduction potentials of hydrogen and water. Reproduced from ref. 4.

When water splitting is targeted, the two redox processes to be performed are proton reduction and oxygen oxidation. As depicted in Figure 1.1.2.1, the CB must be therefore more negative (vs NHE) than the reduction potential of protons (or oxidation potential of H_2, 0.00 eV), while the VB must be more positive than the reduction potential of oxygen (or oxidation potential of water, 1.23 eV). The difference between the reduction and oxidation potentials of water is 1.23 eV, which corresponds to roughly 1000 nm, within the IR region of light. Theoretically, this is the

thermodynamic requirement for water splitting. Many photocatalysts have CBs and VBs which surround the required redox potentials, including those shown in Figure 1.1.2.2.

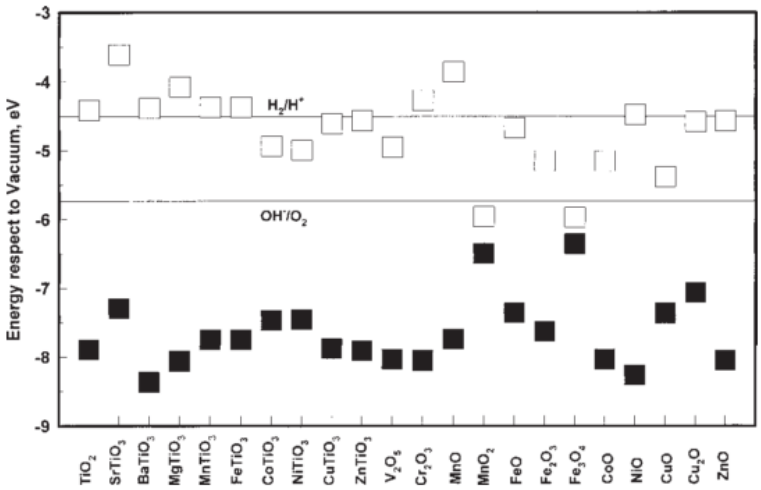

Figure 1.1.2.2. Selection of semiconductors commonly investigated for water splitting applications. Dark squares represent valence band, white squares represent conduction band. Valence bands more negative than the OH^-/O_2 line are capable of water oxidation, while conduction bands more positive (above) than H_2/H^+ band are capable of proton reduction. Reproduced from ref. 10.

However, many other factors may interfere with water splitting, including charge mobility, charge recombination and overpotential. Each of these factors is affected by the nature of the catalyst. Other important factors include the solution pH, and the optional addition of photosensitizers, co-catalysts, and electrolytes.

Charge recombination is the consequence of the semi-random motion of electrons and holes through a material (Figure 1.1.2.3). In an ideal reaction, after a photoexcitation event, both the electron and hole would travel to the nearest surface and undergo a productive redox reaction. Unfortunately, the electron and hole movement is random. The electron/hole pair may recombine

within the bulk of the semiconductor, typically evolving energy under the form of heat and nullifying the photoexcitation. The recombination may also occur on the surface, or with the result of a different photoexcitation. In some semiconductors, the rate of recombination exceeds that of charge mobility, which results in significantly reduced efficiency.

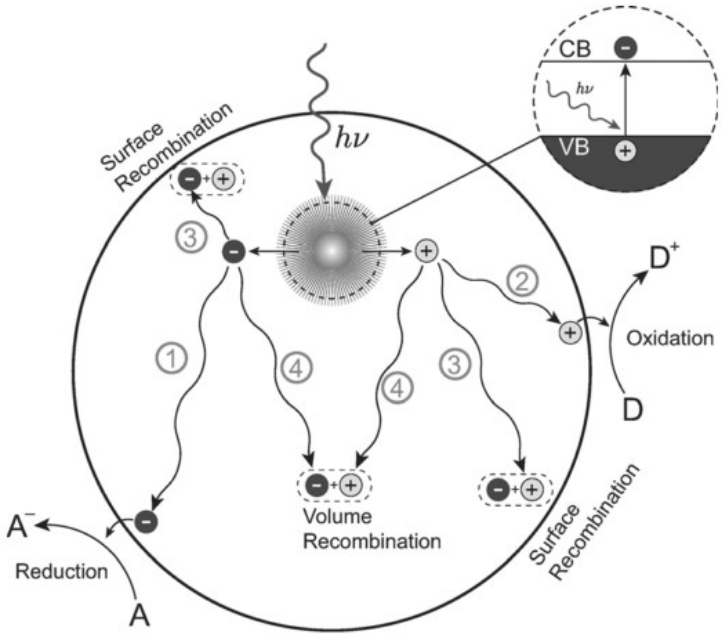

Figure 1.1.2.3. Photogenerated charge separation and mechanisms of catalysis and charge separation. Reproduced from ref. 8.

TiO_2 is the most commonly used photocatalyst for water splitting, due to favorable stability, charge separation, and that it has been well studied. The use of TiO_2 in a photoelectrochemical set-up was the first example of photocatalytic water splitting, by Honda and Fujishima is 1972.[11] For sustainable photocatalytic water splitting, bare TiO2 has a band gap of ~3.2 eV (~385 nm), which makes it weakly absorb, if at all, in the visible region. It should be reminded that the solar spectrum at earth ground level (Figure 1.1.2.4) lies greatly in the visible (and IR) region, with very little natural sunlight capable of exciting bare TiO_2.

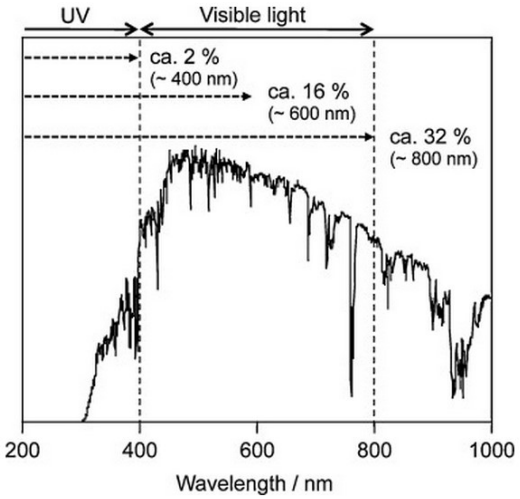

Figure 1.1.2.4. Solar spectrum annotated with the maximum solar efficiency for a semiconductor able to absorb at a given wavelength or lower. Reproduced from ref. 3.

While many other water splitting semiconductors are able to absorb within the visible region (Figure 1.1.2.2), few have the advantages of TiO_2 (stability, mobility, and facile synthesis). Therefore, a great deal of research has focused on the sensitization of TiO_2 in order to improve visible light absorption. One method is to dope TiO_2 with metal ions (e.g. Fe, Mo, V, etc.) in order to introduce a foreign atom which will have either a lower CB than TiO_2, or higher VB (Figure 1.1.2.5).[6]

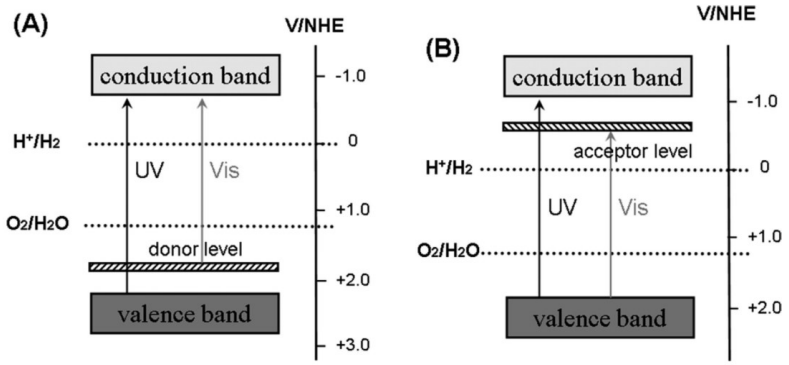

Figure 1.1.2.5. Schematic of metal ion doping of TiO_2 to either raise the VB (A) or lower the CB (B). Reproduced from ref. 6.

Another method to sensitize TiO_2 (or other wide band-gap photocatalysts) is to introduce a photon scavenging dye to the surface of the semiconductor. This dye will inject an excited electron from the dye into the CB of the semiconductor, which will allow for hydrogen reduction (Figure 1.1.2.6). A donor molecule will be required to reduce the dye, but this donor can be recovered by a second catalyst (this will be explored in more detail in section 1.2)

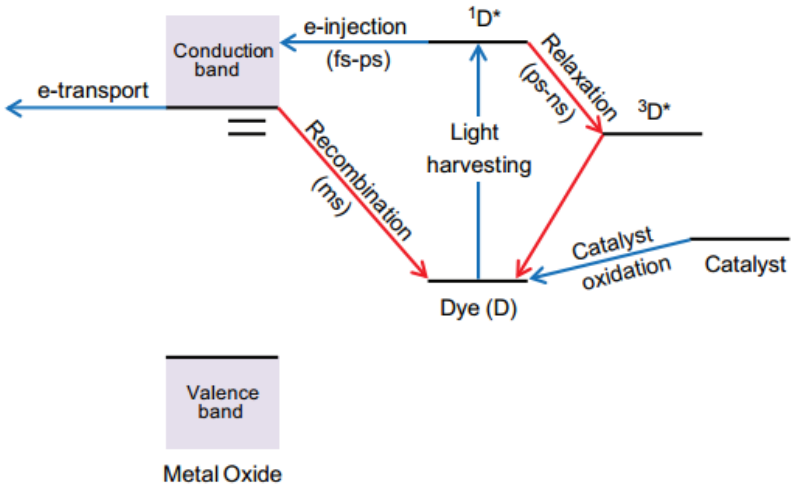

Figure 1.1.2.6. Schematic of electron routes in dye-sensitized metal oxide photocatalysts. Blue lines represent productive electron transport for catalysis. Red lines represent electron deactivation pathways. Reproduced from ref. 1.

The sensitizer can be an organic dye covalently attached to the surface of the semiconductor, or it can be a metal nanoparticle (e.g. Au, Ag), which can sensitize the semiconductor by surface plasmon resonance (SPR). SPR is the resulting effect of metal nanoparticles being excited by photons at their resonant frequency. The excited electrons create an oscillating electric field in the nearby vicinity of the nanoparticles.[12] The resonant frequency is dependent on the metal used as well as nanoparticle shape, size and density of neighboring plasmons.[13]

The mechanism that SPR is able to enhance photocatalysis is currently under debate. Hypothesis include the ability for plasmons to inject electrons into the semiconductor and oxidize water, accept electrons from the semiconductor and reduce water, enhance the probability a photon to stimulate the generation of an electron/hole pair, or enhance electron/hole pair generation near the surface of a semiconductor to reduce charge recombination.[14] While the mechanism is not fully understood, the plasmon induced enhancement of photocatalysis is clear (Figure 1.1.2.7).

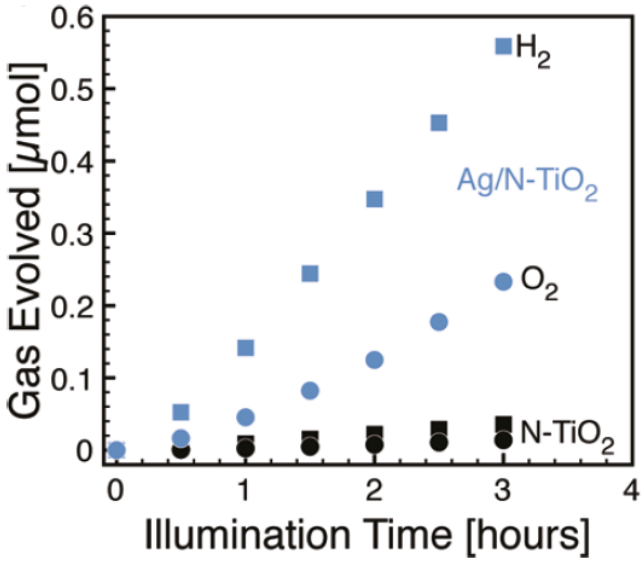

Figure 1.1.2.7. Plasmon (Ag) induced photochemical enhancement of overall water splitting on TiO_2. Reproduced from ref. 15.

Sensitization with a photoactive dye directly bound to the catalyst is well studied. Since the landmark paper from Grätzel, who attached a $Ru(bpy)^{2+}$ derivative to TiO_2, the field of sensitization with Ru complexes has literally exploded.[16] Attempts to increase electron injection, reduce electron recombination, and dye stability have followed, in addition as attempts to move into cheaper organic sensitizers.[17–23]

In order to prevent charge recombination, several strategies are beginning to be employed: adding thin protecting layers on top of the catalyst surface, bulkier electrolytes in reaction solution, and linker molecules between photosensitizers and the catalyst (Figure 1.1.2.8). By depositing very thin layers of amorphous metal oxides on top of the catalyst, charge recombination can be decreased, by separating the bulk of TiO_2 from the dye-localized hole. While the efficiency of electron injection from photosensitizers is reduced, the recombination of electrons is so severely reduced, that conversion efficiencies are still improved by almost 50%.[17] As a bonus, these protecting layers are also capable of reducing the reoxidation of products, and improve stability of the catalyst from being corroded by the electrolyte solution.[18]

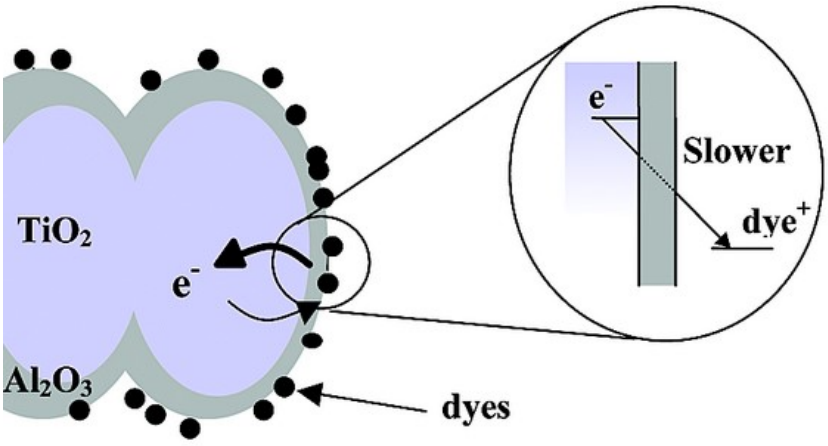

Figure 1.1.2.8. Schematic of reduced electron recombination by introducing thin Al_2O_3 on surface of semiconductor. Reproduced from ref. 17.

A second research area for slowing charge recombination in dye-sensitized solar cells involves modifying the electrolytes in solution. To exclusively study the hydrogen evolution half reaction, researchers add iodide as a sacrificial agent (oxidized to I_3^-). By modifying the counter ion, researchers were able to moderately increase efficiency, while decreasing charge recombination.[19,20] For example, by simply switching from tetraethylammonium iodide to

tetrahexylammonium iodide the quantum efficiency of the H_2 evolution reaction was increased from 7.34% to 8.37%, while increasing electron lifetime. It was proposed that the protection from recombination is due to the bulkier cations blocking I_3^- from coming in close contact with the catalyst, preventing recombination, although this is still being debated.[20]

Recently, researchers have begun to focus on preventing charge recombination in dye-sensitized cells by adding π-conjugated linkers in between the dye and the photocatalyst (Figure 1.1.2.9).[21,22] The purpose of the spacer is to increase the distance between the excited electrons on the semiconductor surface and the photogenerated hole localized on the ruthenium dye. Early results have shown the spacer method as indeed being capable of reducing electron recombination and increasing the catalyst's potential voltage, although these systems have not yet been tested with water splitting reactions to compare quantum yields.

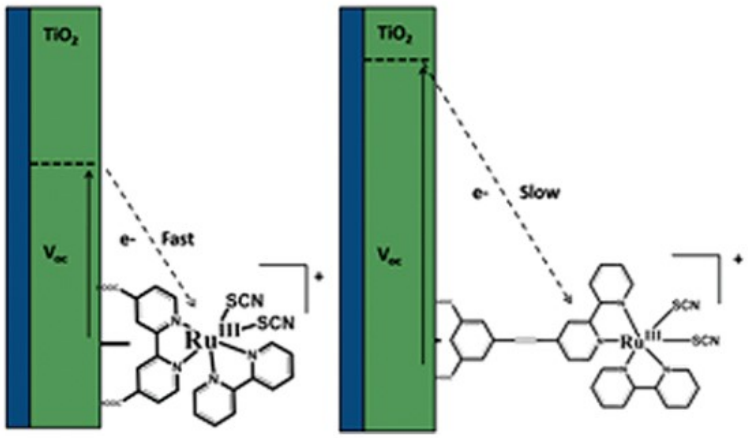

Figure 1.1.2.9. Effect of adding a conjugated spacer between photosensitizer and semiconductor, in order to reduce rate of charge recombination. Reproduced from ref. 22.

In the absence of co-catalysts, most undoped semiconductors are unable to produce hydrogen. However, when a dedicated hydrogen evolution catalyst (e.g. Pt, NiO, MoS_3)[24–26], is deposited on the surface of a semiconductor, hydrogen production is either activated, or greatly improved.

This is caused by a combination of favorable surface chemistry and the ability to trap photoexcited electrons from the semiconductor.[4] Once an electron is transferred to the hydrogen evolution catalyst, it is difficult to recombine with a hole in the semiconductor. Furthermore, the hydrogen evolution catalyst acts as a driving force once H_2 is generated, and removed from the solution.

A similar effect is observed when water oxidation catalysts (WOC) are deposited on the surface, although the benefit is less dramatic, especially with oxide semiconductors[4]. Unlike the hydrogen evolution reaction (HER), most oxide semiconductors are capable of oxidizing H_2O without the use of a co-catalyst, although the addition of a hole-accepting WOC (e.g. IrO_2, RuO_2, Co-P_i)[27–29] is still beneficial, for the same reasons listed above.

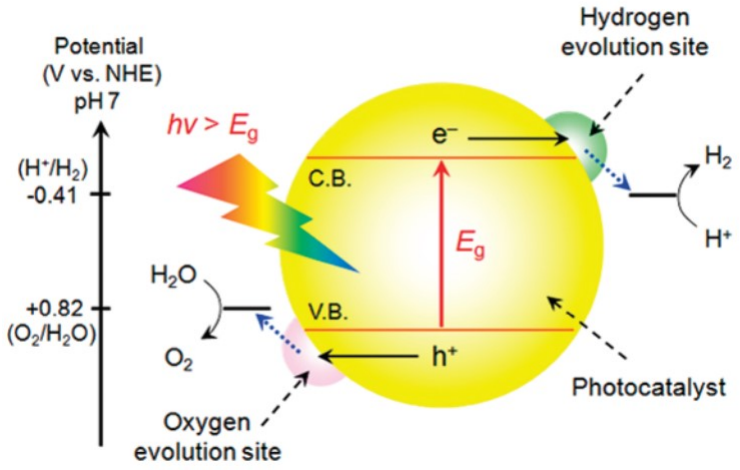

Figure 1.1.2.10. Schematic of overall water splitting by electron transfer to hydrogen evolution site and hole transfer to water oxidation site. Reproduced from ref. 2.

Overall water splitting on a single wide band gap semiconductor has been studied since the Honda-Fujishima effect was discovered in 1972.[11] Single semiconductor photocatalysts are

relatively simple to develop and produce. However, the simultaneous production of H_2 and O_2 on the same catalyst raises both chemical and engineering problems.

Single semiconductor water splitting requires the conduction and valence bands of the semiconductor to surround the reduction potentials of water, as described in Figure 1.1.2.2. This requirement limits the variety of catalysts which could be used in water splitting, including many catalysts with ideal surfaces, conductivity, and stability for water oxidation or reduction. Furthermore, for a water splitting catalyst to be effective in direct sunlight, the wider the bandgap is, the lower the maximum solar efficiency. The most effective single semiconductor water splitting catalysts are capable of high quantum efficiencies (>10%), but can only do so with light <410 nm, thus severely reducing the theoretical efficiency (Figure 1.1.2.11).[5]

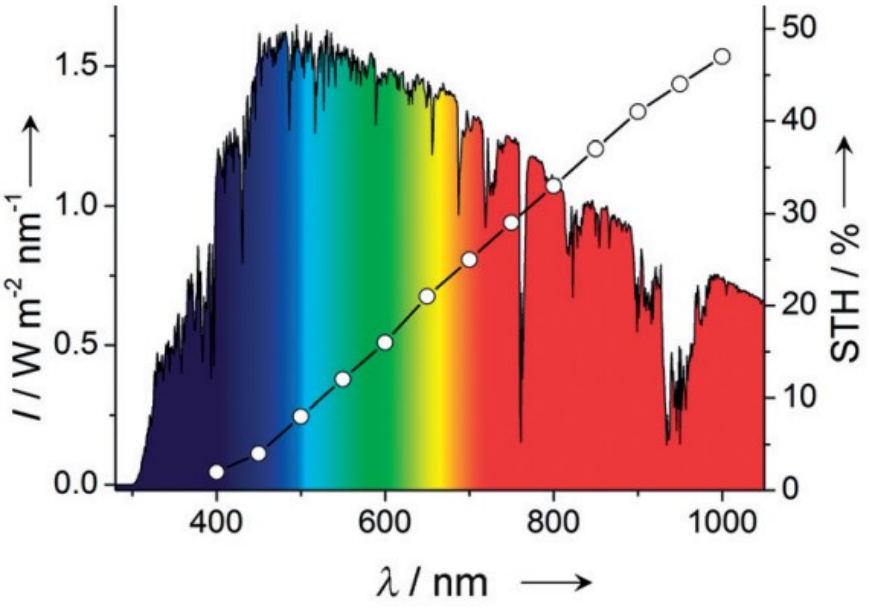

Figure 1.1.2.11. Solar spectrum (left) and the theoretical maximum solar efficiency for water splitting reaction for semiconductors absorbing ≤ specified wavelength (right). Reproduced from ref. 30.

1.2 Z-Scheme Water Splitting

1.2.1 Background

By using two different semiconductors, with a redox couple (with a reduction potential between $2H+/H_2$ and O_2/H_2O) acting as a recyclable "sacrificial" molecule, smaller band gap materials which surround one of the water reduction potentials can be utilized (Figure 1.2.1.1). This is the motivation for Z-scheme photocatalysis. After photoexcitation, water is oxidized into O_2 (and protons) by holes generated by one catalyst, the water oxidation catalyst (WOC), while the electron mediator is simultaneously reduced by the photoexcited electrons. The second catalyst, the hydrogen evolution catalyst (HEC) uses photoexcited holes to oxidize the electron mediator, while the electrons are able to reduce protons to H_2.

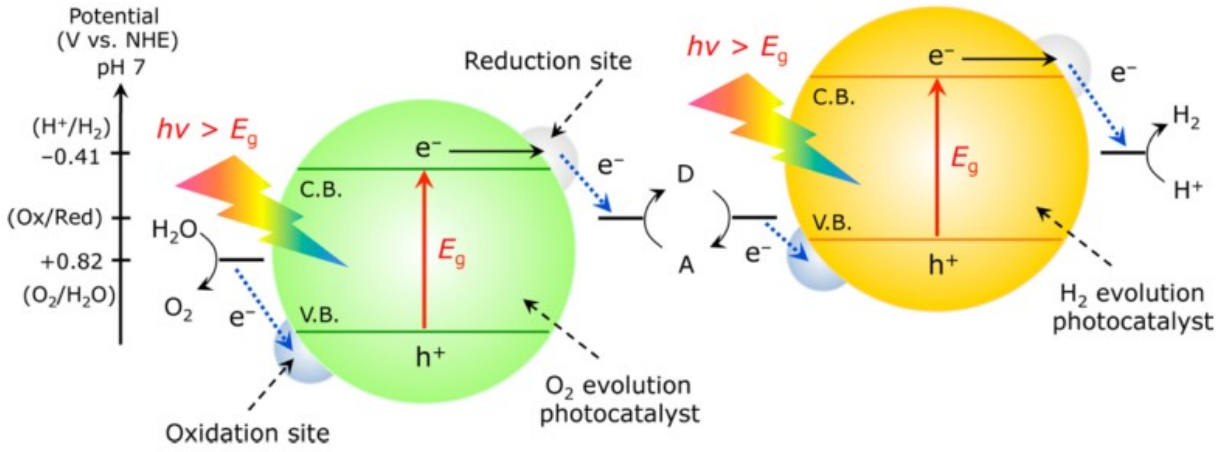

Figure 1.2.1.1. Schematic diagram of Z-scheme photocatalytic water splitting. Reproduced from ref. 5.

Immediately after a successful water oxidation and reduction event, the production of both H_2 and O_2 in close proximity on a catalyst can rapidly recombine into water, severely reducing the

efficiency of the cycle. In this effect, the evolution of H_2 and O_2 on separate surfaces will limit the ability for H_2 and O_2 to recombine.

Furthermore, in single semiconductor water splitting, the co-evolution of H_2 and O_2 produces a dangerously explosive mixture, with separation being very difficult and expensive. Z-scheme systems have the potential to use membranes selective for transport of the mediator, although current attempts have obtained only low yields.[31,32]

In the following section, we will discuss the history and current directions of Z-scheme water splitting, as it applies to H_2 and O_2 production from a single reaction media without the addition of sacrificial agents, or the use of UV light.

1.2.2 Ionic Electron Mediators

In 2001, the Arakawa group published the first artificial example of electron carrier-mediated overall water splitting on the surface of two separate semiconductor photocatalysts.[33] The group tested a series of potential HECs known to produce H_2 in the presence of sacrificial agents to determine the best activity using I^- as a sacrificial agent. Of the tested catalysts (including $InNbO_4$, Bi_2WO_6, *et al*),[34] $SrTiO_3$ doped with both 1 mol% Cr and Ta was the most active. $SrTiO_3$ (and Ta doped $SrTiO_3$) does not absorb light in the visible region, while all Cr doped $SrTiO_3$ exhibited some visible light absorbance, and photoactivity for water reduction. Activity was further improved by photodeposition of 0.3 wt% Pt. The platinum acts as an electron sink and reaction center for proton reduction.

Table 1.2.2.1. Summary of visible light active Z-scheme water splitting systems.

WOC	HEC	Redox mediator	pH	Wavelength(s) (nm)	O_2 activity (mL h^{-1} g_{WOC}^{-1})	AQY (%) (wavelength)	Year (ref)
Pt-WO_3	Pt-$SrTiO_3$:CrTa	I^-/IO_3^-	7	>420	0.10	0.1 (420.7)	2001 ([33,34])
$BiVO_4$	Pt-$SrTiO_3$:Rh	$Fe^{2+/3+}$	n.r.	420	n.r.	0.4 (420)	2004 ([35])
Bi_3MoO_6	Pt-$SrTiO_3$:Rh	$Fe^{2+/3+}$	n.r.	440	n.r.	0.2 (440)	2004 ([35])
WO_3	Ru-$SrTiO_3$:Rh	$Fe^{2+/3+}$	n.r.	420	n.r.	0.5 (420)	2004 ([35])
Pt-WO_3	Pt-TaON	I^-/IO_3^-	7	>420	1.34	0.4 (420)	2005 ([36])
Pt-WO_3	Pt-$SrTiO_3$:CrTa	I^-/IO_3^-	6.5	>420	0.18[a]	1.0 (420)	2005 ([37])
$BiVO_4$	Ru-$SrTiO_3$:Rh	$Fe^{2+/3+}$	2.4	Solar[b]	3.0	0.02 (solar)[b]	2008 ([38])
$BiVO_4$	Pt-$SrTiO_3$:Rh	$Fe^{2+/3+}$	2.4	Solar[b]	2.4	0.02 (solar)[b]	2008 ([38])
RuO_2/TaON	Pt-TaON	I^-/IO_3^-	6	>420	2.24[c]	0.2[c] (>420)	2008 ([39])
Pt-WO_3	Pt-$BaTaO_2N$	I^-/IO_3^-	n.r.	>420	0.75	n.r.	2008 ([40,41])
Pt-WO_3	Pt-$CaTaO_2N$	I^-/IO_3^-	n.r.	>420	0.56	n.r.	2008 ([40,41])
WO_3	$SrTiO_3$:Rh	$Fe^{2+/3+}$	n.r.	>400	0.11	n.r.	2009 ([42])
Pt-WO_3	ZrO_2-TaON	I^-/IO_3^-	5.4	420-800	5.96	6.3 (420)	2010 ([43])
RuO_2-TaON	Pt/ZrO_2/TaON	I^-/IO_3^-	n.r.	420-800	2.24[c]	n.r.	2011 ([44])
Pt-WO_3	Pt-TaON	I^-/IO_3^-	8.6	>420	0.82	n.r.	2011([45])
Pt-W/Mo-$BiVO_4$	CoS-$Zn_{0.2}Cd_{0.8}Se$	S^-/S_n^-	7	420	n.r.	<1 (420)	2013 ([46])
Pt-W/Mo-$BiVO_4$	Pt-W/Mo-$BiVO_4$-Pt	I^-/IO_3^-	7	420	n.r.	<1 (420)	2013 ([46])
PtO_x-WO_3	Pt-$BaZrO_3$-$BaTaO_2N$	$Fe^{2+/3+}$	n.r.	350-800	0	0	2013 ([47])
PtO_x-WO_3	Pt-$BaZrO_3$-$BaTaO_2N$	I^-/IO_3^-	n.r.	350-800	2.08	0.007 (solar)[b]	2013 ([47])
TiO_2 (rutile)	Pt-$BaZrO_3$-$BaTaO_2N$	I^-/IO_3^-	n.r.	Solar[b]	0.28	0.014 (solar)[b]	2013 ([47])
Pt-IrO_2-WO_3	DS[d]-Pt/$H_4Nb_6O_{17}$	I^-/IO_3^-	4.5	410-800	0.20	n.r.	2013 ([48])
Pt-WO_3	DS[d]-Pt/$H_4Nb_6O_{17}$	I^-/IO_3^-	4.5	410-800	0.11	n.r.	2013 ([48])
PtO_x/$HCsWO_3$	Pt-$SrTiO_3$:CrTa	I^-/IO_3^-	6.8	>420	0.87	n.r.	2013 ([49])
PtO_x-WO_3	Pt-$SrTiO_3$:CrTa	I^-/IO_3^-	6.8	>420	0.15	n.r.	2013 ([49])
$BiVO_4$	Rh-$SrTiO_3$:Rh	$Co(bpy)_3^{2-/3-}$	3.8	>420	10.5	0.06 (solar)[b], 2.1(420)	2013 ([50])
$BiVO_4$	Rh-$SrTiO_3$:Rh	$Fe^{2+/3+}$	3.8	>420	4.70	n.r.	2013 ([50])
$BiVO_4$	SSR-$SrTiO_3$:Rh	$Fe^{2+/3+}$	2.4	420	8.5	0.4 (420)	2013 ([51])
$BiVO_4$	HT-$SrTiO_3$:Rh	$Fe^{2+/3+}$	2.4	420	28.7	0.1 (solar)[b], 3.9 (420)	2013 ([51])
$BiVO_4$	PC-$SrTiO_3$:Rh	$Fe^{2+/3+}$	2.4	420	27.3	4.2 (420)	2013 ([51])
IrO_x-$SrTiO_3$:RhSb	Ru-$SrTiO_3$:Rh	$Fe^{2+/3+}$	2.4	420	0.67	n.r.	2014 ([52])
PtO_x-WO_3	Pt-$BaTiO_3$:Rh	I^-/IO_3^-	n.r.	>420	0.22	n.r.	2014 ([53])
Pt-WO_3	Pt/g-C_3N_4	I^-/IO_3^-	8.3	>395	0.25	n.r.	2014 ([54])
Pt-WO_3	Pt/g-C_3N_4	$Fe^{2+/3+}$	8.3	>395	0.06	n.r.	2014 ([54])
PSII	Ru-$SrTiO_3$:Rh	$Fe(CN)_6^{4-/3-}$	6	>420	1334[e]	n.r.	2014 ([55])

[a] Measured in ml h^{-1}, [b] used solar simulator, [c] initial rate, [d] DS = dye sensitized with coumarin-dithiophene based dye, [e] TOF (h^{-1}) of WOC.

On the water oxidation side, a series of known low bandgap (<3.0 eV) semiconductors (including $BiVO_4$, Fe_2O_3, In_2O_3, *et al*) were tested for water oxidation using IO_3^- to be sacrificially reduced. Ultimately, the most active catalyst was WO_3 doped with Pt to as a reduction site for IO_3^-.

Put together, a solution of Pt-WO_3, Pt-$SrTiO_3$:CrTa and NaI was capable of producing both H_2 and O_2 at a 2:1 stoichiometric ratio while illuminated by a 300 W Xe arc-lamp with a cutoff filter of all light <420 nm (Figure 1.2.2.1). Overall, the catalysts were capable of a sustained rate of 0.1 mL_{O2} h^{-1} g_{WOC}^{-1} for 70+ h. When the lamp was filtered for monochromatic light (420.7 nm), the catalyst obtained an AQY of 0.1%. This number is far below any commercial target, but was a good start for a new technique for water splitting.

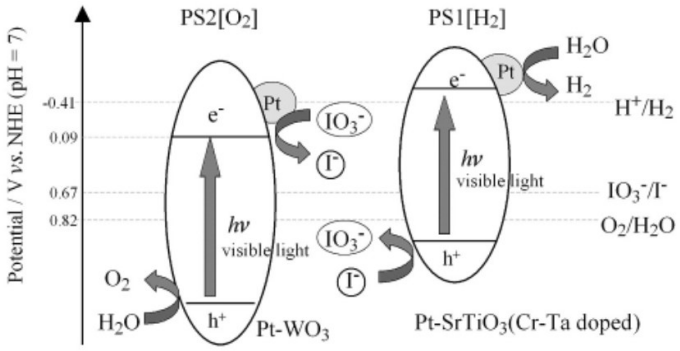

Figure 1.2.2.1. Schematic of the first artificial Z-Scheme catalyst for solar water splitting. Reproduced from ref. 33.

Over the last 15 years, many papers have been published using the Z-Scheme technique for water splitting. The entire list of results are shown in Table 1.2.2.1. A few of the more notable examples will be expanded on further.

In 2005, the Domen and Abe groups demonstrated the first use of TaON as an HEC.[36] TaON has an advantage of being a relatively narrow band gap semiconductor (~2.5 eV) with a conduction

band of -0.3 V vs NHE, well above the reduction potential of protons. Pt-TaON, along with Pt-WO_3 as a WOC in aqueous media with NaI produced 1.3 mL_{O2} h^{-1} g_{WOC}^{-1}. At 420 nm, the catalytic system provided an AQY of 0.4.

Interestingly, Pt-TaON was inactive in high concentrations of IO_3^-, even when concentrations of I^- was high. The cause of this is that in high concentrations of IO_3^-, Pt-TaON will reduce IO_3^- preferentially to protons, halting H_2 production in an unfavorable back-reaction. In the full Z-scheme reaction, Pt-WO_3 is capable of rapidly reducing IO_3^- to prevent a buildup of the oxidized product.

The Kudo group studied the use of Pt and Ru doped $SrTiO_3$:Rh as an HEC and the effect of the co-catalyst on the recombination of H_2 and O_2 on the surface of the co-catalyst.[38] In a sealed system, using $BiVO_4$ as a WOC and $Fe^{3+/2+}$ mediator, Pt/$SrTiO_3$:Rh and Ru/$SrTiO_3$:Rh produced nearly identical initial reaction rates (~9 mL_{O2} h^{-1} g_{WOC}^{-1}), although the Pt doped catalyst slowed to a halt within 50 h, while the Ru doped catalyst remained active. It was found that a competing dark reaction, the recombination of H_2 and O_2 into H_2O, was far more active with the Pt doped catalyst than the Ru doped one.

When photocatalysis using a solar simulator was performed when constantly flowing Ar though the system, the effect of water recombination was not apparent, as the catalysts were capable of 2.4 and 3.0 mL_{O2} h^{-1} g_{WOC}^{-1} for Ru and Pt doped catalysts, respectively. The solar efficiency of both was approximately 0.02%.

In 2009, the Lee lab demonstrated the ability to use a $Fe^{2+/3+}$ redox couple as a storable shuttle for separated H_2 and O_2 production.[42] The group loaded a 10 mM solution of $FeCl_2$ with Pt-$SrTiO_3$:Rh and illuminated to produce hydrogen. Once H_2 production halted, the entire system

was filtered, where the HEC was saved while the solution, now containing 10 mM Fe^{3+} was loaded with Pt-WO_3 to produce oxygen. The process was repeated for two full cycles with minimal reduction of activity. Although the catalytic activity was low (0.11 mL_{O2} h^{-1} g_{WOC}^{-1}), the Lee group provided an interested method for separation of H_2 and O_2.

In 2010, the Domen group continued their work into TaON by developing a Pt-ZrO_2/TaON (10:1 Ta:Zr) nanocomposite capable of a record 6.3% AQY at 420.5 nm.[43] In later studies, the cause of this improvement was ascribed to ZrO_2 nanoparticles on the surface of the Ta_3O_5 precatalyst preventing the production of Ta^{4+} defects on the surface of the final catalyst. These defects acted as ideal sites for e^-/h^+ recombination sites, and the suppression led to improved H_2 evolution (Figure 1.2.2.2).[56]

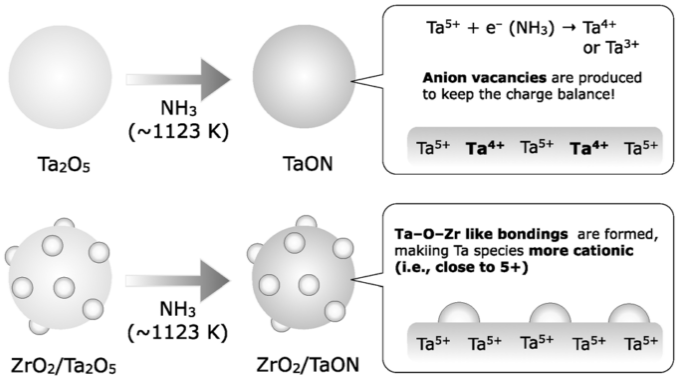

Figure 1.2.2.2. Effect of ZrO_2 protection of defect-free production of TaON. Reproduced from ref. 57.

Along with the Abe lab, the Domen group found that the deposition of rutile TiO_2 on Ta_3N_5 repels I^- from the surface of the catalyst, allowing for selective absorption and reduction of IO_3^- coupled with water oxidation with minimal (unwanted) I^- oxidation.[58] The catalyst was most active when Ir nanoparticles were deposited on the TiO_2 surface particles.

In 2013, Domen and Maeda developed a small bandgap ZrO_2/TaON based catalyst for hydrogen evolution. The final catalyst, $BaZrO_3$ on $BaTaO_2N$ (10:1 Ta:Zr), has a band gap of 1.8 eV (~660 nm). The catalyst was mildly effective (solar AQY = 0.014% with TiO_2 as WOC), the group did provide a record AQY for a HEC with a band gap <2.0 eV. Interestingly, while the reduction potentials of the conduction and valence bands were not elucidated, the catalyst was capable of both water oxidation and reduction, depending on co-catalysts loaded (IrO_x+ Ru for water oxidation, Pt for hydrogen evolution). This suggests a Z-scheme system using only small bandgap photocatalysts in within reach.

The Kudo lab demonstrated the first use of $Co(bpy)_3$ and $Co(phen)_3$ dyes as efficient redox couples for Z-scheme catalysts.[50] Using Ru-$SrTiO_3$:Rh as an HEC and $BiVO_4$ as a WOC, the group obtained a nearly threefold increase in activity for O_2 evolution with $Co(bpy)_3$ over Fe as an electron mediator (12.3 vs 4.7 $mL_{O2}\ h^{-1}\ g_{WOC}^{-1}$). As other groups have demonstrated, different Z-scheme systems are more effective with different electron mediators, so the introduction of alternate electron mediators to be tested for each new Z-scheme system is a valuable resource.[46,47,54,59]

The Kudo lab also investigated the effect of production method of $SrTiO_3$:Rh as an HEC.[51] Three methods were investigated: hydrothermal (HT), solid state (SSR) and "polymerizable complex" (PC). Even though the HT particles were typically 2x as large as the PC particles (~300 nm vs 150 nm by SEM), there was little difference in the catalytic activity of the catalysts (see Table 1.2.2.1). Meanwhile, PC and HT preparations were ~10x more efficient than the SSR (see Table 1.2.2.1) when coupled with $BiVO_4$ as a WOC, using and iron election mediator. This research demonstrated the effect of production methods in the development of future photocatalysts, beyond the control of the size of nanoparticles.

In 2014, Chen and co-workers demonstrated the ability to use photosystem II (PSII) directly as a highly active WOC.[55] PSII was coupled with Ru-$SrTiO_3$:Rh and using $Fe(CN)_6^{3-/4-}$ as an electron mediator (Figure 1.2.2.3), and was capable of an impressive TOF of 2489 h^{-1}, with respect to PSII. As expected, PSII was not very stable, showing signs of oxidative damage to the protein backbone within two hours. This lead to deactivation of the catalyst. However, the catalyst retained its activity for longer time when illuminated with light >600 nm, although the HER was inactive at this time. While a small bandgap HEC, such as Pt-$BaZrO_3$/$BaTaO_2N$ would allow for catalysis to continue efficiently for light >600 nm, limiting the use of light <600 nm will reduce the overall solar efficiency. Nevertheless, the use of an efficient, biological, small band gap WOC, and ferro/ferricyanide as an electron mediator is a promising development.

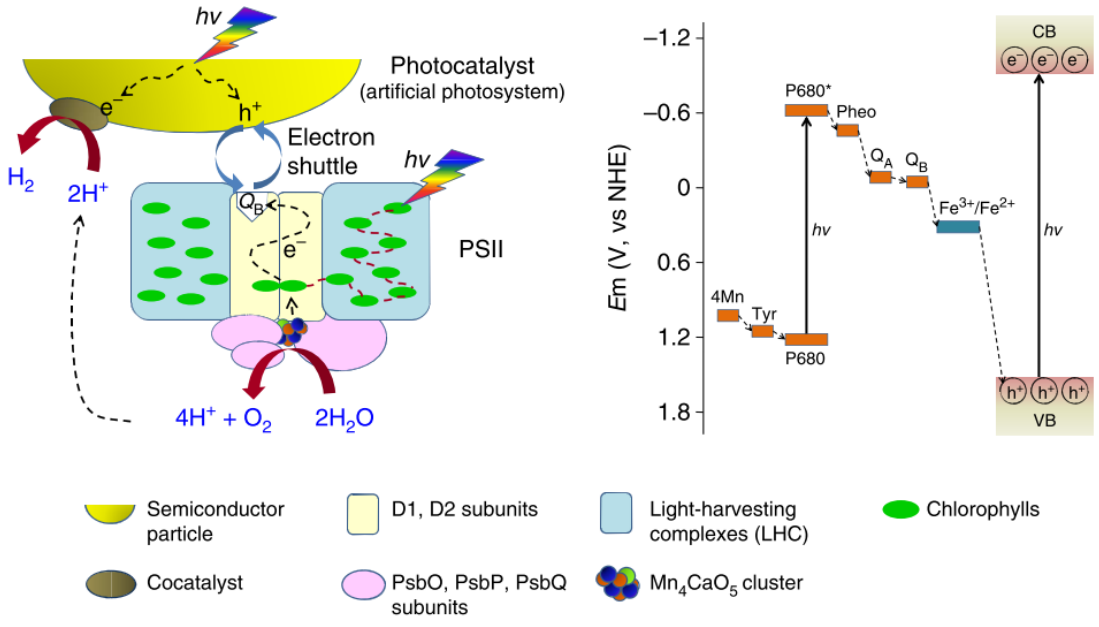

Figure 1.2.2.3. The use of PSII in a hybrid inorganic-biological system for overall water splitting. Reproduced from ref. 55.

1.2.3 Solid State Electron Mediators

A more recent evolution of Z-scheme water splitting research has been into the use of solid state electron mediators which physically and electrically connect the HEC and WOC without the use of ionic mediators. Ionic electron mediators are obviously crucial elements to a traditional Z-scheme system, but the unwanted backwards reactions (e.g. preferential oxidation of I^- instead of H_2O) can be largely avoided by using conductive or semiconductive materials to bridge the WOC and HEC. In addition, the ability to recover all catalytic components will be improved when using an entirely heterogeneous water splitting system, which will aid in reducing water pollution and reducing costs. This approach is similar to photoelectrochemical cells, except in the case of Z-scheme catalysis, the connective material is not necessarily a semiconductor, while the HEC and WOC must remain to be photosemiconductors.

Table 1.2.3.1. Summary of visible light active ionic mediator free Z-scheme water splitting systems.

WOC	HEC	Redox mediator	pH	Wavelength(s) (nm)	O_2 activity (mL h^{-1} g_{WOC}^{-1})	AQY (%) (wavelength)	Year (ref)
$BiVO_4$	Ru-$SrTiO_3$:Rh	Rh	3.5	>420	4.26	1.7 (420), 0.12 (solar)[a]	2009 ([60])
Ir-CoO_x-Ta_3N_5	Ru-$SrTiO_3$:Rh	Rh	3.9	>420	5.97	0.013 (solar)[a]	2013 ([61])
$BiVO_4$	Ru-$SrTiO_3$:Rh	WOC-PRGO	3.5	>420	4.11	1.0 (420)	2011 ([62])
$BiVO_4$	Ru-$SrTiO_3$:Rh	HEC-PRGO	3.5	>420	0.45	n.r.	2011 ([62])
$BiVO_4$	Ru-$SrTiO_3$:Rh	N_2H_4-RGO	3.5	>420	1.72	n.r.	2011 ([62])
$Ag_{1-x}SbO_{3-y}$	$ZnRh_2O_4$	Ag	n.r.	>450	1.49[b]	0.05 (405), 0.023 (470)	2014 ([63])
TiO_2 (rutile)	Pt-$CuGaS_2$	RGO	n.r.	Solar[a]	0.90[c]	0.023[b] (solar)[a]	2015 ([64])

[a] used a solar simulator, [b] measured in μL h^{-1} g_{WOC}^{-1}, [c] initial rate

The first example of ionic mediator-free Z-scheme catalysis came from the Kudo group (Figure 1.2.3.1).[60] The Kudo group used Ru-$SrTiO_3$:Rh as an HEC, and a series of well described WOCs (WO_3, $BiVO_4$, TiO_2, *et al*). In suspension at neutral or basic pH, the catalysts would remain apart

(no O_2 production), but at pH = 3.5, the HEC and WOC would agglomerate, with Rh surface particles acting as a connective mediator. The best WOC for this reaction was $BIVO_4$, including a solar AQY of 0.12%.

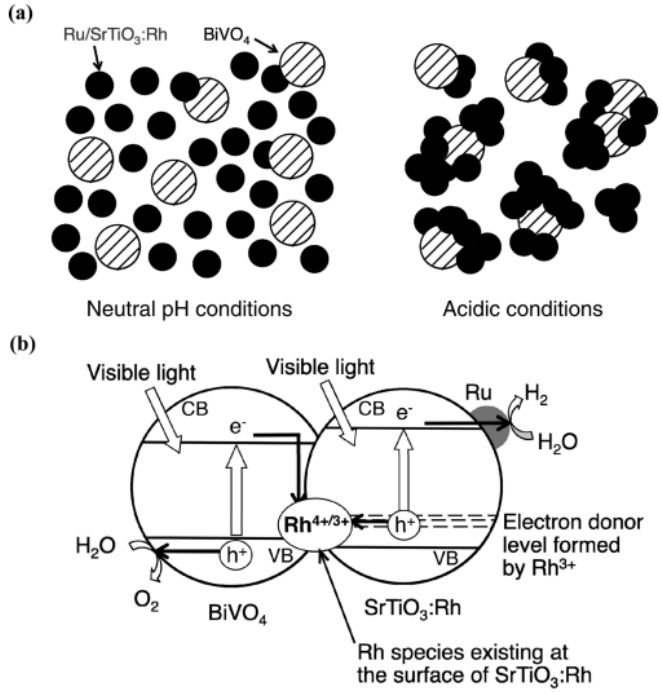

Figure 1.2.3.1. a) Effect of pH on clustering of $BiVO_4$ and Ru-$SrTiO_3$:Rh, and b) schematic of Rh-mediated Z-scheme water splitting. Reproduced from ref. 60.

The Amal group demonstrated the use of photoreduced graphene oxide (RGO) decorated with Ru-$SrTiO_3$:Rh and $BiVO_4$ for water splitting (Figure 1.2.3.2).[62] The catalyst was active for >24 h, with no signs of decomposition after 24 h, while producing 4.11 $mL_{O2}\ h^{-1}\ g_{WOC}^{-1}$ when graphene oxide (GO) was reduced with $BiVO_4$. Interestingly, the activity of the entire system was dependant on the catalyst responsible for GO reduction. When GO was reduced by Ru-$SrTiO_3$:Rh, the activity dropped to 0.45 $mL_{O2}\ h^{-1}\ g_{WOC}^{-1}$. Furthermore, by chemically reducing GO with hydrazine, the activity was only 1.72 $mL_{O2}\ h^{-1}\ g_{WOC}^{-1}$.

In both the cases of N_2H_4 and HEC, photoreductions were accompanied by efficient reduction of GO. Although in principle a better semiconductor has been so obtained, the system became highly hydrophobic and was capable of little contact with $BiVO_4$ to support deposition of the WOC, and little contact with water to promote water splitting. WOC-PRGO has provided less efficient photoreduction, which resulted in increased hydrophilicity, while maintaining adequate conductivity. This study shows that, when using RGO as a solid state mediator, careful tuning of the reduction efficiency is required.

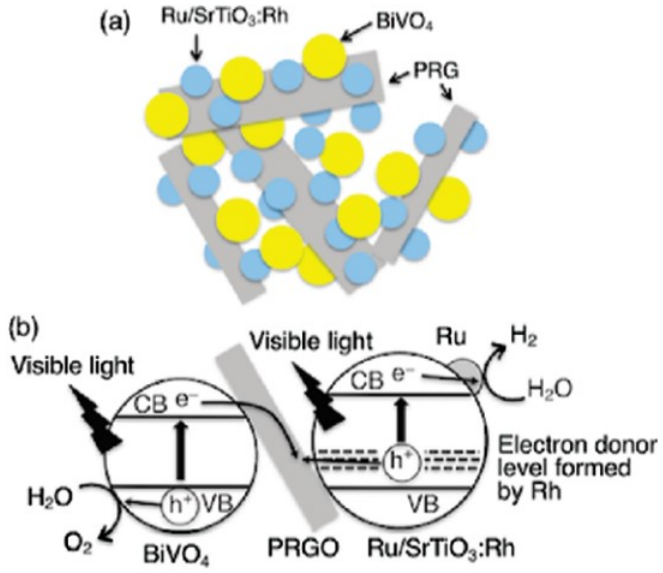

Figure 1.2.3.2. a) Schematic of the structure of $BiVO_4$-RGO-Ru-$SrTiO_3$:Rh, and b) band edge diagrams for Z-scheme water splitting. Reproduced from ref. 62.

Recently, the Kudo group published the activity of a series of Pt loaded metal sulfide HECs with TiO_2 as a WOC on RGO.[64] The most active sulfide was $CuGaS_2$, which was capable of an initial rate of ~0.9 mL_{O2} h^{-1} g_{WOC}^{-1} in simulated sunlight, although the catalyst degraded over the course of 12 hours. The initial solar AQY was 0.023%, although the efficiency drops quickly. A likely

cause of catalyst decay is decomposition of the metal sulfide, which may limit the effectiveness of sulfide-based HECs in the future.

Multiple other attempts at Z-scheme water splitting with solid state mediators has focused on the use of Au^0 or Ag^0 mediators, although to our best knowledge, only one example of overall water splitting have been published to date, while several examples of sacrificial hydrogen evolution have been disclosed.[65–69]

The Irie lab inserted Ag between the small band gap $ZnRh_2O_4$ (1.2 eV) as the HEC and $Ag_{1-x}SbO_{3-y}$ as the WOC (Figure 1.2.3.3).[63] The catalyst was capable of producing O_2 and H_2, although the activity was very low (1.5 **µ**L h^{-1} g_{WOC}^{-1}), under irradiation >460 nm. However moderate AQY of 0.05% was obtained in 405 nm (0.023 at 470 nm) light, although information about using light >400 nm for overall water splitting is not available. However, these results provide a proof of concept for noble metal mediators inserted between an HEC and a WOC.

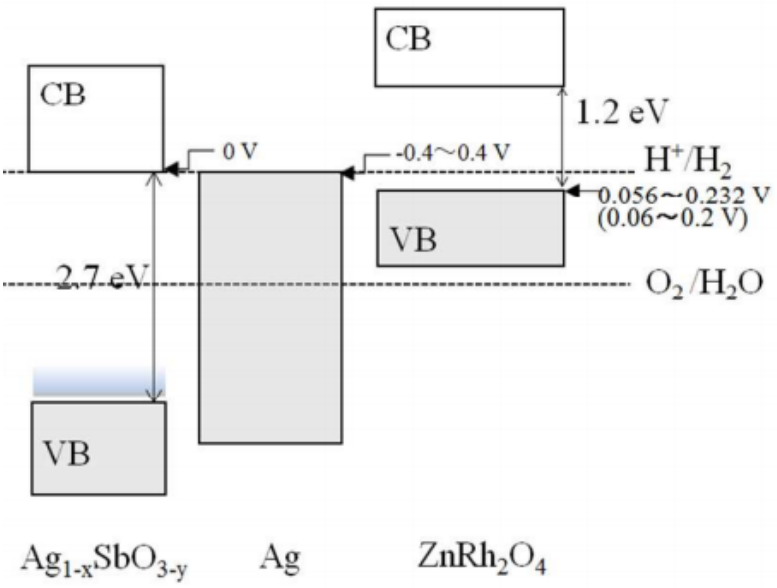

Figure 1.2.3.3. Schematic of $Ag_{1-x}SbO_{3-y}$-Ag-$ZnRh_2O_4$ solid state Z-scheme system. Reproduced from ref. 63.

1.2.4 Outlook

Over the past 15 years, the mechanics of Z-scheme water splitting and the major problems with its advancement have been clarified. Despite a number of successes, the quantum efficiency record for Z-scheme catalysts remains a low 6.3%, which was only obtained with 420 nm light. The record for solar efficiency is merely 0.12%, and was obtained by a solid state electron mediator.

However, the theoretical advantages of Z-scheme water splitting, especially for H_2/O_2 separation, are great enough that the field should remain active. Novel developments in low bandgap catalysts, taking advantage of WOCs and HECs with bandgaps $\leq$1.85 eV (650 nm) are currently being developed. Furthermore, a series of new electron mediators should be tested with new, and existing, Z-scheme systems to match catalytic systems to their most efficient electron mediators. Novel and existing methods to prevent unwanted oxidation/reduction of electron mediators should be tested with existing and new catalysts to improve quantum efficiencies. Finally, novel methods for separation of O_2 and H_2 evolution, to prevent unwanted water formation and improve evolved H_2 purity, must be developed for Z-scheme water splitting to become commercially relevant.

1.3 Water-assisted photoreduction of CO_2

1.3.1 Background

Photochemical CO_2 reduction coupled with water oxidation is theoretically very similar to photochemical water splitting. While the reduction potential of oxygen clearly remains the same, most reduction potentials of CO_2 is in fact very similar to that of protons (Figure 1.3.1.1).[8]

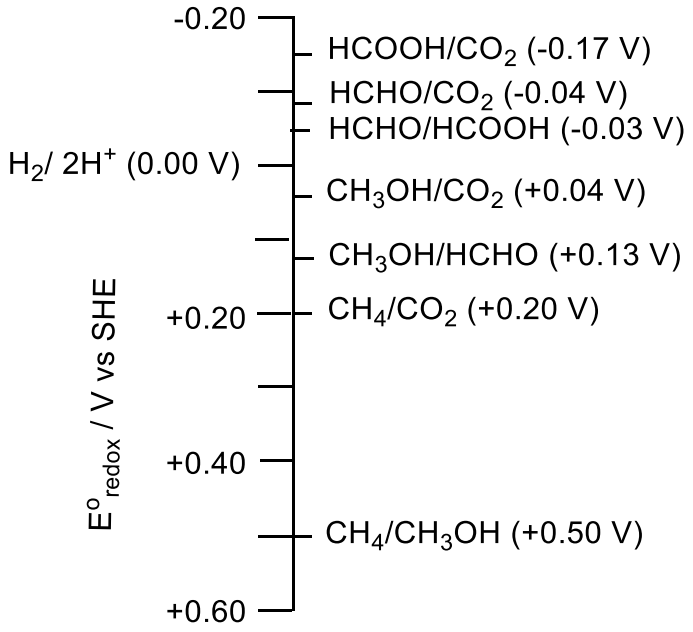

Figure 1.3.1.1. Reduction potentials (vs SHE at pH 0) of CO_2 and related compounds. Oxygen reduction occurs at +1.23 V.

This presents a problem of selectivity for CO_2 photoreduction. Not only is selectivity for the major carbon product difficult to control, but selectivity for carbon reduction over proton reduction is also difficult to control.[70–73]

The mechanism for CO_2 photoreduction on the surface of semiconductors is currently under debate, although it likely changes from catalyst to catalyst. Three complete pathways have been described in detail in the literature and are shown in Figure 1.3.1.2. Notably, the first step for each mechanism requires the initial formation of $CO_2^{\bullet}$. The reduction potential of $CO_2^{\bullet}/CO_2$ is -1.46 V, which is beyond the reduction potential of the conduction bands of semiconductors used for CO_2 reduction. The catalysts overcome this barrier by rapidly coupling protons to the reduction steps, which are more energetically favorable.

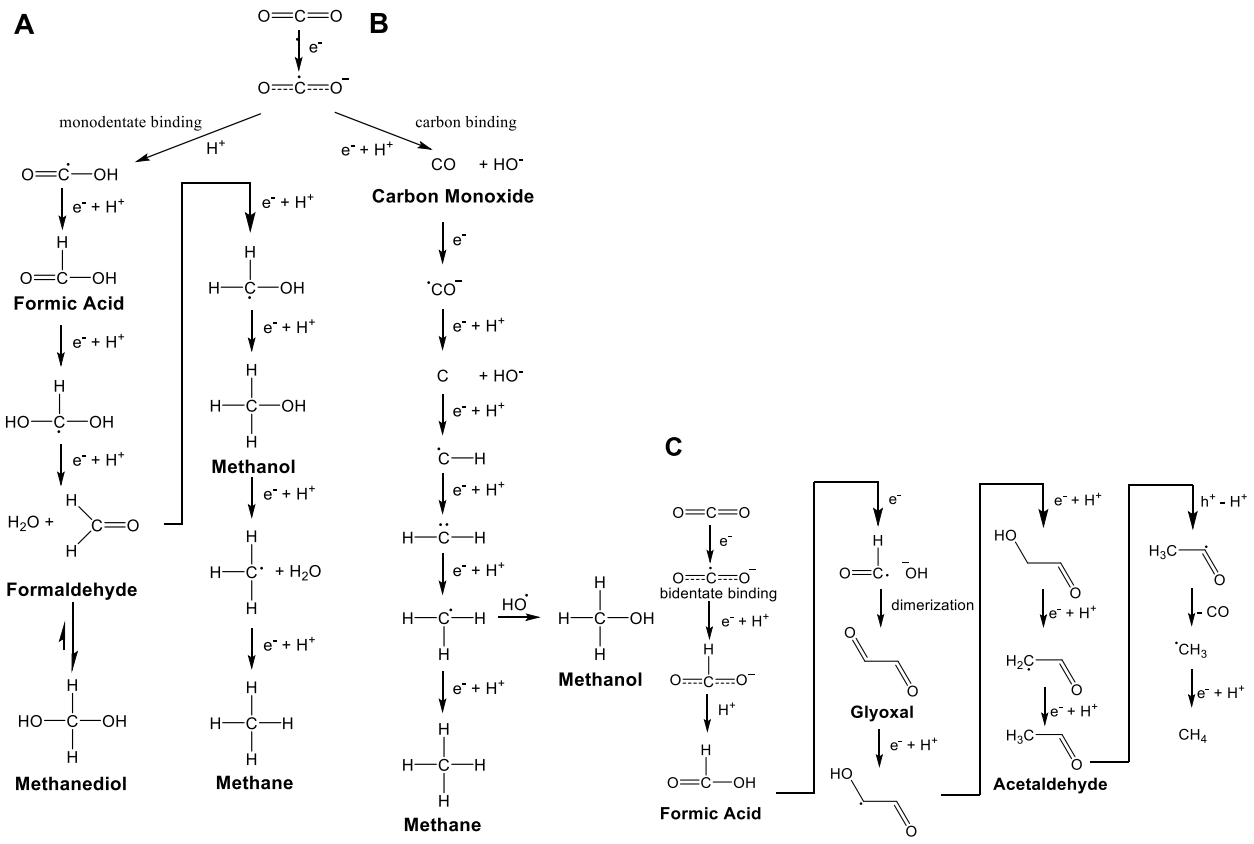

Figure 1.3.1.2. Proposed mechanism for the step-wise photocatalytic reduction of CO_2 into a selection of carbon based products. A) Represents the "formaldehyde" pathway which initiates via monodentate binding via oxygen, B) represents the "carbene" pathway which initiates monodentate binding via carbon, and C) represents the "glyoxal" pathway which initiates via bidentate binding via two oxygens.

All proposed pathways are initiated by the production of $CO_2^{\bullet}$ by single electron reduction of CO_2. Each of the three described pathways are represented by different binding of $CO_2^{\bullet}$ on the surface of the semiconductor.[74] In the formaldehyde pathway, the radical binds in a monodentate formation. This promotes proton-coupled electron transfer (PCET) to the distal oxygen, forming a hydroxylformyl radical.[75] This is followed by a series of stepwise PCETs through formic acid, formaldehyde, and methanol intermediates until methane is finally produced.

The formaldehyde pathway is supported by the presence of formaldehyde and formic acid in some reactions.[76–79] However, several key radical intermediates (e.g. (di)hydroxymethyl radical) have not been observed. The best evidence for this reaction is the observation of formaldehyde production which is not explicitly produced in the other two pathways, although production of formaldehyde may be the result of methanol oxidation.

The carbene pathway is promoted by direct semiconductor-carbon binding. PCET to an oxygen results in the immediate cleavage of the C-OH bond, producing CO on the catalyst surface and free hydroxide. The addition of two more electrons and a proton support a second C-OH cleavage, resulting in a carbon residue on the surface. Subsequent PCET to the carbon residue result in a series of carbon radicals which have been detected by ESR spectroscopy on the surface of TiO_2.[80]

The methyl radical formed after reduction of carbene can either undergo further reduction to methane, or be coupled with a hydroxyl radical (formed during water oxidation) to produce methanol. This method supports the common production of CO, methanol and methane, while formaldehyde and formic acid could still be produced by oxidation of methanol.

The glyoxal pathway was first proposed by the Shkrob and co-workers in order to explain the observation of a few intermediates in CO_2 reduction, including acetaldehyde and the formyl radical proposed to dimerize into glyoxal.[81] The glyoxal pathway begins with bidentate binding to $CO_2^{\bullet}$ and PCET to the carbon.[74] After the eventual formation of the formyl radical, it dimerizes into glyoxal. PCET eventually leads to the production of acetaldehyde. Acetaldehyde can be easily oxidized by a hole on the semiconductor surface, producing the unstable acetyl radical. This can undergo decarbonylation (producing CO) to produce a methyl radical, which

can be either reduced to methane, or coupled to a hydroxyl radical (as in the carbene pathway) to produce methanol.

The detection of several C_2 products in CO_2 reduction (including oxalate[82], acetaldehyde[83,84] and ethanol[73,85,86]) supports the glyoxal pathway as they are either directly produced in this pathway, or the potential product of reduction/oxidation of pathway intermediates.

The first major breakthrough in this direction was obtained by Honda *et al* in 1979 who first demonstrated the possibility of CO_2 photo reduction coupled with water oxidation by using TiO_2 and UV light, although the catalyst produced little CO_2 and was inactive in visible light due to TiO_2's large band gap (~3.2 eV).[87]

For the purposes of this section, we will focus on CO_2 photoreduction coupled with water oxidation, limiting the scope to semiconductor catalysts that use exclusively visible light or solar simulators and without the use of sacrificial electron donors. In addition, the focus of this section will be on CO_2 reduction into C-H fuels (CH_4, MeOH, EtOH, HCOOH) as they exist as potential couples for hydrogen evolution reactions discussed in the remainder of this thesis.

1.3.2 Reduction into methane

Since the pioneering work from Honda, various modifications to TiO_2 to improve photocatalytic activity in both visible and UV light.[8] Sensitizing TiO_2 with Ru-based dyes has been a mildly successful strategy, much like with water splitting, although yields remained low.[88] TiO_2 films with metal dopants have been more successful, although product selectivity remains problematic, with many side products being produced alongside methane.[90,92]

Table 1.3.2.1. Summary of visible light assisted CO_2 reduction coupled with water oxidation into methane.

Semiconductor	Co-catalyst	E_g (eV)	CH_4 production (μmol h^{-1} g_{cat}^{-1})	Wavelength(s) (nm)	Other products	Year (ref)
TiO_2 on OF[a]	Ru dye	3.2	0.85	solar[b]	-	2008 ([88])
TiO_2/SiO_2 on OF[a]	-	3.2	1.86	solar[b]	MeOH, C_2H_6	2008 ([89])
TiO_2	GaP	3.2/2.3	111	solar[g]	-	2014 ([90])
TiO_2/CNT	10 wt% Ni	2.22	0.15	>400	-	2013 ([91])
TiO_2[c]	Au	3.2	15[e]	532	MeOH, CH_2O, C_2H_6	2012 ([92])
TiO_2[c]	-	3.2	50	solar[g]	H_2	2014 ([93])
TiO_2[c]	1.5 wt% Au	3.2	210	solar[g]	H_2	2014 ([93])
TiO_2[c]	1.5 wt% Cu	3.2	280	solar[g]	H_2	2014 ([93])
TiO_2[c]	3:1.5 wt% Cu:Au	3.2	2200	solar[g]	H_2	2014 ([93])
TiO_2	3:1.5 wt% Cu:Au	3.2	44	solar[g]	H_2	2014 ([93])
Bi_2WO_6	-	2.75	1.1	>420	-	2011 ([94])
$Zn_{1.7}GeN_{1.8}O$	1 wt% Pt, RuO_2	2.6	11.5	>420	-	2012 ([95])
$Zn_xGe_yN_zO_k$	1 wt% Pt	2.7	2.7[f]	>400	-	2012 ([96])
AgBr/graphite	-	2.64	29.4	>420	MeOH, EtOH, CO	2014 ([86])
CdS/RGO	-	2.4	2.51	>420	MeOH	2014 ([97])
g-C_3N_4	15 wt% RGO	2.82	0.70	400-800	-	2015 ([98])
g-C_3N_4	2 wt% Pt	2.82	1.6	solar[g]	H_2	2015 ([99])
g-C_3N_4	-	2.82	0.30	400-800	-	2015 ([98])

[a] Catalyst on optical fiber, [b] concentrated sunlight, [c] Thin film, [d] AQY, [e] μmol m_{cat}^{-2} h^{-1}, [f] ppm g_{cat}^{-1} h^{-1}, [g] simulated sunlight

Recently, the Garcia group was able to simultaneously improve TiO_2 activity for methane production (up to 2200 μmol h^{-1} g_{cat}^{-1}), while demonstrating improving selectivity towards methane production over hydrogen production.[93] The group produced thin films of TiO_2 by spray deposition, loaded with nanoparticles of Au, Cu, or a combination of both (or blank). Bare TiO_2 produced H_2 and CH_4 in a roughly 1:1 rate, at ~ 50 μmol h^{-1} g_{cat}^{-1} for each. By adding Au particles, activity for CH_4 production increased fourfold, while H_2 production remained the same. Adding Cu reduced H_2 production by ~25%, while increasing CH_4 production >5x vs bare TiO_2. When depositing a Cu/Au alloy (optimized at 2:1 ratio), both H_2 and CH_4 production

increased, but CH_4 production increased >40x (vs bare TiO_2), while H_2 production increased by only ~5x (vs bare TiO_2).

The group explained the role of Au as an overall photocatalytic sensitizer, by plasmonic enhancement (claiming via direct electron injection). The role of Cu was elucidated as the key to CO_2 reduction selectivity. As electrons are injected into Cu (directly from Au), copper acts exclusively as a CO_2 reduction site, while TiO_2 reduction sites are both methane and H_2 reduction sites (Figure 1.3.2.1).

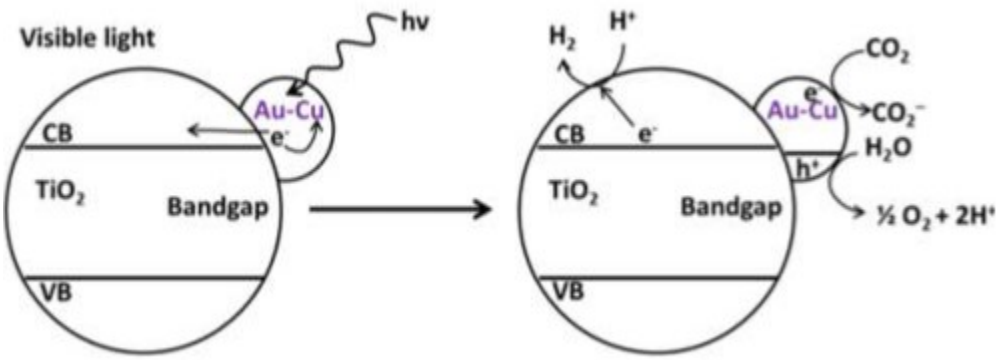

Figure 1.3.2.1. Effect of Au/Cu nanoparticles on the surface of TiO_2 to initiate selective CO_2 reduction vs water reduction. Reproduced from ref. 93.

Graphitic carbon nitride (*g*-C_3N_4) is a 2D semiconductor similar to graphene which has recently become a semiconductor and support for a variety of photochemical applications, including CO_2 photoreduction.[54,72,73,98–100] The reason for its popularity has to do with its native 2.7 eV band gap while limiting e^-/h^+ recombination by avoiding travel from the bulk to the surface (since it is a 2-D sheet). Furthermore, *g*-C_3N_4 is readily doped, and can be produced by an extremely facile synthesis (simply heating urea to ~500 ^{0}C), although more complex syntheses are known to improve activity.

Despite the interest in *g*-C_3N_4, activity for CO_2 photoreduction has remained low, ranging from 0.23-2.18 μmol h^{-1} g_{cat}^{-1} of CH_4 or EtOH products. However, it has been active towards CO (up to 20.3 μmol h^{-1} g_{cat}^{-1}), as shown by the Jiang and Xiong groups.[73] The groups deposited nanotubes and nanocrystals of Pd on the surface of *g*-C_3N_4 to test the dependence of crystal facet on selectivity for H_2 production vs organic products. The group found that nanocrystals, with exposed {100} facets preferentially reduce water, while nanotubes with exposed {111} facets preferentially reduce CO_2 (~10:1 CO:EtOH with trace CH_4).

1.3.3 Reduction into LOHCs

Table 1.3.3.1. Summary of visible light assisted CO_2 reduction coupled with water oxidation into LOHCs.

Semiconductor	Co-catalyst / electrolyte	E_g (eV)	Major Product	LOHC production (μmol h^{-1} g_{cat}^{-1})	Wavelengths(s) (nm)	Other products	Year (ref)
$InTaO_4$ (solid state)	1 wt% NiO	2.6	MeOH	1.39	400-800	-	2007 ([101])
$InTaO_4$ (nanoparticle)	1 wt% NiO	2.6	MeOH	11.1	400-1100	-	2010 ([102])
N-$InTaO_4$	3.2 wt% Ni/NiO	2.28	MeOH	165	390-770	-	2011 ([103])
$InNbO_4$	1 wt% NiO	2.5	MeOH	1.58	500-900	-	2012 ([104])
CdS	Bi_2S_3	1.28/2.4	MeOH	88	400-800	-	2011 ([105])
$Cu_{0.3}Ag_{0.07}In_{0.34}Zn_{1.3}S_2$	RuO_2	1.4	MeOH	34.3	>400	-	2011 ([106])
WO_3	-	2.79	MeOH	0.34	>400	-	2012 ([107])
$BiVO_4$	-	2.24	EtOH	112.5	>400	MeOH	2009 ([85])
$BiVO_4$	-	2.24	MeOH	18.8	>420	-	2012 ([108])
p-GaP[a]	Pyridine	2.3	MeOH	2.6	465	-	2008 ([70])
p-InP[a]	Ru dye	1.35	HCOOH	140[b]	>400	-	2010 ([109])
p-InP[a]	Ru dye	1.35	HCOOH	0.21[c]	solar[e]	-	2011 ([71])
Cu_2ZnSnS_4[a]	Ru dye	1.5	HCOOH	~5[d]	400-800	-	2011 ([110])
g-C_3N_4 (bulk)	-	2.7	EtOH	0.23	>400	H_2, CO, CH_4	2014 ([73])
g-C_3N_4 (nanocrystals)	5.7 wt% Pd	2.7	EtOH	0.67	>400	H_2, CO, CH_4	2014 ([73])
g-C_3N_4 (nanotubes)	5.7 wt% Pd	2.7	EtOH	2.18	>400	H_2, CO, CH_4	2014 ([73])

[a] Photoanode, [b] μmol h^{-1}, [c] μmol cm^{-2} h^{-1}, [d] TON, [e] solar simulator

In 2009, the Huang lab demonstrated that $BiVO_4$ nanoparticles was capable of CO_2 photoreduction into ethanol while bubbling CO_2 through the solution.[85] The catalyst was largely selective for EtOH formation, although a small amount of methanol was produced in low energy

visible light. Ultimately the catalysts was capable of 112 μmol h^{-1} g_{cat}^{-1} in visible light. The catalyst was not tested for more than 80 minutes, although the catalyst was capable of being recovered and reused for up to 5 times with a minimal degradation of activity.

Later, in 2012, Peng and co-workers produced similar $BiVO_4$ nanoparticles as the Huang group, used a static CO_2 atmosphere and instead selectively produced MeOH, for an activity of 18.8 μmol h^{-1} g_{cat}^{-1}.[108] A trace amount of EtOH detected although not quantifiable. The catalysts was lost activity after 6 hours of catalysis before deactivating. After recovery, the catalyst can be reused at least three times with mild reduction of activity. Interestingly, the catalyst is capable of photoreducing CO_2 into methane when sodium sulfite is used as a sacrificial electron donor.[111]

In recent years, the field of CO_2 reduction has begun to follow that of water splitting, in the development of complex devices for enhanced efficiency. Numerous water splitting groups have incorporated photovoltaic semiconductors (e.g. amorphous Si, GaP, GaAs, *et al*) with water oxidation and reduction electrocatalysts (e.g. Co_3O_4, NiMoZn alloy).[112,113] Recently, the Hwang group used a $Cu(In_xGa_{1-x})(S_ySe_{1-y})_2$ (CIGS) photovoltaic core loaded with a Co_3O_4 WOC and an electrodeposited Au film as a CO_2 reduction catalyst (Figure 1.3.3.1).[114]

When illuminated by a solar simulator, the solar cell was capable of producing CO at a rate of 64 μmol h^{-1} cm^{-2}, with an impressive initial solar-to-CO conversion of 4.23% (which decreased to 2.67% over 5 hours). Impressively, this catalyst was selective for CO production, which is a function of the gold film's selectivity for CO production. As a proof of this concept, the group replaced the Au film with Pt, and selectively produced H_2 with a 4.37% (solar-to-hydrogen) STH efficiency.

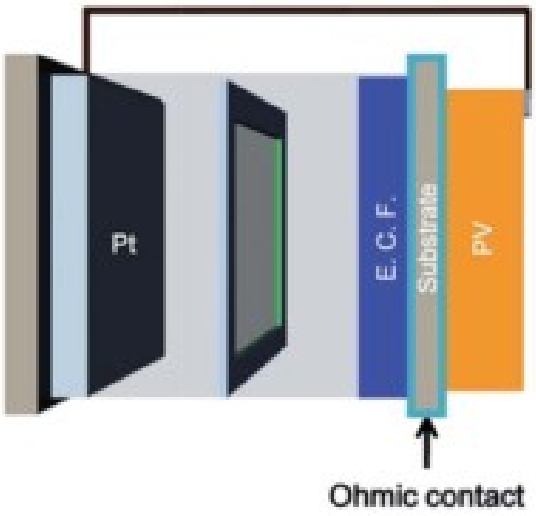

Figure 1.3.3.1. Schematic of solar fuel device used by the Hwang group for CO_2 reduction, where PV represents the CIGS semiconductor, ECF represents the Co_3O_4 water oxidation catalyst, and the Pt film is replaced by Au for the purposes of CO_2 reduction. Reproduced from ref. 114.

1.3.4 Outlook

The future of CO_2 photoreduction depends on several factors. First, researchers must reduce unproductive activity, including electron/hole recombination and reoxidation of organic products. Furthermore, smaller bandgap semiconductors must be utilized in order to increase the theoretical maximum efficiency. Finally, a series of selective CO_2 reduction catalysts must be identified to avoid wasted side-product formation. A key to the final requirement will be to conclusively elucidate CO_2 reduction mechanism(s) on the surface of heterogeneous catalysts, or in modelling studies for catalysts with well-defined surfaces.

1.4 Methanol Dehydrogenation

1.4.1 Background

Methanol is an attractive platform for hydrogen storage primarily for its high 12.6 wt% content of hydrogen in a liquid material. Compared to other liquid organic hydrocarbons (LOHCs), methanol has the greatest potential for efficient hydrogen storage[115–117]. Industrially, MeOH is readily dehydrogenated to CO_2 and 3 equivalents of H_2, although these processes are carried out at high temperatures and pressures using heterogeneous catalysts[117]. In this section, historical and current research aimed at MeOH dehydrogenation at temperatures lower than 150^0C and at atmospheric (or nearly atmospheric) pressures will be highlighted.

1.4.2 Anhydrous methanol dehydrogenation

In the mid-1980s, Saito[118–120], Maitlis[121] and Cole-Hamilton[122] began to experiment with methanol dehydrogenation using homogeneous platinum group metals. The majority of these reactions were using ruthenium-phosphine catalysts, although Ir, Rh, Pt, and Pd catalysts were also targeted.

Following up on prior research into dehydrogenation of isopropanol and other primary and secondary alcohols, Saito tested $M_2Cl_2(dppm)_2$ (M = Pd, Pt; dppm = bis(diphenylphosphino)methane) and cis-$Rh_2Cl_2(dppm)_2$ dimers in refluxing MeOH under irradiation (400 W Hg lamp). In all cases, activity was greatly improved with the addition of 10% acetone. $Pd_2Cl_2(dppm)_2$ exhibited the greatest activity in the presence of acetone (TOF = 156 h^{-1}), and stability (stable after 10 h in light). The improvement resulting from addition of acetone was proposed to be caused by non-bonding electrons being excited to π^* orbital to

initiate reaction. As evidence, the group demonstrated that catalyst-free solutions of 9:1 MeOH:acetone showed some activity, producing CH_4, CO, and H_2.

Table 1.4.2.1. Early examples of methanol dehydrogenation by homogeneous catalysts in anhydrous solvents.

Catalyst	Additive	TOF (h^{-1})	TON	Time (h)	Yield (%)	Temp (^{0}C)	Major C_1 Product	Ref
cis-$Rh_2Cl_2(CO)_2(dppm)_2$	acetone, hν	130	n.r	n.r.	n.r.	64	MEG	[118]
$Pd_2Cl_2(dppm)_2$	acetone, hν	156	n.r.	n.r.	n.r.	64	CH_2O	[118]
$Pt_2Cl_2(dppm)_2$	Acetone, hν	30	n.r.	n.r.	n.r.	64	n.r.	[118]
$Ru_2(OAc)_4Cl(PPh_3)$		0.20	3.4	17	2.8	66	CH_2O	[119]
$Ru_2(OAc)_4Cl(PEtPh_2)$		0.59	10.0	17	8.1	66	CH_2O	[119]
$Ru_2(OAc)_4Cl(PEt_2Ph)$		0.47	8.0	17	6.5	66	CH_2O	[119]
$Ru(PPh_3)_3Cl_2$		3.61	65	18	2.1	150	DMM	[121]
$Ru(H)_2(PPh_3)_4$	NaOH, hν	27.7	55.4	2	n.r.	150	n.r.	[122]
$Ru(H)_2N_2(PPh_3)_3$	NaOH, hν	37.3	74.6	2	n.r.	150	n.r.	[122]
$Ru(SnCl_3)_2(P(OMe)_3)_3$	$MeNO_2$	0.06	1.09	20	n.r.	65	MeOAc	[123]
$Ru(SnCl_3)_2(P(OMe)_3)_3$	CCl_4	0.29	5.82	20	n.r.	65	MeO_2C	[123]
$Ru(Cp^*)(PPh_3)_2SnF_3$	MeCN	7.7	154	20	0.24	120	MeOAc	[124]

In addition to studying the aforementioned chloride dimers, the Saito group was also working on thermocatalytic dehydrogenation of MeOH with homogeneous catalysts. Saito used $Ru_{1/2}(OAc)_{1/4}Cl(PPh_{3-n}Et_n)_{3/1}$ catalysts at reflux temperatures to produce hydrogen gas and formaldehyde with low activity.[119] Despite the low activity, these catalysts were rather robust, capable of steady activity for approximately 17 hours. The highest activity was exhibited by $Ru_2(OAc)_4Cl(PPh_2Et)$ (TOF = 0.59 h^{-1}). Later, the same group suggested a mechanism via β-H elimination, followed by acid-promoted H_2 release (Figure 1.4.2.1).[120]

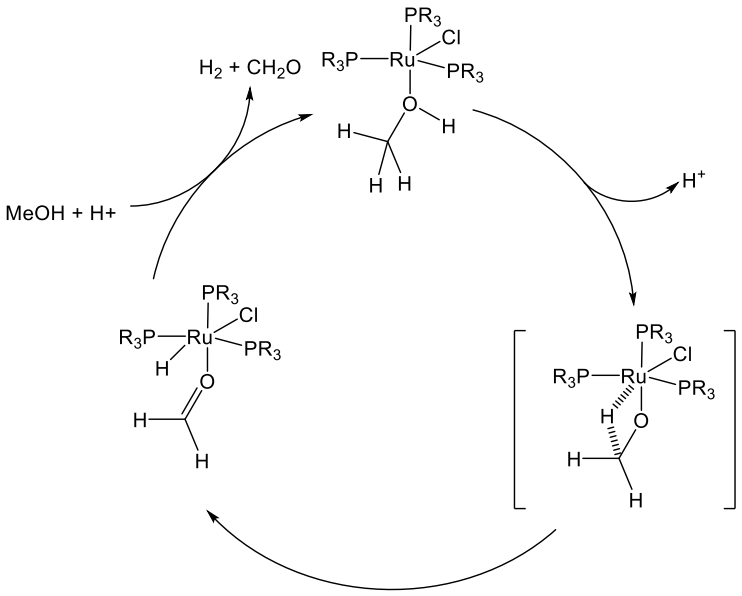

Figure 1.4.2.1. Proposed mechanism for acid-catalyzed methanol dehydrogenation with $Ru(PR_3Cl)$ catalysts. Modified from Ref 120.

At the same time as the Saito group was working with diruthenium acetates, Maitlis and co-workers reacted $Ru(PPh_3)_3Cl_2$ with methanol to 150 ^{0}C, to form hydrogen, methyl formate and dimethoxymethane.[121] At these elevated temperatures, Maitlis was capable of obtaining moderate activity (TOF = 3.61 h^{-1}), and low yields (2% assuming 1 molecule of H_2 per MeOH). The group was able to precipitate out a hydride-bridged di-ruthenium carbonyl complex, believed to be an active species in the catalytic cycle.

Accordingly, Cole-Hamilton used $Ru(H)_2(PPh_3)_4$ and $Ru(H)_2(N_2)(PPh_3)_3$ with and without light (500 W tungsten/halogen lamp) in basic conditions (10 eq. NaOH) and elevated temperatures (150 ^{0}C).[122] While reactions in the dark provided moderate activity (7.5 turnovers h^{-1} without N_2 ligand and 6.4 turnovers h^{-1} with N_2 ligand), when the solution was irradiated, the TOF drastically improved (27.7 h^{-1} and 37.3 h^{-1}, respectively). The effect of light was not fully

elucidated, although it was proposed to promote the release of H_2 from in situ formed $RuH_4(PPh_3)_3$.

Shinoda used $RuCl_n(SnCl_3)_{2-n}(P(OMe)_3)_{4/3}$ catalysts to target acetic acid production, via CH_2O.[123] Production was low in all cases, although the highest is $Ru(SnCl_3)_2(P(OMe)_3)_3$ (TOF = 0.055 h^{-1}) refluxing in $MeNO_2$. Interestingly, dehydrogenation alone is improved in CCl_4 (TOF = 0.291 h^{-1}), although the targeted acetic acid (or methyl acetate) was only detected in trace quantities, methyl formate was instead the dominant product. While still targeting dehydrogenation of MeOH to acetic acid, Shinoda used $Ru(Cp^*)(PPh_3)_2X$ compounds (X = Cl, $SnCl_3$, SnF_3) at 120 ^{0}C.[124] The group was able to observe modest TOF (7.7 h^{-1}) with the SnF_3^- co-metallic ligand, while producing low yields with the $SnCl_3$ and Cl ligands. The pathway is proposed to proceed through formaldehyde and methyl formate intermediates before producing acetic acid, which readily undergoes esterification to methyl acetate, although no formaldehyde or methyl formate were detected.

In each of these early examples, catalysis was performed in anhydrous conditions, which typically lead to the major product being formaldehyde, and the production of hydrogen being limited due to the difficulty in dehydrogenating non-hydrated formaldehyde (which would form carbon monoxide as a co-product). It is therefore understandable that many of these groups were not interested in MeOH as a hydrogen carrier, the focus of their effort being instead on using methanol as a source for formaldehyde, methyl formate, acetic acid, dimethoxymethane and others.

1.4.3 Heterogeneous photocatalysts for methanol dehydrogenation

While the majority of research into low temperature alcohol dehydrogenation had focused on the oxidation of larger alcohols, including ethanol, isopropanol and monoethylene glycol,[125–127] papers describing successful low-temperature hydrogen production from methanol in aqueous media began to proliferate in 2010. Initial reports of catalytic systems operating below 100 degrees used heterogeneous catalysts, with or without photoactivation, to produce hydrogen.

More recently, a great deal of research has focused on decomposition of methanol using photocatalysts, although the ultimate goal was to achieve water splitting using methanol as a sacrificial agent. A few of the more notable examples are also shown in Table 1.4.3.1. While this is not complete, it represents a substantial snapshot of the focus of the field.

Table 1.4.3.1. Hydrogen production by heterogeneous photocatalysts in water using methanol as a sacrificial agent.

Catalyst	**Light Source**	**TOF (h^{-1})**	**TON**	**Temp (^0C)**	**Additive**	**Ref**
0.1 %Au/TiO_2 (anatase)	Hg	1.34	n.r.	R.T.	None	[128]
0.1 %Au/TiO_2 (rutile)	Hg	1.05	n.r.	R.T.	None	[128]
1% Pt/TiO_2	15 W UV	1.01	101	R.T.	None	[129]
Ag_2O/TiO_2	Sunlight	5.35	139	n.r.	None	[130]
Bi_2S_3/TiO_2	UV (365 nm)	0.136	0.583	R.T.	NaOH	[131]
Bulk Pt/TBA$Ca_2Nb_3O_{10}$	300 W Xe	1.82	9.11	30	NaOH	[132]
Nano Pt/TBA$Ca_2Nb_3O_{10}$	300 W Xe	24.6	123	30	NaOH	[132]
0.5% Pt/$NaTaO_3$	150 W Hg	0.038	0.265	25	None	[133]
0.5% Pt/Ce$NaTaO_3$	150 W Hg	0.012	0.082	25	None	[133]
0.5% Pt/Y$NaTaO_3$	150 W Hg	0.163	0.982	25	None	[133]
0.5% Pt/Yb$NaTaO_3$	150 W Hg	0.140	0.739	25	None	[133]
0.5% Pt/La$NaTaO_3$	150 W Hg	0.106	0.191	25	None	[133]

While the majority of research into low temperature alcohol dehydrogenation had focused on the oxidation of larger alcohols, including ethanol, isopropanol and monoethylene glycol,[125–127] papers describing successful low-temperature hydrogen production from methanol in aqueous media began to proliferate in 2010. Initial reports of catalytic systems operating below 100 degrees used heterogeneous catalysts, with or without photoactivation, to produce hydrogen.

More recently, a major research effort was directed towards decomposition of methanol using photocatalysts, although the ultimate goal was to achieve water splitting using methanol as a sacrificial agent. A few of the more notable examples are also shown in Table 1.4.3.1 While this is not complete, it represents a substantial snapshot of the focus of the field.

Many researchers used the well-studied TiO_2 system with a variety of dopants to dehydrogenate methanol. These dopants include platinum-group metal deposited on the surface of the catalyst to take advantage of the plasmon effect. This is to both reduce the effective band gap of the catalyst and reduce recombination of electron/hole pairs. Ohtani photodeposited Au on a series of TiO_2 catalysts. Irradiating the catalyst with an unfiltered Hg lamp obtaining optimal MeOH dehydrogenation with between 0.1 to 4 wt% deposition of Au on anatase TiO_2 (TOF ~ 1.4 h^{-1}).[128] Meanwhile, Puzenat directly coupled MeOH dehydrogenation to a PEM fuel cell to test the activity of Pt/TiO_2 photocatalysts.[129] The group used a 15 W UVA lamp for both photodeposition of Pt onto TiO_2 and the hydrogen production reactions. While activity was low (TOF = 1.01 h^{-1}), the outlet H_2 was both CO and CO_2 free, allowing for the continuous activity of the fuel cell without poisoning for at least 100 h.

Secondary semi-conductors are also often deposited on TiO_2 to promote charge separation and reduce the effective band gap via electron or hole injection into TiO_2 by the second photocatalyst. In 2010, the Subrahmanyam group deposited Ag_2O onto anatase TiO_2 and irradiated a water:methanol solution in the sun.[130] The group was able to produce a moderate TOF of 5.35 h^{-1}, which was stable for 24 hours. The group also tried depositing reduced Ag on TiO_2 although no activity was detected. Later, in 2012, Kang and Kim attempted to dehydrogenate MeOH with Bi_2S_3 on TiO_2, although the activity was low (TOF = 0.136 h^{-1}), and produced in UV light (365 nm).[131]Moving on from using TiO_2 catalysts, the Osterloh group studied the difference between using nanocrystals (~1 nm thick) of Pt loaded $TBACa_2Nb_3O_{10}$ structures vs their bulk (~250 nm thick) counterparts (see Figure 1.4.3.1).[132] The bulk structures were capable of moderate activity (TOF = 1.82 h^{-1}), though the nanoscale structures were capable of > 10x activity (TOF = 24.6 h^{-1}). These results are proposed to be the result of reduced path length for electron/hole pairs to travel to the catalyst surface, which reduces the probability of charge recombination.

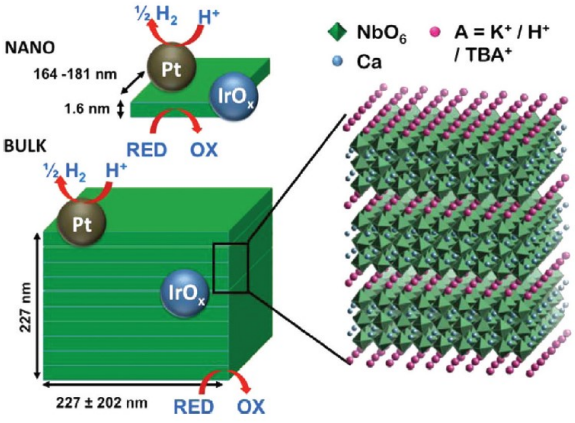

Figure 1.4.3.1. Hydrogen production by bulk and nano-scale niobate catalysts using methanol as a sacrificial agent. Either Pt or IrO_x was deposited for each experiment. Reproduced from ref. 132.

More recently, de la Pena, O'Shea and co-workers tested a series of $MNaTaO_3$ (M = Ce, Y, Yb, La) catalysts were produced by solid state synthesis, followed by photodeposition of 0.5% Pt.[133] While the Yb and Y catalysts were the most active (TOF = 0.140 and 0.164 h^{-1}, respectively vs M-free TOF = 0.038 h^{-1}), activities were generally low. The Y and Yb species exhibited greater absorbances than the La and undoped catalysts, which resulted in the increased activity. While Ce doped catalysts contained the greatest absorbance in the visible region, the structure of the catalyst was altered from orthorhombic to monoclinic, which is proposed to be a less active form for catalysis.

1.4.4 Aqueous methanol dehydrogenation

In 2013, the Beller group published the first example of a homogeneous catalyst capable of dehydrogenating methanol below 100 ^{0}C, while simultaneously providing high activities and stability.[134] Using Ru(H)(PNP) catalysts, Beller and co-workers were capable of obtaining steady high activities (TOF = > 120 h^{-1} for at least three hours) at a low temperature (72^{0}C) and a low concentration of base (0.5 M NaOH). The same catalysts were also tested in very basic conditions (8.0 M KOH) with pure MeOH, and higher temperatures (95^{0}C) to provide stable TOF exceeding 4700 h^{-1}. Interestingly, while carbonate and formate salts were readily detected in the system, formaldehyde (and methanediol) was not. This suggests that the dehydrogenation of formaldehyde is far too rapid for detection (Figure 1.4.4.1). In ideal conditions, the maximum TON exceeded 350 000, well on its way to industrial relevance.

Table 1.4.4.1. Methanol dehydrogenation by homogeneous catalysts in methanol:water mixtures.

Catalyst	**Additive**	**TOF (h^{-1})**	**TON**	**MeOH: H_2O (mL)**	**Temp (^0C)**	**Ref**
Ru(MACHO)(Cl)	NaOH[a]	121[c]	n.r.	4:1	72	[134]
Ru(H)(Cl)(CO)(PNP^{Ph})	NaOH[a]	48[c]	n.r.	4:1	72	[134]
Ru(MACHO)(Cl)	KOH[b]	2205[c]	n.r.	9:1	91	[134]
Ru(H)(Cl)(CO)(PNP^{Ph})	KOH[b]	1093[c]	n.r.	9:1	91	[134]
Ru(MACHO)(Cl)	KOH[b]	4734[c]	n.r.	neat	95	[134]
Ru(MACHO)(Cl)	KOH[b]	n.r.	>350000	4:1	72	[134]
Fe(MACHO)(Br)	KOH[a]	8.3[c]	n.r.	9:1	72	[135]
Fe(MACHO)(Br)	KOH[b]	617[c]	9834	9:1	91	[135]
Fe(MACHO)(Br)	KOH[b], PNP	520[c]	9184	9:1	91	[135]
Ru(H)($trop_2dad$)	THF	54	540	~4:5	90	[136]
Ru(H)(Cl)(CO)(NNP^{tBu})	KOH[d],,toluene	43	9288	~1:5	100	[137]
Ru(H)(Cl)(CO)(NNP^{tBu})[f]	KOH[d], toluene	45	9720	~1:5	100	[137]
Ru-MACHO-BH_3 + $Ru(H)_2(dppm)_2$	triglyme	239[e]	>600	9:1	93.5	[138]
Ru-MACHO-H + $Ru(H)_2(dppe)_2$	triglyme	80[e]	~4200	9:1	93.5	[138]
Ir(Cp*)(Cl)(IMes)(BF_4)[g]	KOH[h]	59	880	~4:1	91	[139]
Ir(CO)($DMI)_2(BF_4$)[g]	KOH[h]	112	1680	~4:1	91	[139]
Ir(CO)($DMI)_2(BF_4$)[g]	KOH[h]	533	8000	neat	91	[139]

[a] 0.5 M, [b] 8.0 M, [c] TOF of first three hours, [d] 40 mM, [e] TOF of first hour, [f] recovered from prior entry, [g] primary carbon product is formate, [h] 6.7 M

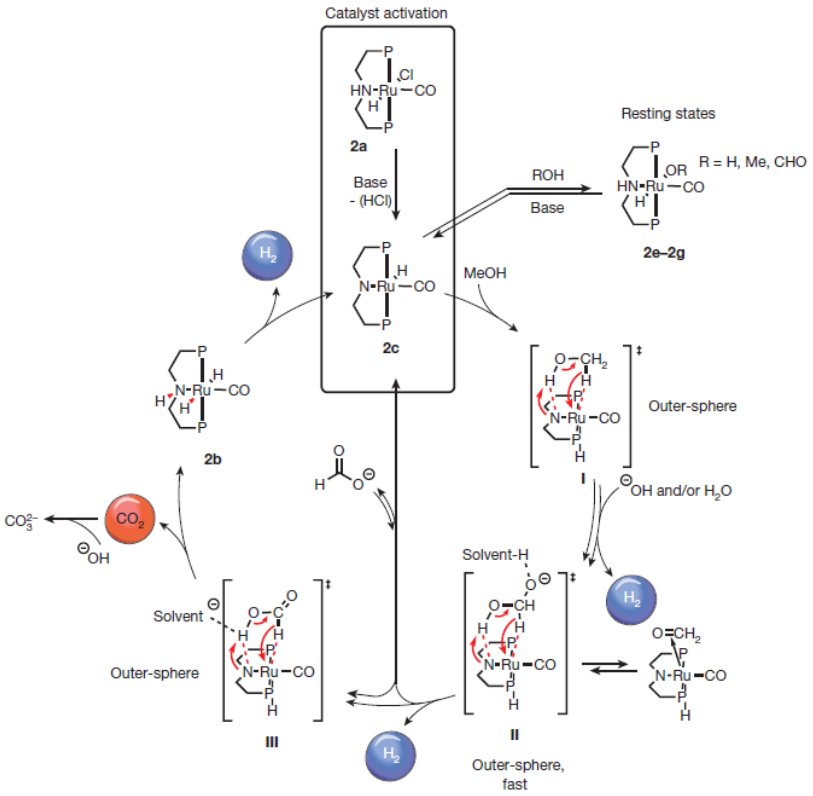

Figure 1.4.4.1. Proposed mechanism for complete methanol dehydrogenation with RuH(PNP). Reproduced from ref 134.

Later, the same group used the same PNP (MACHO) ligand with iron replacing ruthenium.[135] Predictably, the activity was reduced, although this demonstrated for the first time that iron was capable of dehydrogenation of an alcohol, much less methanol. The group was capable of producing TOF exceeding 600 h^{-1} over three hours at 91^0C. The catalyst requires high concentrations of base (8.0 M KOH) to provide reasonable TOFs. The catalyst was capable of producing TON of approximately 10 000 in a two day range, although catalytic activity was halted after that point. Interestingly, free ligand was detected during the course of the experiment, so the group attempted to increase catalyst lifetime by adding excess ligand. While the catalyst's lifetime increased to over 100 h, the activity was reduced to the point where TON were within 10%, and the un-spiked experiment was more robust (see Table 1.4.4.1)

The Grützmacher group developed a Ru(H)(trop$_2$dad) complex, capable of a high initial TOF (initial TOF = 24 000 h^{-1}).[136] In a MeOH/H_2O mixture at 90^0C, the active catalyst undergoes a Ru^{II}-Ru^0 redox couple, capable of fully oxidizing MeOH to CO_2, trapped as carbonate in basic reaction conditions. Long term experiments provided a strong 84% yield, although high catalyst loading was required, as the total turnover number in 10 hours was 540. Once again, while activity with formic acid has been directly observed, no evidence of formaldehyde production or dehydrogenation was found during MeOH dehydrogenation. The group was able to isolate a series of intermediates which suggests that the diazodiene backbone is an active participant in catalysis, being reduced into diazodiamine by accepting protons and electrons from methanol and methanediol. In base-free conditions, a proton acceptor is able to dehydrogenate the diazodiamine to produce one molecule of H_2 and reform the Ru-H catalyst (Figure 1.4.4.2).

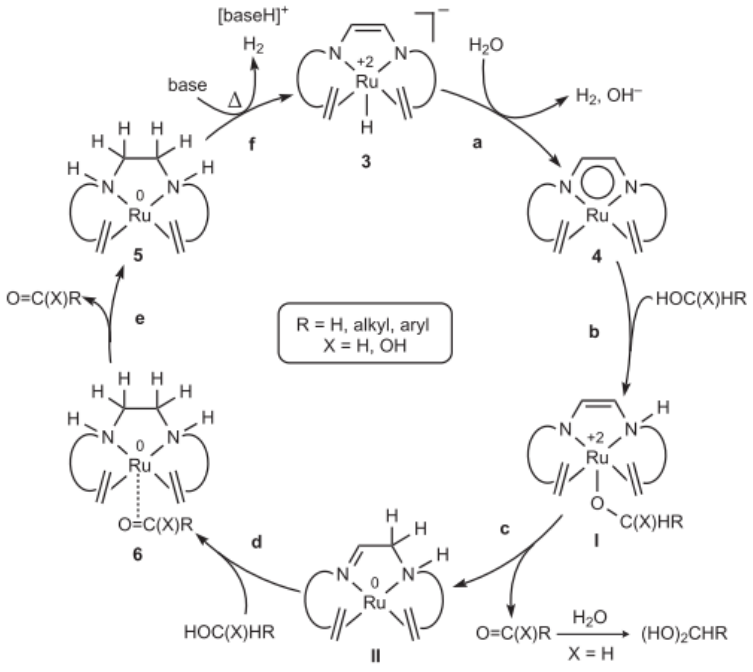

Figure 1.4.4.2. Proposed pathway for dehydrogenation of methanol and methanediol using Ru(H)(trop$_2$dad). Reproduced from ref 136.

The Milstein group has studied a recoverable Ru-PNN catalyst capable of 77% yields of H_2 from MeOH in basic conditions at 100^0C with toluene and water as co-solvents.[137] While TOF is limited (45 h^{-1}), the catalyst loses no activity post-recovery after three separate 9 h cycles, and was able to produce a TON of ~30 000.

More recently, Beller's group investigated the use of a bi-catalytic combination of a series of Ru(PNP)(CO) complexes and $RuH_2(Ph_2PRPPh_2)$ complexes at 93.5^0C.[138] The bi-catalytic system was developed to eliminate the need for the addition of base for MeOH dehydrogenation. In the best system, using Ru-MACHO-H and $Ru(H)_2(dppe)_2$, was capable of > 4200 turnovers in 8 days, with a yield of 26%, with a far more impressive initial TOF of 87 h^{-1}, which appeared stable for 24 hours before slowly decaying. . The bi-catalytic system exhibited a positive synergistic effect, as the combination of the best Ru-MACHO and $RuH_2(Ph_2PRPPh_2)$ catalysts was more active than the sum the two individually (Figure 1.4.4.3).

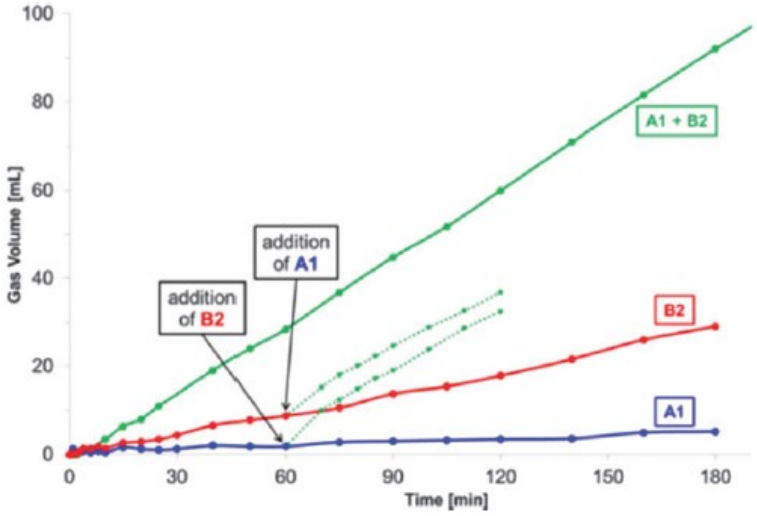

Figure 1.4.4.3. Base-free dehydrogenation of methanol catalyzed by A1 (Ru-MACHO-H), B2 ($RuH_2(dppe)_2$), and combination of both (A1+B2). Reproduced from ref 158.

Very recently, Crabtree tested the thermal dehydrogenation of methanol with a series of Ir N-heterocyclic carbene catalysts.[139] When reacted with 6.7 M KOH at 91^0C, the best systems, utilizing IMes ligands, were capable of producing TON of 8000 in dry MeOH in inert atmospheres, and 375 when combined with 10% H_2O. Interestingly, formate ions were the major carbon product, making up 95% of the carbon products, with the remaining 5% being (bi)carbonate. These catalysts were also capable of transfer hydrogenation of aldehydes and immines, as well as methylation of aniline, both with methanol as a reactant.

1.4.5 Outlook

Although low-temperature dehydrogenation of methanol has been known since the 1980s, it was not until 2010 that promising methods for methanol dehydrogenation as a reasonable energy source were developed. It will be interesting to track the comparison of heterogeneous photocatalysts and homogenous catalysts as the prime method for hydrogen production from methanol.

Heterogeneous catalysts have the advantage of stability and the ability to filter and recover the catalysts from a spent system. Furthermore, the requirement for hydroxide bases are less ubiquitous for heterogeneous photocatalysts than their homogeneous counterparts, which may lead the way to effective base-free H_2 storage systems. Unfortunately, the catalytic activities of heterogeneous photocatalysts are severely lacking and must be improved before they are commercially comparable to high temperature steam reformation. For many of these catalysts, the fate of oxidized methanol is not studied, whether the final product is CO_2 (or carbonate), formic acid (or formate), formaldehyde, or one of many possible adducts of each of these potential products is largely unknown.

As expected, homogeneous catalysts have an advantage in rapid and overall activity, as evidenced by the TOFs routinely 1000x greater than their heterogeneous counterparts. However, the homogeneous catalysts typically use expensive platinum group catalysts, expensive phosphine ligands, and severely reduced lifetimes. An active area of research into the homogeneous catalysts has focused on reducing, or eliminating the use of high concentrations of hydroxide bases. These required additives add both cost and weight to a prospective hydrogen storage system.

With the exception of the very recent Crabtree Ir-NHC catalysts, all homogeneous catalysts fully dehydrogenate MeOH into CO_2. In order to produce pure H_2, the CO_2 must be trapped. Of course, in basic media, CO_2 will be trapped as carbonate, but this requires the utilization of costly hydroxides in stoichiometric quantities. In the case of the Ir-NHC catalysts, the opportunity for production of pure H_2 is a possibility as the vast majority of oxidized methanol is trapped as formate. Tuning the catalysts may yet provide the production of only H_2 and formate, although the cost of NHC ligands, relatively high temperatures, and basic environment may be too much for successful commercialization.

The youth of the field of methanol dehydrogenation as a H_2 storage medium allows for an optimistic outlook into whether commercially relevant catalysts can be developed, although much work remains to be done.

1.5 Formaldehyde dehydrogenation

1.5.1 Background

Solid paraformaldehyde (*p*-FA) has an 6.7 wt% content of H_2 while its hydrated form (methanediol) has a 8.4 wt% of H_2.[140] The equilibrium is highly favouring the hydrated form in

the presence of water, so for the purpose of hydrogen storage, total dehydrogenation results in the production of 2 eq. of H_2 and 1 eq. of CO_2. In contrast, anhydrous formaldehyde dehydrogenation produces a single eq. of H_2 and 1 eq. of CO. For the use in fuel cells, this reaction must be avoided both to improve H_2 efficiency, but also to prevent the formation of CO, a fuel cell poison.[140]

The earliest observations of hydrogen evolution from formaldehyde date back to 1887 with the observation of the presence of H_2 in formaldehyde solutions in combination with large excesses of NaOH.[141] The reaction was later clarified to be caused by an intermediate of the Cannizzaro reaction interacting with water to produce formate and hydrogen at low concentrations of formaldehyde and high concentrations of sodium hydroxide.[142,143] Despite these early observations, the use of formaldehyde as a potential source of hydrogen was not discussed until very recently.

1.5.2 Dark heterogeneous formaldehyde dehydrogenation

In 2008, Bi and Lu were the first to propose the use of formaldehyde as a hydrogen carrier for energy usage.[144] They used a series of metal nanocatalysts in basic conditions to dehydrogenate formaldehyde at room temperature. The copper catalyst was the most rapid in terms of hydrogen production, providing a 29.5 mL min^{-1} g_{cat}^{-1}, compared to gold`s 26.1 mL min^{-1} g_{cat}^{-1}. However, in terms of TOF, Au is preferable to Cu (13.8 h^{-1} and 5.02 h^{-1}, respectively) over the span of 100 min. The authors expect sodium formate to be the only carbon-based product, although their claim was never substantiated. The heterogeneous catalyst was recyclable, although lost approximately 10% of its activity in every successive reaction.

Table 1.5.2.1 Formaldehyde dehydrogenation by dark heterogeneous catalysts

Catalyst	H_2 flow rate (ml min^{-1} g^{-1})[b]	TOF (h^{-1})[b]	Ref
Cu nano-catalyst	29.5	5.02	[144]
Au nano-catalyst	26.1	13.8	[144]
Pt nano-catalyst	16.9	8.41	[144]
Ni nano-catalyst	4.1	0.64	[144]
Ag nano-catalyst	163.5	47.3	[145]
Pd nano-crystals	72.9	20.8	[146]
Pd nanotubes	167.6	47.6	[146]
Ag/γ-Al_2O_3	414	113	[147]
3% Au/$SrTiO_3$[c]	0.005	0.023	[148]
3% Au/$SrTiO_3$[c,d]	0.021	0.101	[148]

[a] Unless otherwise noted, all reactions at performed at 25 ^{0}C in water with 0.48 M CH_2O, 1M NaOH, producing only sodium formate and hydrogen. [b] Rates are average over the course of 100 minutes. [c] Reaction performed at 35 ^{0}C in water with 1.5M CH_2O. [d] Biomass assisted synthesis,

Later, the Lu group also tested Ag nanocatalysts for the same reaction.[145] The silver catalyst is an improvement on the prior catalysts, with hydrogen production rates of 163.5 mL min^{-1} g_{cat}^{-1} with the same reaction conditions. This corresponds to TOF of 47.3 h^{-1}. The catalyst is very stable over 9 hours of activity.

In 2014, the Lu and Bi group continued to expand the library of known formaldehyde dehydrogenation catalysts. They tested Pd nanotubes, as well as Ag/Al_2O_3 in the same reaction conditions as before.[146,147] The Pd nanotubes behaved similarly to the previous Ag nanocatalysts, with a TOF of 47.6 h^{-1}, while the Ag/Al_2O_3 catalysts provided the best yet TOF of 113 h^{-1}, with an impressive 414 mL min^{-1} g_{cat}^{-1} observed. In the Pd reactions, the group detected formate release by FTIR, although the amount was not quantified, and the reaction was not repeated

when testing Ag/Al_2O_3 catalysis. Both catalysts were entirely inactive with formic acid and methanol.

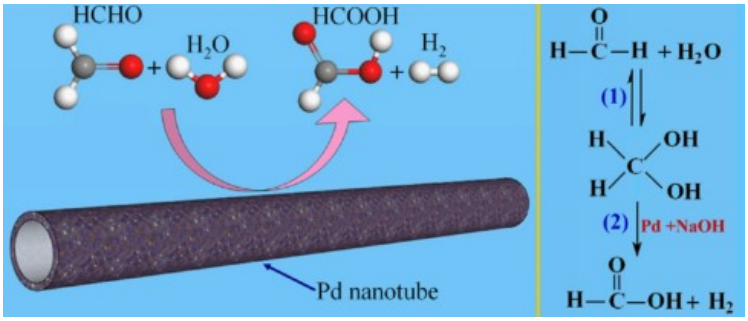

Figure 1.5.2.1. Overview of formaldehyde dehydrogenation over Pd nanotubes. Reproduced from ref. 146.

The Jia group tested $SrTiO_3$, with Au deposited three different ways. When photodeposited from solution, the catalyst was inactive at formaldehyde dehydrogenation. However, when chemically deposited from a glucose solution, the catalyst was able to dehydrogenate formaldehyde, at a low TOF of 0.023 h^{-1}. Interestingly, when glucose was replaced by the extract of syzygium, the catalyst experienced greater than a fourfold increase in activity (TOF = 0.101 h^{-1}). This catalyst was capable of complete dehydrogenation of formaldehyde into CO_2 and 2 eq. of H_2, and did so without the addition of any base. XPS data shows that the photodeposited Au was entirely in the zero valence state, while the chemically deposited Au samples contained both Au^0 and Au^I molecules. In addition, the percent of Au^I detected by XPS in the biomass-assisted deposition is more than 3x greater than that of the glucose-assisted deposition (45.5% vs 14.6%). The group suggests that Au^I is active in the oxidation of formaldehyde. Both active catalysts are stable at a constant rate for >5 h, suggesting the dehydrogenation is not a stoichiometric reaction (far more than 1 turnover with respect to Au^I was produced).

1.5.3 Heterogeneous photocatalytic formaldehyde dehydrogenation

Table 1.5.3.1 Formaldehyde dehydrogenation by heterogeneous photocatalysts

Catalyst	pH	Light source	H_2 flow rate (mL min^{-1} g^{-1})	TOF (h^{-1})	Ref
0.25% Pt/TiO_2	7	Solar simulator	2.9	0.139	[149]
0.25% Pt/TiO_2	8.5	Solar simulator	2.85	0.137	[149]
0.25% Pt/TiO_2	4	Solar simulator	2.1	0.101	[149]
$LaCo_{0.7}Cu_{0.3}O_3$	n.r.	125 W Xe	0.11	0.074	[150]
$LaCo_{0.7}Cu_{0.3}O_3$[b]	n.r.	125 W Xe	0.43	0.284	[150]
Cu_2O (110 facets)	n.r.	50 mW/cm^2 Xe	0.014	0.0024	[151]
Cu_2O (111 facets)	n.r.	50 mW/cm^2 Xe	0.011	0.0018	[151]

[a] All reactions performed at room temperature, unless otherwise noted, [b] Biomass assisted synthesis, [c] Reaction performed at 35 ^{0}C.

While Bi and Lu were testing their series of transition metal nano-catalysts in basic media at room temperature to catalyze the energetically favorable formaldehyde dehydrogenation to sodium formate, other groups began testing photocatalysts that could use formaldehyde as a sacrificial hole acceptor. The Ray group tested 0.25% Pt/TiO_2 photocatalysts (using a 1 kW solar simulator) in acidic, neutral and basic conditions.[149] The group found little difference in activity in neutral and basic conditions (TOF = 0.139 h^{-1} and 0.137 h^{-1}, respectively), although activity was reduced in acidic media (0.101 h^{-1}). However, to our knowledge, this is the first example of hydrogen production from formaldehyde in acidic conditions.

More recently, the Jia group tested photocatalytic hydrogen production from $LaCo_{0.7}Cu_{0.3}O_3$, although activities proved to be low.[150] Similar to Au-$SrTiO_3$, the catalyst exhibited increased activity when prepared alongside biomass extracts. The activity of $LaCo_{0.7}Cu_{0.3}O_3$ increased from 0.074 h^{-1} to 0.284 h^{-1}. The group speculates that oxygen vacancies promoted by the

biomass-assisted syntheses activate formaldehyde. Although another likely cause for the increased activity is a reduced band-edge energy for the microbial synthesis (Figure 1.5.3.1).

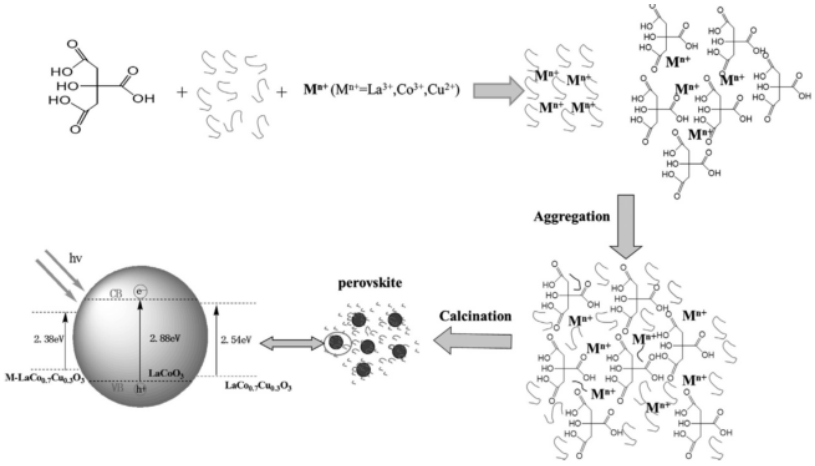

Figure 1.5.3.1. Proposed pathway for biomass assisted formation of $LaCo_{0.7}Cu_{0.3}O_3$ (denoted as M-$LaCo_{0.7}Cu_{0.3}O_3$). Reproduced from ref. 150.

The Wang group tested the effect of Cu_2O exposed crystal facets in photocatalytic formaldehyde dehydrogenation into formate. The authors determined that the 110 facet crystal is likely the active site where dehydrogenation occurs (TOF = 0.381 h^{-1} and 0.286 h^{-1} for 110 and 111 facets, respectively). By monitoring the reaction progress via EPR, the group detected the formation of hydroxyl radicals which are capable of oxidizing formaldehyde.

1.5.4 Homogeneous formaldehyde dehydrogenation

Table 1.5.4.1. Formaldehyde dehydrogenation by homogeneous catalysts

Catalyst	pH	TOF (h^{-1})	TON	Yield (%)	Temp (^{0}C)	Ref
Ru(*p*-cymene)$_2$(μ-Cl)$_2$Cl$_2$	5.5	104	346	33	95	[140]
Ir(Cp*)(pyrazolyl-benzoic acid)	11	3.6	50.4	2	60	[152]

While heterogeneous formaldehyde dehydrogenation has been actively studied by a few groups since 2008, it wasn't until 2014 that the first example of homogeneous formaldehyde dehydrogenation for the purpose of hydrogen storage was described.

In the first example of homogeneous hydrogen production from formaldehyde, the Prechtl group used a $Ru_2(p\text{-cymene})_2(\mu\text{-}Cl)_2Cl_2$ dimer to efficiently oxidize formaldehyde into 2 eq. of H_2 and CO_2. This catalyst was active at temperatures as low as 65 ^{0}C, although it is more effective at 95 ^{0}C. Also, the catalyst is active at a wide range of pH, but best at a moderately acidic (pH = 5.5) media, modified by the use of a buffer. Interestingly, the active catalyst in slightly acidic conditions hydrolyzes into a tris-hydroxyl bridged dimer. These conditions promote maximum activity, yielding an 84% yield in an hour, although with high catalyst loadings (10 mol%). The maximum reported TON was 346 (TOF = 104 h^{-1}), although only providing a 33% yield.

Inspired by the Prechtl group, Fukuzumi used an organoiridium complex containing benzoic acid, pyrazole and hydroxyl ligands to dehydrogenate formaldehyde (Figure 3). While the activity was low, compared to Prechtl's Ru complex (TOF = 1.7 h^{-1} after 14 hours), the catalyst was active at room temperature, although the activity roughly doubled (TOF = 3.6 h^{-1} after 14 hours) at 60 ^{0}C. Interestingly, the catalyst was inactive below a pH of 8, when the hydroxyl ligand was protonated to a water ligand. As seen with the Ru(cymene) catalyst, activity seems to be tied to the formation of metal-hydroxide bonds.

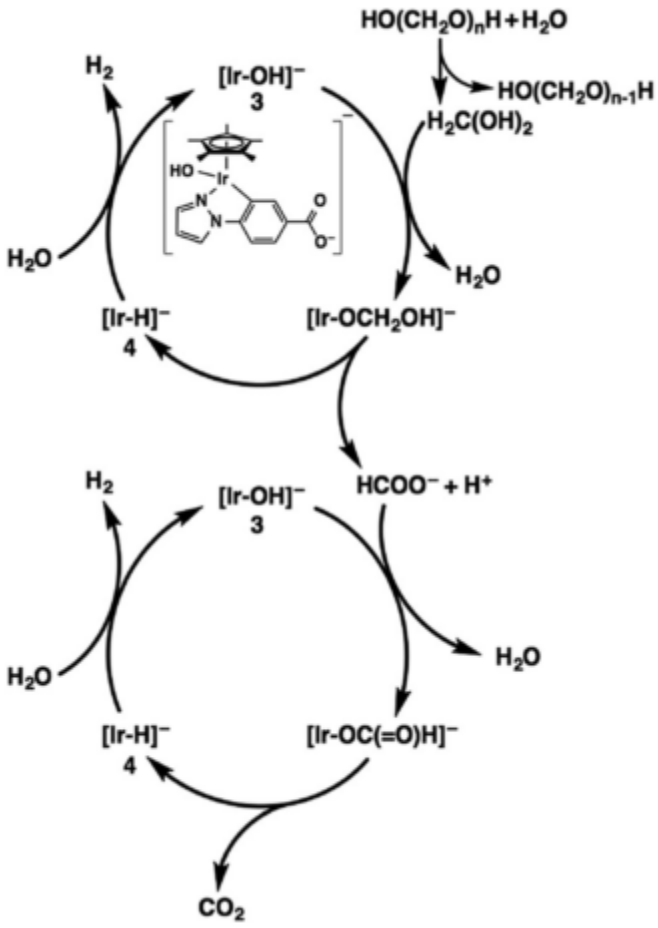

Figure 1.5.4.1. L-Ir-OH catalyzed dehydrogenation of formaldehyde. Reproduced from ref.152.

Both of these homogeneous catalysts provide an intriguing proof-of-concept for formaldehyde dehydrogenation, although the activity and stability of both catalysts are problematic vis-a-vis real applications. One point of further study for homogeneous catalysts is the potential requirement for metal hydroxide bonds in the active catalysts. The activity of other Ru, Ir, and cheaper transition metal catalysts with an active M-OH bond is a possible starting point for further studies into formaldehyde dehydrogenation.

1.5.5 Outlook

Prechtl's catalyst benefits from being commercially available, and relatively low cost. In addition, the ruthenium catalyst compares favorably to Bi and Lu's $Ag/\gamma\text{-}Al_2O_3$ catalyst in terms of TOF, and its activity in base-free conditions. However, the heterogeneous $Ag/\gamma\text{-}Al_2O_3$ catalyst is capable of longer lifetimes, and its activity at room temperature is a major advantage to that of the near reflux conditions from the ruthenium catalyst. Furthermore, the heterogeneous catalyst is capable of producing a pure stream of H_2, while the ruthenium catalyst produces CO_2 in addition to H_2, which may require separation before use in fuel cells.

Bi and Lu have shown that neutral metal nano-catalysts are moderately effective dehydrogenation agents, although the requirement for basic conditions may need to be reduced. Mechanistic studies into the activity of these catalysts may be beneficial to direct future studies into improving these catalysts, or developing new ones.

Heterogeneous photocatalysts are thus far ineffective at hydrogen production using paraformaldehyde as a sacrificial agent. At the moment, these catalysts are unlikely to lead to commercialization, although as the entire field of photochemical water splitting is developed, new techniques may provide new insights for formaldehyde dehydrogenation.

It remains to be seen if homogeneous or heterogeneous catalysts will be more cost-efficient for commercial applications, but the field is very young, and will require a great deal of future research. Ideally, a catalyst should be capable of producing large amount of H_2 that does not need to be purified. In addition, the catalyst should be active at room temperature, or near it, with at most solar energy being used to stimulate hydrogen release. Furthermore, the catalyst should be active in base-free conditions to reduce the production cost.

1.6 Formic acid and Formate dehydrogenation

1.6.1 Background

Formic acid is the most thoroughly studied vehicle for hydrogen storage in single carbon organic molecules. For the purpose of pure hydrogen storage, formic acid and CO_2 are readily interconverted, depending on the pressure of H_2, temperature and pH of the reaction media.[153–156,9,157] This provides an opportunity for formic acid to act as a hydrogen "battery" to be recharged by H_2 produced by conventional means (steam reformation, water electrolysis, etc.). Formic acid is also readily produced by CO_2 reduction photosemiconductors coupled with water oxidation.[8] As a downside, formic acid has a hydrogen storage content of 4.4 wt%, which is less than comparable LOHCs, and limits mobile applications due to weight constraints.[9]

Formic acid decomposition can occur via two pathways, dehydrogenation into CO_2 and H_2, the preferred reaction, or decarbonylation into CO and H_2O. Both reactions are thermodynamically favorable, and the products can interchange at high temperatures via the water-gas shift reaction.[9] Decarbonylation (and the reverse water-gas shift reaction) produce CO, which in addition to reducing the H_2 yield of formic acid decomposition, is a potent poison in fuel cells and must be avoided.

Early studies in formic acid dehydrogenation for hydrogen production focused on heterogeneous catalysts at high temperatures. Unfortunately, these reactions tended to yield high concentrations of CO, and the application of high temperatures further reduces the scope of applications available for formic acid dehydrogenation.[158] Initial studies into homogeneous formic acid dehydrogenation were the result of studies into CO_2 hydrogenation, with the dehydrogenation of

formic acid acting as an unwanted side reaction.[9,157,159] Formic acid as a hydrogen storage vector was not explored until 2008.[160,161]

For the scope of this section, we will focus on formic acid dehydrogenation with the following requirements:

- Operating temperatures < 100 ^{0}C
- atmospheric conditions
- <10 ppm CO produced
- No use of sacrificial agents

In addition, while the catalysts in prior dehydrogenation sections (methanol, formaldehyde) are often capable of dehydrogenating formic acid, the catalysts were not extensively tested for specifically formic acid, and therefore will be not reviewed in the following section.

1.6.2 Homogeneous formic acid dehydrogenation

In 1967, Coffey reported the first examples of soluble catalysts for the dehydrogenation of formic acid (TON >1) into H_2 and CO_2. In a refluxing solution of formic acid in acetic acid, Coffey was able to produce TOF exceeding 1000 h^{-1}, with a TON exceeding 11 000 using $Ir(H)_3(PPh_3)_3$.[162] Coffey proposed that the general reaction cycle has intermediates including metal-carbonyls and –acetates. Further research, from the Yoshida, Shriver, Puddephatt, and Himeda groups, explored the use of homogeneous transition metal catalysts, although they all required temperatures exceeding 100 ^{0}C.[157,159,163,164].

1.6.2.1 Dehydrogenation via formic acid/amine adducts

As one of the initial examples of formic acid dehydrogenation below 100 ^{0}C, the Beller lab screened a series of homogeneous and heterogeneous catalysts for the dehydrogenation of formic acid in the presence of triethylamine as a formic acid/amine adduct.[160] Initially, the most active catalyst was a $RuCl_2$(*p*-cymene) dimer, which was capable of a moderate stable TOF of 7 h^{-1}, but after 24 hours, the activity of the catalyst increased exponentially (TOF ~ 350 h^{-1}), as the ratio of amine:formate augmented. The catalyst remained active after full conversion of formic acid was obtained. However, the Beller group continued to test $Ru(PPh_3)_3Cl_2$ in the same conditions, and were able to avoid the long induction period, and capable of an initial TOF of 2688 h^{-1} with DMF as a solvent, although the catalyst's activity was rapidly halted, producing only 893 turnovers in 3 hours, with a modest 8.9% yield.

The Beller group, among others, would later improve the activity of formic acid/amine dehydrogenation catalysts.[165,166] However, the addition of amines as a requisite co-catalyst increases the cost of dehydrogenation, but more crucially, dilutes the formic acid enough to reduce the theoretical wt% of H_2 below relevant storage levels. In 2012, the groups of Beller and Laurenczy jointly obtained a reversible Ru-dppe battery for hydrogen storage and release.[153] The reaction was favored in either direction simply by modifying the system pressure. The Ru catalytically active species was formed *in situ* in the presence of hexyldimethylamine as an amine adduct demonstrated to be of pivotal importance for the reactivity. The dehydrogenation reaction was tested under flow conditions at 80 ^{0}C, and was capable of producing a stable TOF of nearly 48,000 h^{-1} while maintaining a yield of 50% capable of a TON of 800,000, with respect to H_2 release. However, despite a then-record formic acid:amine ratio of 2.69, the hydrogen

content was limited to approximately 1 wt%, far too low compared to pure formic acid (4.4%), commercial solutions of formaldehyde (5%), and methanol (12.6%).

For these reasons, the rest of the review will disregard the use of formic acid/amine adducts as meaningful media for hydrogen storage.

1.6.2.2 Homogeneous dehydrogenation with ruthenium catalysts

Table 1.6.2.2.1. Formic acid dehydrogenation by Ru-based homogeneous catalysts.

Catalyst	**Additive**	**TOF (h^{-1})**	**TON**	**Temp (^0C)**	**Yield (%)**	**Ref**
$[Ru(H_2O)_6](toluene\text{-}4\text{-}sulfonate)_2$	2 eq TPPTS	80	200	70	95	[161]
$[Ru(H_2O)_6](toluene\text{-}4\text{-}sulfonate)_2$	2 eq TPPTS	230	n.r.	100	n.r.	[161]
$RuCl_3$	2 eq $MDAPhPPh_2$-BF	1430[a]	357	90	95	[167]
$RuCl_3$	2 eq TPAMPhP-BF	1130[a]	357	90	95	[167]
$RuCl_3$	2 eq TPAMPhP-BF	n.r	10,000	90	n.r.	[167]
Ru-MACHO-BH	dioxane	663	994	84	99.4	[156]

[a]TOF calculated after 5th cycle.

In the same issue as Beller's first example of a formate dehydrogenation catalyst, the Laurenczy lab published the first example of a selective and stable homogeneous catalyst for formate dehydrogenation without the use of an amine adduct. The Laurenczy lab developed an *in situ* generated Ru-phosphine catalyst (from $[Ru(H_2O)_6](toluene\text{-}4\text{-}sulfonate)_2$ and *meta*-trisulfonated triphenylphosphine, TPPTS) capable of dehydrogenation of 10 mmoles of formate (0.5 mol% Ru) with a 95% yield after 2.5 hours at 70 ^0C (TOF ~ 80 h^{-1}). Rapid dehydrogenation in less than 30 minutes was achieved under hydrothermal conditions. The lab also tested the reaction with a continuous addition of formic acid, obtaining a stable TOF of 230 h^{-1} at 100 ^0C.

The Laurenczy group continued their investigation of the Ru/TPPTS system by proposing a competing bicyclic mechanism for H_2 production.[168] In this study, they observed that the activity for pure formic acid decomposition is slow, but it is rapidly catalyzed by the addition of sodium formate. This suggests the activation of the Ru catalyst requires deprotonated formic acid to bind, prior to β-elimination of the formyl hydrogen. The second cycle of the reaction will later be denoted as the "slow" cycle, while the "fast" cycle would be remodelled later (Figure 1.6.2.2.1).

In 2014, the group modified their interpretation of the "fast" cycle.[169] The pro-catalyst initially enters the "fast" cycle, but after dissociation of one of the three phosphine ligands, it can pick up a second aqua ligand, which sets a stable octahedral complex which is slow to react with formic acid (**6**). On the other hand, if the phosphine ligand returns and replaces the CO_2 ligand, the catalyst continues in an alternating 5/6 coordinate cycle which rapidly oxidizes formic acid. Two key steps in the fast cycle include the β-elimination of the formyl ligand, leading to complex **7**, and the formation of dihydrogen via hydride migration from complex **5a** to complex **8**.

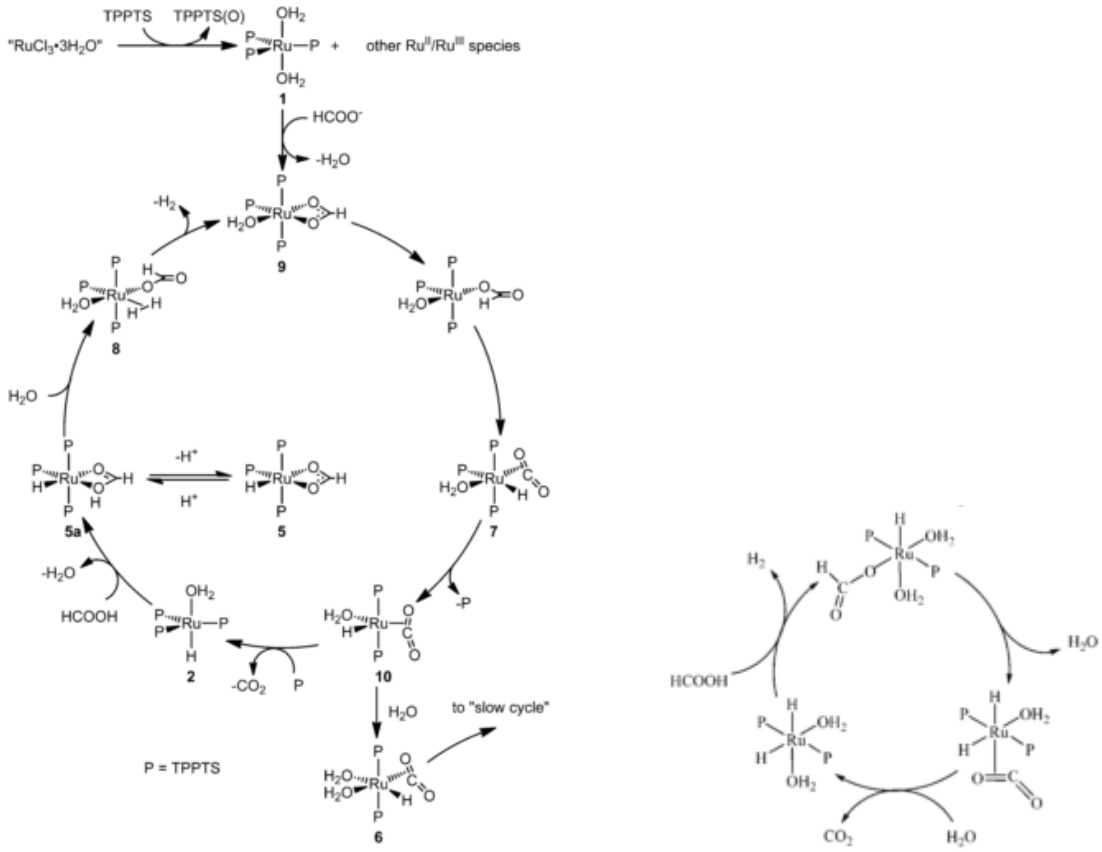

Figure 1.6.2.2.1: Proposed mechanism for the "fast" and "slow" cycles for sodium formate catalyzed formic acid dehydrogenation using Ru-TPPTS. "Fast" cycle is reproduced from ref. 168. "Slow" cycle is reproduced from ref. 169.

The Laurenczy group also investigated the use of cationic amino-substituted triphenylphosphine ligands with Ru^{II}.[167] The most active system utilized a ligand **4** (MDAPhPPh$_2$-BF) in Figure 2, which was capable of a TOF of 1430 h^{-1} at 90 ^{0}C with quantitative yields, although activity was largely the same with only bis-amino substituted ligands. The catalyst was recyclable, and capable of multiple additions of formic acid to provide a TON exceeding 10,000 with ligand **3A** (TPAMPhP-BF) in Figure 1.6.2.2.2. Additional amino-substitution resulted in a severe decrease in activity (TOF < 150 h^{-1}), which was speculated to be an effect of increased steric bulk, although this effect was not investigated further.

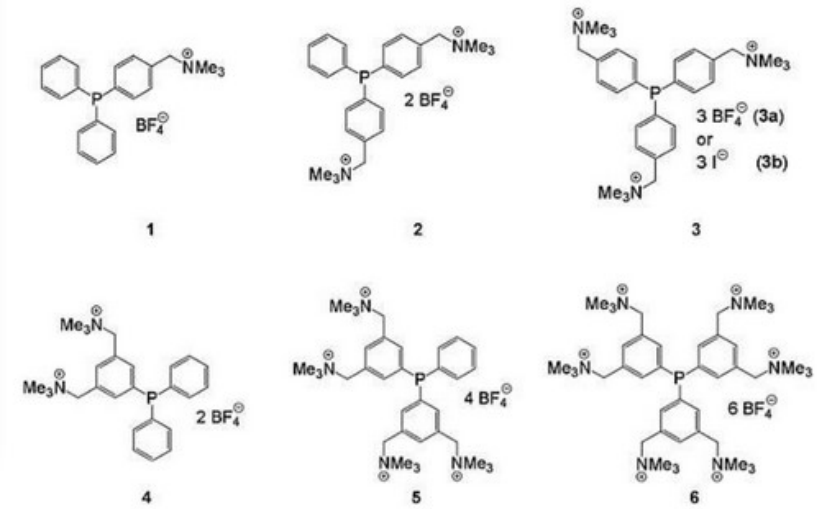

Figure 1.6.2.2.2. Ligands used by Laurenczy, *et al*. for dehydrogenation of formic acid with ruthenium. Reproduced from ref. 167.

Recently, the Olah and Prakash groups demonstrated the use of commercially available Ru-PNP complexes for amine-free reversible formate dehydrogenation.[156] While the catalyst was capable of several dehydrogenation/hydrogenation cycles simply by changing pressure and temperatures, the carbonate hydrogenation reaction required a 3x excess of H_2 gas to produce yields in excess of 90%. As a pure dehydrogenation catalyst, Ru-MACHO-BH (carbonylhydrido{tetrahydroborato}[bis-{2-diphenylphosphinoethyl}amino]ruthenium{II}) is capable of 994 turnovers with an average TOF of 663 h^{-1} over 90 minutes at 84 ^{0}C for a quantitative yield of H_2 (20 mmol). The catalyst is fully active over at least 6 dehydrogenation/hydrogenation cycles. The amine function of the PNP ligand is non-innocent and is able to hold onto a proton required for coupling to a hydride ligand for H_2 release (Figure 3).

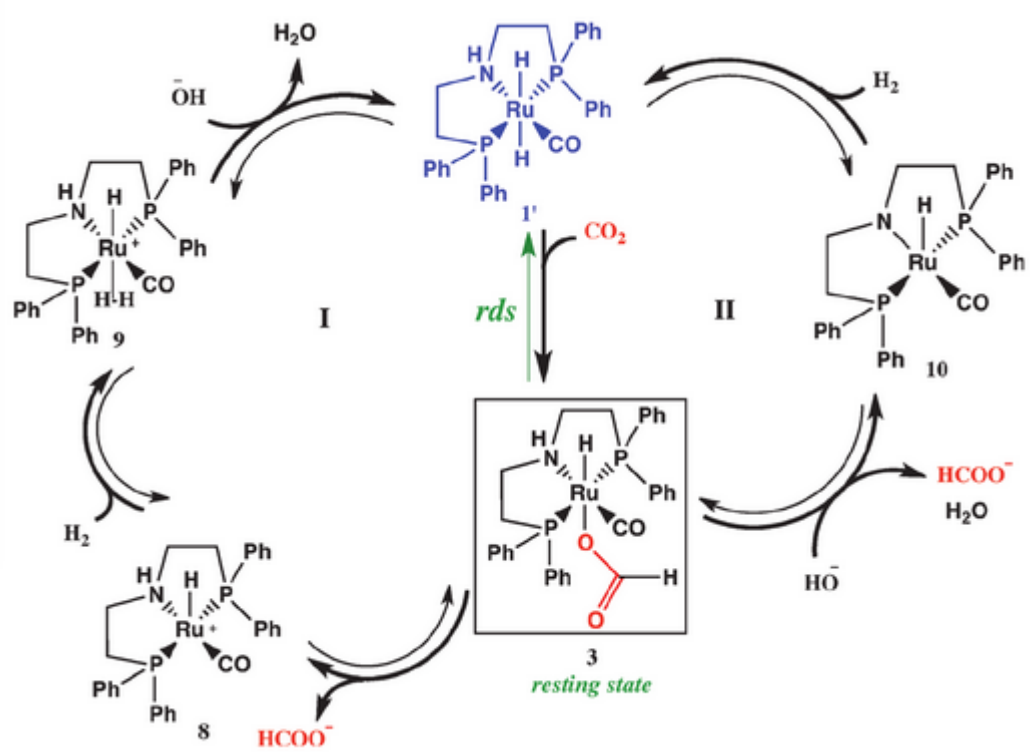

Figure 1.6.2.2.3. Proposed mechanism for reversible formic acid dehydrogenation using Ru-MACHO. Reproduced from ref. 156.

1.6.2.3 Homogeneous dehydrogenation with iridium catalysts

Table 1.6.2.3.1. Formic acid dehydrogenation by Ir-based homogeneous catalysts.

Catalyst	Initial TOF (h^{-1})	TON	Temp (^{0}C)	Yield (%)	Ref
Ir(Cp*)(H_2O)(4DHBP)	2400	5000	60	100	170
Ir(Cp*)(H_2O)(6DHBP)	39,500	11,000	80	55	171
Ir(Cp*)(H_2O)(4,6THBPM)	19,800	30,000	90	100	171
[Ir(Cp*)(H_2O)]$_2$(μ-4,6THBPM)	12,000	20,000	50	100	154
[Ir(Cp*)(H_2O)]$_2$(μ-4,6THBPM)	158,000	308,000	80	46	154
Ir-bisMETAMORPhos[a]	3092	n.r.	85	n.r.	172
Ir(Cp*)(H_2O)(imim)	182	250	37	100	155
Ir(Cp*)(H_2O)(phenpzCO_2H)	295	250	37	100	155

[a] Reaction performed in toluene

In 2009, Himeda studied Ir(Cp*)(H_2O) catalysts with 4,4'-dihydroxy-2,2'-bipyridine (4DHBP), and were capable of and initial TOF of 14,000 h^{-1} and nearly quantitative yields at 90 ^{0}C.[170] This was later improved as Himeda and co-workers in 2014 explored the ability of Ir(Cp*)(H_2O) catalysts by testing a wider series of bipyridine based ligands.[171] The most active for formate dehydrogenation was a 4,4',6,6'-tetrahydroxy-2,2'-bipyrimidine (4,6THBPM) cased catalyst, with an initial TOF of 39,500 h^{-1}, although it quickly decomposed, and was unable to exceed 11,000 turnovers. However, the use of 6,6'-dihydroxy-2,2'-bipyridine (6DHBP) had an initial TOF of 19,800, and able to quantitatively dehydrogenate 30,000 turnovers of formic acid in less than 5 hours. The group also explored the mechanism by using kinetic isotope experiments, concluding that the rate determining step for reactions with 6,6' hydroxyl ligands is the β-elimination of formate, while ligands without the 6,6' hydroxides are instead limited by the metal hydride extraction by water (Figure 1.6.2.3.1).

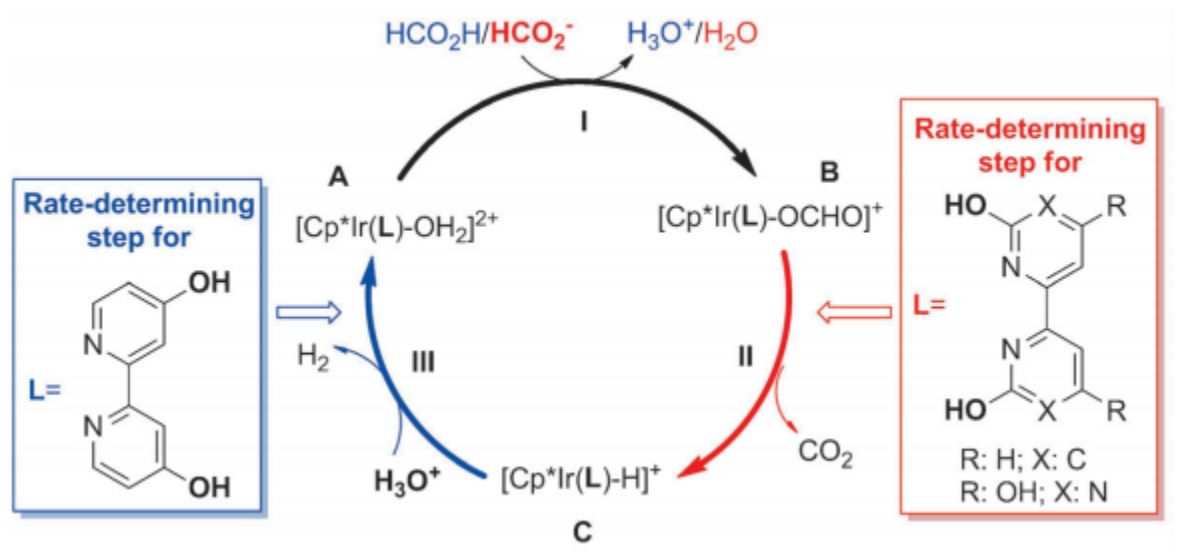

Figure 1.6.2.3.1. Summary of formic acid dehydrogenation from Ir(Cp*)(H_2O)(bipyridine) catalysts, noting the rate determining steps for different bipyridine ligands. Reproduced from ref. [171].

Himeda and co-workers also tested the 4DHBP ligand with Ru(C_6Me_6) and Rh(Cp*), and were capable of achieving full dehydrogenation of formic acid, although their activities were reduced (initial TOF for Ir = 2400 h^{-1}, Rh = 440 h^{-1}, Ru = 36 h^{-1} in tested conditions).[173]

Hull and co-workers developed a reversible dehydrogenation catalyst, triggered by pH and H_2 pressure changes.[154] On the dehydrogenation side, the group used a dimerized [Ir(Cp*)(H_2O)]$_2$(μ-4,6THBPM), which is capable of quantitative production of H_2 with 5 mmol% catalyst loading at 60 ^{0}C. The catalyst provided an improved TON of 20,000 in 4 h (compared to previous work from Himeda), although it was slower, with an initial TOF of 12,000 h^{-1}. When catalyst loading is decreased to 0.15 mmol% and temperature increased to 80 ^{0}C, a TON of 308,000 (initial TOF = 158,000 h^{-1}) is possible in 12 hours, although yield is reduced to just 46%.

The Reek group developed an Ir catalyst with an intrinsic base, which removed the requirement to add external bases for catalysis.[172] The ligand used in this system is bisMETAMORPhos (Figure 1.6.3.2.2), and is capable of TOFs exceeding 3000 h^{-1} in either dioxane or toluene at 85 ^{0}C without the production of CO.

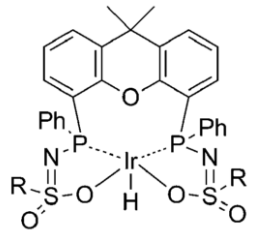

Figure 1.6.2.3.2. Ir-bisMETAMORPhos catalyst. Reproduced from ref. 172.

Later, the same group elaborated on the mechanism of the bisMETAMORPhos ligand's effect on formic acid dehydrogenation via experimental and DFT data. As expected, the sulfonamide unit

of the ligand plays a major role. The nitrogen coordinates with the acidic hydrogen of formic acid, while the iridium cleaves the formyl hydrogen to produce a hydride ligand (and releasing CO_2). Interestingly, the nitrogen is then deprotonated by an additional atom of formic acid, while the acidic proton coordinates with the iridium hydride and is released as H_2 (Figure 1.6.2.3.3).

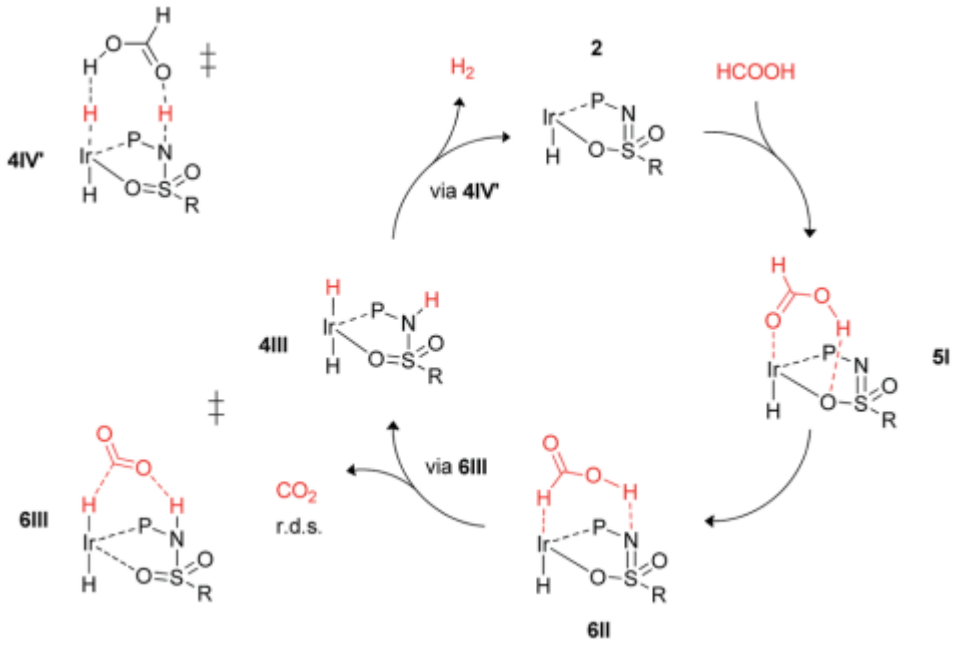

Figure 1.6.2.3.3. Proposed mechanism for formic acid dehydrogenation via Ir-bisMETAMORPhos. Reproduced from ref. 174.

The Ward group tested a series of Ir(Cp*)-bidentate ligand catalysts.[155] Their best catalysts using one of (4-(pyrazol-1-yl))benzoic acid, phenpzCO_2H) or (2,2-bis(4,5-dimethylimidazole), imim) ligands were capable of yields just shy of 100% in 150 minutes. When formic acid was added in regular ~2 h intervals, the catalysts were capable of total TON of 3650 and 8700, respectively, in 48 hours. The initial TOF of the catalysts were comparatively low at 294 and 182 h^{-1}, respectively. Promisingly, each catalyst was equally active in N_2 and air.

1.6.2.4 Homogeneous dehydrogenation with iron catalysts

Table 1.6.2.4.1. Formic acid dehydrogenation by *in situ* generated Fe-based homogeneous catalysts.[a]

Iron precursor	Solvent	TOF (h^{-1})	TON	Ref
$Fe(BF_4)_2 \bullet 6H_2O$[b]	PC	5805	92417	[175]
$Fe(BF_4)_2 \bullet 6H_2O$	PC	647[c]	1942	[176]
$Fe(BF_4)_2 \bullet 6H_2O$	THF	183[c]	549	[176]
$Fe(BF_4)_2 \bullet 6H_2O$	none	1.2[c]	3.7	[176]
$Fe(acac)_2$	PC	626[c]	1879	[176]
$Fe(acac)_3$	PC	648[c]	1943	[176]
$Fe(ClO_4)_2 \bullet 6H_2O$	PC	500[c]	1500	[176]
$Fe(ClO_4)_3 \bullet 6H_2O$	PC	472[c]	1418	[176]

[a] Reaction performed at 40 ^{0}C with 2 equivalents of PP_3, unless otherwise noted. [b] Reaction performed under continuous flow conditions at 80 ^{0}C, with 3 equivalents of PP_3. [c] average TOF after 3 hours.

The advantage of using iron catalysts is easily apparent. Iron is cheap, abundant and relatively non-toxic. It is in fact, the active catalyst in many organisms which use H_2 as an energy source.[175] Unfortunately, as of now, the literature for iron catalyzed formic acid dehydrogenation is limited to two papers, both from the Beller group.

Beller and co-workers developed an *in situ* generated Fe-H (tris[2-(diphenylphosphino)ethyl]phosphine, PP_3) catalyst for stable and efficient formic acid dehydrogenation in propylene carbonate (PC) without any additives.[175] The catalyst was most active when 4 eq. of the ligand were added (maximum TOF = 9425 h^{-1}). Impressively, after a

short (~1 hr) induction period, the catalyst was stable under continuous addition of formic acid for more than 15 hours with quantitative yields, for a TON exceeding 92,000.

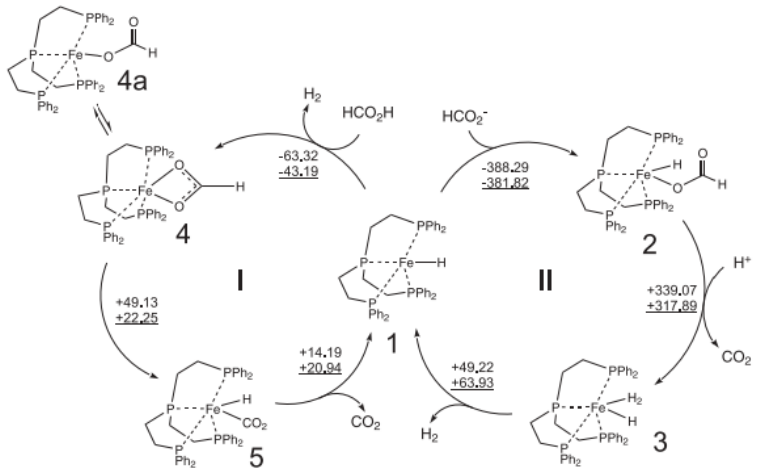

Figure 1.6.2.4.1. Proposed mechanism for formic acid dehydrogenation using *in situ* generated Fe-PP_3 catalysts. Relative energy change of each reaction provided in each step, calculated from B3PW91/6-31G and B3PW91/6-311G theories. Reproduced from ref. 175.

Later, the combined Beller, Laurenczy, and Ludwig groups expanded the scope of *in situ* generated Fe-PP_3 catalysts.[176] The activity, decomposition and selectivity of the catalysts depended on both the choice of iron precursor and solvent. While screening with the addition on PP_3 to various Fe precursors, the group found that the use of acetylacetonate (acac) or chlorate precursors produced quantitative yields of CO-free H_2 (TON ~ 1900 after 3 hours), while the use of acetate and carbonyl precursors were less active, while also yielding > 50 ppm of CO. Meanwhile, the presence of chloride salts promoted the formation of stable and inactive $Fe(PP_3)Cl_{1/2}$ species, deactivating the catalyst.

Finally, these catalysts were highly solvent dependant. Water was a poison to the catalyst, and additionally activity increased from 3.7 turnovers in neat formic acid, to 549 in THF to 1942 in

propylene carbonate. Additionally, the effect of adding excess PP_3 showed a significant increase in activity when using 2 eq of ligand vs 1 (TON_{2h} = 6244 and 523, respectively).

1.6.3 Heterogeneous formic acid dehydrogenation

In the following section, the use of metallic catalysts on heterogeneous supports is explored. As alluded to earlier, heterogeneous catalysts traditionally produce CO as a by-product in a competitive decomposition pathway. In each of the following examples, palladium is the active catalyst for dehydrogenation, often alloyed with a noble metal to control the reaction pathway.

In 2014, the Mullins group conducted a study on the surfaces of Pd, Au and Pd/Au catalysts.[177] They determined that while Pd surfaces are the active center for formic acid decomposition, the adjacent atoms are crucial in the identity of the decomposition product. Specifically, if Pd surfaces are adjacent to the activated formic acid, dehydration into CO and H_2O would be favored, while if Au surfaces are adjacent to the active Pd-COOH catalyst, dehydrogenation into H_2 and CO_2 is preferred (Figure 1.6.3.1).

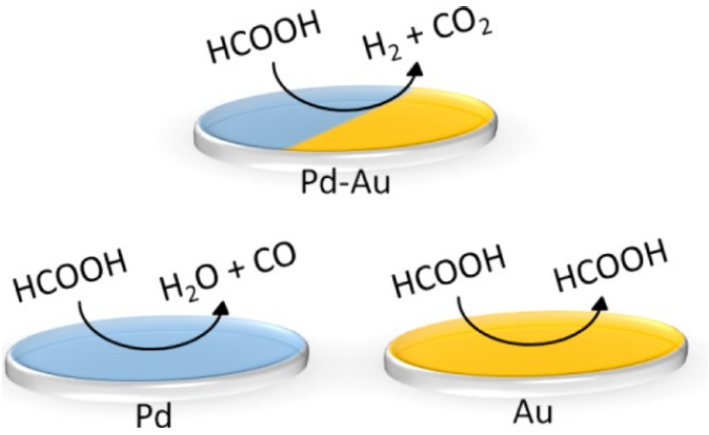

Figure 1.6.3.1. Schematic of energetically favorable formic acid decomposition pathways on the surfaces of unsupported Pd, Au and PdAu nanocatalysts. Reproduced from ref. 177.

Table 1.6.3.1. Formic acid dehydrogenation by heterogeneous catalysts.

Catalyst	TOF (h^{-1})	Rate (mL min^{-1} g_{cat}^{-1})	Yield (%)	Temp (^0C)	Ref
$Co_{0.3}Au_{0.35}Pd_{0.35}/C$	80[a]	n.r.	90	25	[178]
CoPd@PdC	n.r.	545	100	25	[179]
Pd/C[b]	1578	n.r.	92	80	[180]
$Ag_{0.1}Pd_{0.9}$/RGO	2739	n.r.	100	50	[181]
Pd/H-BETA	59.2	0.75	1.3	50	[182]
Ag_1Pd_4/N-ZIF	936[a]	213[a]	100	80	[183]
$Ag_{18}Pd_{82}$/ZIF	580	n.r.	100	80	[184]
8% Pd/g-C_3N_4	50	129	n.r.	15	[185]
8% Pd/g-C_3N_4 + hν	71	250	n.r.	15	[185]
Pd-MnO_x/H_2N-SiO_2	1300[a]	40[a]	100	50	[186]

[a] Initial TOF or rate, [b] uses HCO_2NH_4

The Jiang and Yan groups produced a series of mixed CoAuPd catalyst on carbon for room temperature FA dehydrogenation.[178] The catalysts were produced by coreduction of the corresponding salts with $NaBH_4$ in the presense of carbon black. The most effective catalyst was $Co_{0.3}Au_{0.35}Pd_{0.35}/C$, which was capable of an initial TOF of 80 h^{-1} with respect to CoAuPd, with 90% conversion of formic acid (TON = 45).

The Wang group developed a catalyst consisting of PdCo on a Pd/C scaffold.[179] At its peak, the recyclable catalyst was capable of producing an initial production rate of 545 mL H_2 min^{-1} g_{cat}^{-1} at room temperature. Quantitative dehydrogenation of formate is complete after 90 minutes. The catalyst appears to retain its full activity after 4 cycles.

The Lin group demonstrated the reversible dehydrogenation of formate salts into H_2 and CO_3^{2-}, and the reverse reaction using platinum group nanoparticles on activated carbon.[180] The most active catalyst, Pd/C at 80 ^0C was capable of 1578 turnovers, with respect to Pd nanoparticles on

the surface of the carbon support, in one hour for an 85.6% yield (H_2 generation halted after 1.5 hours and 92.1% yield). The group used ammonium formate due to the improved solubility of ammonium formate vs. the sodium salt at ambient and elevated temperatures. By increasing the pressure of H_2 (to ~20 atm), the same catalyst was capable of reducing carbonate in solution to formate at a 96% yield after 15 hours (similar results at 50 atm in 2 hours).

The Xu group has developed highly dispersed AgPd nanoparticles on graphene.[181] The group prepared their highly dispersed catalyst by co-precipitating with cobalt-borate to prevent clumping of the active AgPd catalyst (Figure 1.6.3.2). Before catalysis, the borate particles were etched off of the surface with acid. The resulting catalyst was capable of an average TOF of 2739 h^{-1} at 50 ^{0}C, with a remarkable quantitative dehydrogenation of formic acid in less than two minutes (2 mol% catalyst with respect to Ag/Pd). The catalyst is also active at room temperature, capable of TOF of 453 h^{-1}, and complete conversion after 10 minutes. The activity of the catalyst increased as a higher percentage of Co-Bi to Ag/Pd was precipitated until a 6:1 ratio of Co:Ag/Pd. The catalyst was stable without a loss of activity over 5 cycles.

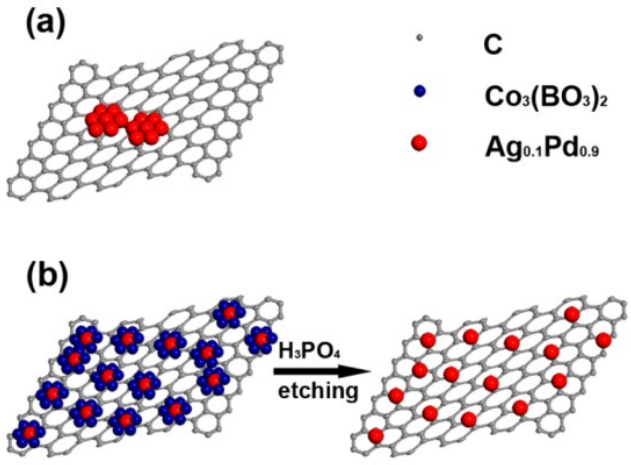

Figure 1.6.3.2. Effect of co-deposition of $Co_3(BO_3)_2$ with AgPd nanocrystals on graphene to prevent aggregation of AgPd particles. Reproduced from ref. 181.

The Yamashita group investigated, for the first time, the impregnation of zeolite supports with metallic nanoparticles for the use of formic acid dehydrogenation.[182] The group achieved their best results by impregnating Pd nanoparticles within H-BETA zeolites, and were able to achieve a rate of 0.75 mL min^{-1} g_{cat}^{-1} over the first hour. This corresponded to a TOF of 59.2 h^{-1}, with respect to the active Pd nanoparticle. Unfortunately, the catalyst was only active for ~ 3 hours, deactivating after achieving a 1.3% yield, with respect to formic acid.

At the same time as the Yamashita group was studying Pd nanoparticles in zeolites, the Gao and Wang groups developed a series of N-doped zeolitic imidiazole frameworks doped with both Pd and Ag nanoparticles for formate dehydrogenation.[183] The heterogeneous catalyst with a 4:1 Pd:Ag ratio was capable of exhibiting initial TOFs of 936 h^{-1} at 80 ^{0}C (579 h^{-1} at 60 ^{0}C), with respect to the active nanoparticles. Interestingly, the catalyst with only Ag was inactive, while the catalyst with only Pd had a 50% decrease in activity over the first 10 minutes. Within 5 minutes, the Pd_4Ag_1ZIF catalyst was able to get 100% dehydrogenation at an excellent rate of 213 mL min^{-1} g_{cat}^{-1}.

The Luo group also tested the use of AgPd nanocatalysts on ZIF frameworks. The catalyst was loaded by wet impregnation, followed by reduction with $NaBH_4$.[184] The best catalyst ($Ag_{18}Pd_{82}$ on ZIF-8) was capable of achieving was capable of achieving a TOF of 580 h^{-1} (with respect to AgPd) with quantitative yields at 80 ^{0}C. The catalyst was also mostly recyclable, with a slight reduction of activity after each cycle, although the catalyst was still capable of quantitative conversions. The catalyst may have produced a trace amount of CO, although the production was too low to confirm.

The Li and Chen groups used graphitic C_3N_4 (g-C_3N_4) as a photosemiconductor loaded with Pd as a photocatalyst for hydrogen evolution, while formic acid acts a hole scavenger and is

oxidized.[185] The loaded catalyst was produced by wet impregnation of Pd^{2+} followed by reduction with $NaBH_4$. While the catalyst was active in the absence of light (TOF = 50 h^{-1}, ~130 mL min^{-1} g_{cat}^{-1}), activity was increased when illuminated with visible light (TOF= 71 $h^{-1,}$ ~250 mL min^{-1} g_{cat}^{-1}). Unfortunately, even in the presence of visible light, the H_2 yield after 4 hours is ~50%.

The Kaya group prepared a Pd-MnO_x catalyst supported on amine functionalized SiO_2 as a rapid catalyst for HCOOH dehydrogenation.[186] The catalyst was capable of a high TOF of 1300 h^{-1}, with respect to Pd on the surface. The catalyst was capable of achieving quantitative yields of H_2/CO_2 in less than 10 minutes, although this was achieved with a relatively high 1.5 mol% catalyst loading. The catalyst was active after recovery, but the activity was diminished over 4 catalytic runs, where conversion took 30 minutes. The group did not report activity after further recovery cycles, although it is likely that the catalyst will slowly decompose.

1.6.4 Outlook

The scope of hydrogen production from formic acid via homogeneous catalysts is promising. Many catalysts are produced from either commercially available or simple ligands, and capable of high TOFs and repeated for many cycles. High TONs of >100,000 were reported, and are likely capable of being topped in long term flow reactions with the catalysts described above.

The scope of transition metal catalysts used in homogeneous catalysts are limited to Ru and Ir. While the Beller group has made great strides in incorporating earth abundant Fe catalysts into the field, further efforts to convert hydrogen production catalysts should be realized.

Low-temperature heterogeneous catalysts are currently very limited in their scope, focusing on Pd and Pd alloys for dehydrogenation. However, a few of these catalysts are very promising,

providing stable TOFs in excess of 1000 h^{-1} and nearly complete recoveries. The large majority of these catalysts were developed in the past year, and the intriguing theoretical work from Mullins provides a crutch for future work.

Overall, the productivity of formic acid as a hydrogen storage molecule very high and promising. Unfortunately, the very low 4.4 wt% of hydrogen severely limits the feasibility for formic acid, especially for mobile storage. It remains to be seen if formic acid storage can become successfully commercialized, although the activity of dehydrogenation catalysts, both homogeneous and heterogeneous, are far greater than their methanol or formaldehyde counterparts.

1.7 Scope of Thesis

Despite decades of effort into this field, activity and stability of photocatalytic water splitting catalysts remain too low for commercialization. Furthermore, the low reaction rates of pure water splitting result in a storage problem for produced hydrogen. Rapid, on demand, production of hydrogen for direct fuel cell applications is unlikely to be produced by pure photocatalytic water splitting. Storing hydrogen long term provides several issues including pressurization, and with pure water splitting, separation of O_2 and H_2 from gas flow is difficult, expensive and energy intensive.

By merging the emerging fields of hydrogen storage with CO_2 photoreduction, we can provide a novel method for solar powered hydrogen production from light, using small organic molecules as shuttles and storage molecules. The scope of this thesis is to explore the feasibility of using LOHC shuttles.

In one section, we will explore the photoreduction of CO_2 using a promising photosemiconductor, $BiVO_4$. In the second half, we will explore the selective dehydrogenation of formaldehyde using a cheap and abundant photocatalyst, $Na_4Fe(CN)_6$.

1.8 References

(1) Young, K. J.; Martini, L. a.; Milot, R. L.; Snoeberger, R. C.; Batista, V. S.; Schmuttenmaer, C. a.; Crabtree, R. H.; Brudvig, G. W. *Coord. Chem. Rev.* **2012**, *256*, 2503.

(2) Maeda, K.; Domen, K. *J. Phys. Chem. Lett.* **2010**, *1*, 2655.

(3) Abe, R. *J. Photochem. Photobiol. C Photochem. Rev.* **2010**, *11*, 179.

(4) Hisatomi, T.; Kubota, J.; Domen, K. *Chem. Soc. Rev.* **2014**, *43*, 7520.

(5) Maeda, K. *ACS Catal.* **2013**, *2*, 1486.

(6) Chen, X.; Shen, S.; Guo, L.; Mao, S. S. *Chem. Rev.* **2010**, *110*, 6503.

(7) Eberle, U.; Felderhoff, M.; Schüth, F. *Angew. Chem. Int. Ed. Engl.* **2009**, *48*, 6608.

(8) Habisreutinger, S. N.; Schmidt-Mende, L.; Stolarczyk, J. K. *Angew. Chem. Int. Ed. Engl.* **2013**, *52*, 7372.

(9) Grasemann, M.; Laurenczy, G. *Energy Environ. Sci.* **2012**, *5*, 8171.

(10) Yong, X.; Schoonen, M. a a. *Am. Mineral.* **2000**, *85*, 543.

(11) Fujishima, A.; Honda, K. *Nature* **1972**, *238*, 37.

(12) Linic, S.; Christopher, P.; Ingram, D. B. *Nat. Mater.* **2011**, *10*, 911.

(13) Rycenga, M.; Cobley, C. M.; Zeng, J.; Li, W.; Moran, C. H.; Zhang, Q.; Qin, D.; Xia, Y. *Chem. Rev.* **2011**, *111*, 3669.

(14) Hou, W.; Cronin, S. B. *Adv. Funct. Mater.* **2013**, *23*, 1612.

(15) Ingram, D. B.; Linic, S. **2011**, 5202.

(16) O'Regan, B.; Grätzel, M. *Nature* **1991**, *353*, 737.

(17) Palomares, E.; Clifford, J. N.; Haque, S. a; Lutz, T.; Durrant, J. R. *J. Am. Chem. Soc.* **2003**, *125*, 475.

(18) Paracchino, A.; Mathews, N.; Hisatomi, T.; Stefik, M.; Tilley, S. D.; Grätzel, M. *Energy Environ. Sci.* **2012**, *5*, 8673.

(19) Nakade, S.; Kanzaki, T.; Kubo, W.; Kitamura, T.; Wada, Y.; Yanagida, S. *J. Phys. Chem. B* **2005**, *109*, 3480.

(20) Ozawa, H.; Okuyama, Y.; Arakawa, H. *ChemPhysChem* **2014**, *15*, 1201.

(21) Wiberg, J.; Marinado, T.; Hagberg, D. P.; Sun, L.; Hagfeldt, A.; Albinsson, B. *J. Phys. Chem. C* **2009**, *113*, 3881.

(22) Abrahamsson, M.; Johansson, P. G.; Ardo, S.; Kopecky, A.; Galoppini, E.; Meyer, G. J. *J. Phys. Chem. Lett.* **2010**, *1*, 1725.

(23) Hua, Y.; He, J.; Zhang, C.; Qin, C.; Han, L.; Zhao, J.; Chen, T.; Wong, W.-Y.; Wong, W.-K.; Zhu, X. *J. Mater. Chem. A* **2015**, *3*, 3103.

(24) Yoshida, M.; Yamakata, A.; Takanabe, K.; Kubota, J.; Osawa, M.; Domen, K. *J. Am. Chem. Soc.* **2009**, *131*, 13218.

(25) Kato, H.; Asakura, K.; Kudo, A. *J. Am. Chem. Soc.* **2003**, *125*, 3082.

(26) Bourgeteau, T.; Tondelier, D.; Geffroy, B.; Brisse, R.; Laberty-Robert, C.; Campidelli, S.; de Bettignies, R.; Artero, V.; Palacin, S.; Jousselme, B. *Energy. Sustain. Soc.* **2013**, *6*, 2706.

(27) Maeda, K.; Lu, D.; Domen, K. *Chem. - A Eur. J.* **2013**, *19*, 4986.

(28) Harriman, A.; Pickering, I. J.; Thomas, J. M.; Christensen, P. a. *J. Chem. Soc. Faraday Trans. 1* **1988**, *84*, 2795.

(29) Kanan, M. W.; Nocera, D. G. *Science* **2008**, *321*, 1072.

(30) Zhang, J.; Wang, X. *Angew. Chemie Int. Ed.* **2015**, *54*, 7230.

(31) Lo, C. C.; Huang, C. W.; Liao, C. H.; Wu, J. C. S. *Int. J. Hydrogen Energy* **2010**, *35*, 1523.

(32) Yu, S.-C.; Huang, C.-W.; Liao, C.-H.; Wu, J. C. S.; Chang, S.-T.; Chen, K.-H. *J. Memb. Sci.* **2011**, *382*, 291.

(33) Sayama, K.; Mukasa, K.; Abe, R.; Abe, Y.; Arakawa, H. *Chem. Commun. (Camb).* **2001**, 2416.

(34) Sayama, K.; Mukasa, K.; Abe, R.; Abe, Y.; Arakawa, H. *J. Photochem. Photobiol. A Chem.* **2002**, *148*, 71.

(35) Kato, H.; Hori, M.; Konta, R.; Shimodaira, Y.; Kudo, A. *Chem Lett,* **2004**, *33*, 1348–1349.

(36) Abe, R.; Takata, T.; Sugihara, H.; Domen, K. *Chem. Commun. (Camb).* **2005**, 3829.

(37) Abe, R.; Sayama, K.; Sugihara, H. *J. Phys. Chem. B* **2005**, *109*, 16052.

(38) Sasaki, Y.; Iwase, A.; Kato, H.; Kudo, A. *J. Catal.* **2008**, *259*, 133.

(39) Higashi, M.; Abe, R.; Ishikawa, A.; Takata, T.; Ohtani, B.; Domen, K. *Chem. Lett.* **2008**, *37*, 138.

(40) Higashi, M.; Abe, R.; Teramura, K.; Takata, T.; Ohtani, B.; Domen, K. *Chem. Phys. Lett.* **2008**, *452*, 120.

(41) Higashi, M.; Abe, R.; Takata, T.; Domen, K. *Chem. Mat.* **2009**, *21*, 1543.

(42) Bae, S. W.; Ji, S. M.; Hong, S. J.; Jang, J. W.; Lee, J. S. *Int. J. Hydrogen Energy* **2009**, *34*, 3243.

(43) Maeda, K.; Higashi, M.; Lu, D.; Abe, R.; Domen, K. *J. Am. Chem. Soc.* **2010**, *132*, 5858.

(44) Maeda, K.; Abe, R.; Domen, K. *J. Phys. Chem. C* **2011**, *115*, 3057.

(45) Abe, R.; Higashi, M.; Domen, K. *ChemSusChem* **2011**, *4*, 228.

(46) Park, H. S.; Lee, H. C.; Leonard, K. C.; Liu, G.; Bard, A. J. *ChemPhysChem* **2013**, *14*, 2277.

(47) Maeda, K.; Lu, D.; Domen, K. *ACS Catal.* **2013**, *3*, 1026.

(48) Abe, R.; Shinmei, K.; Koumura, N.; Hara, K.; Ohtani, B. *J. Am. Chem. Soc.* **2013**, *135*, 16872.

(49) Miseki, Y.; Fujiyoshi, S.; Gunji, T.; Sayama, K. *Catal. Sci. Technol.* **2013**, *3*, 1750.

(50) Sasaki, Y.; Kato, H.; Kudo, A. *J. Am. Chem. Soc.* **2013**.

(51) Kato, H.; Sasaki, Y.; Shirakura, N.; Kudo, A. *J. Mater. Chem. A* **2013**, *1*, 12327.

(52) Niishiro, R.; Tanaka, S.; Kudo, A. *Appl. Catal. B Environ.* **2014**, *150-151*, 187.

(53) Maeda, K. *ACS Appl. Mater. Interfaces* **2014**, *6*, 2167.

(54) Martin, D. J.; Reardon, P. J. T.; Moniz, S. J. a; Tang, J. *J. Am. Chem. Soc.* **2014**, 2.

(55) Wang, W.; Chen, J.; Li, C.; Tian, W. *Nat. Commun.* **2014**, *5*, 1.

(56) Ma, S. S. K.; Maeda, K.; Domen, K. *Catal. Sci. Technol.* **2012**, *2*, 818.

(57) Maeda, K. *Phys. Chem. Chem. Phys.* **2013**, *15*, 10537.

(58) Tabata, M.; Maeda, K.; Higashi, M.; Lu, D.; Takata, T.; Abe, R.; Domen, K. *Langmuir* **2010**, *26*, 9161.

(59) Suzuki, H.; Tomita, O.; Higashi, M.; Abe, R. *Catal. Sci. Technol.* **2015**, *5*, 2640.

(60) Sasaki, Y.; Nemoto, H.; Saito, K.; Kudo, A. *J. Phys. Chem. C* **2009**, *113*, 17536.

(61) Ma, S. S. K.; Maeda, K.; Hisatomi, T.; Tabata, M.; Kudo, A.; Domen, K. *Chem. - A Eur. J.* **2013**, *19*, 7480.

(62) Iwase, A.; Ng, Y. H.; Ishiguro, Y.; Kudo, A.; Amal, R. *J. Am. Chem. Soc.* **2011**, *133*, 11054.

(63) Kobayashi, R.; Tanigawa, S.; Takashima, T.; Ohtani, B.; Irie, H. *J. Phys. Chem. C* **2014**, *118*, 22450.

(64) Iwashina, K.; Iwase, A.; Ng, Y. H.; Amal, R.; Kudo, A. *J. Am. Chem. Soc.* **2015**, *137*, 604.

(65) Tian, Y.; Tatsuma, T. *J. Am. Chem. Soc.* **2005**, *127*, 7632.

(66) Tada, H.; Mitsui, T.; Kiyonaga, T.; Akita, T.; Tanaka, K. *Nat. Mater.* **2006**, *5*, 782.

(67) Ye, L.; Liu, J.; Gong, C.; Tian, L.; Peng, T.; Zan, L. *ACS Catal.* **2012**, *2*, 1677.

(68) Yu, Z. B.; Xie, Y. P.; Liu, G.; Lu, G. Q. (Max); Ma, X. L.; Cheng, H.-M. *J. Mater. Chem. A* **2013**, *1*, 2773.

(69) Zhou, H.; Ding, L.; Fan, T.; Ding, J.; Zhang, D.; Guo, Q. *Appl. Catal. B Environ.* **2014**, *147*, 221.

(70) Barton, E. E.; Rampulla, D. M.; Bocarsly, A. B. *J. Am. Chem. Soc.* **2008**, *130*, 6342.

(71) Sato, S.; Arai, T.; Morikawa, T.; Uemura, K.; Suzuki, T. M.; Tanaka, H.; Kajino, T. *J. Am. Chem. Soc.* **2011**, *133*, 15240.

(72) Niu, P.; Yang, Y.; Yu, J. C.; Liu, G.; Cheng, H.-M. *Chem. Commun.* **2014**, *50*, 10837.

(73) Bai, S.; Wang, X.; Hu, C.; Xie, M.; Jiang, J.; Xiong, Y. *Chem. Commun. (Camb).* **2014**, *50*, 6094.

(74) He, H.; Zapol, P.; Curtiss, L. a. *Energy Environ. Sci.* **2012**, *5*, 6196.

(75) Gattrell, M.; Gupta, N.; Co, a. *J. Electroanal. Chem.* **2006**, *594*, 1.

(76) Chiarello, G. L.; Aguirre, M. H.; Selli, E. *J. Catal.* **2010**, *273*, 182.

(77) Suzuki, T. M.; Tanaka, H.; Morikawa, T.; Iwaki, M.; Sato, S.; Saeki, S.; Inoue, M.; Kajino, T.; Motohiro, T. *Chem. Commun. (Camb).* **2011**, *47*, 8673.

(78) Sahu, S.; Liu, Y.; Wang, P.; Bunker, C. E.; Fernando, K. a S.; Lewis, W. K.; Guliants, E. a.; Yang, F.; Wang, J.; Sun, Y. P. *Langmuir* **2014**, *30*, 8631.

(79) Nishijima, Y.; Ueno, K.; Kotake, Y.; Murakoshi, K.; Inoue, H.; Misawa, H. *J. Phys. Chem. Lett.* **2012**, *3*, 1248.

(80) Anpo, M.; Yamashita, H.; Ikeue, K.; Fujii, Y.; Zhang, S. G.; Ichihashi, Y.; Park, D. R.; Suzuki, Y.; Koyano, K.; Tatsumi, T. *Catal. Today* **1998**, *44*, 327.

(81) Shkrob, I. a.; Marin, T. W.; He, H.; Zapol, P. *J. Phys. Chem. C* **2012**, *116*, 9450.

(82) Srinivas, B.; Shubhamangala, B.; Lalitha, K.; Anil Kumar Reddy, P.; Durga Kumari, V.; Subrahmanyam, M.; De, B. R. *Photochem. Photobiol.* **2011**, *87*, 995.

(83) Ola, O.; Mercedes Maroto-Valer, M. *J. Catal.* **2014**, *309*, 300.

(84) Rossetti, I.; Villa, a.; Pirola, C.; Prati, L.; Ramis, G. *RSC Adv.* **2014**, *4*, 28883.

(85) Liu, Y.; Huang, B.; Dai, Y.; Zhang, X.; Qin, X.; Jiang, M.; Whangbo, M. H. *Catal. Commun.* **2009**, *11*, 210.

(86) Fang, Z.; Li, S.; Gong, Y.; Liao, W.; Tian, S.; Shan, C.; He, C. *J. Saudi Chem. Soc.* **2014**, *18*, 299.

(87) Inoue, T.; Fujishima, A.; Konishi, S.; Honda, K. *Nature* **1979**, *227*, 637.

(88) Nguyen, T. V.; Wu, J. C. S.; Chiou, C. H. *Catal. Commun.* **2008**, *9*, 2073.

(89) Nguyen, T. V.; Wu, J. C. S. *Sol. Energy Mater. Sol. Cells* **2008**, *92*, 864.

(90) Marcì, G.; García-López, E. I.; Palmisano, L. *Catal. Commun.* **2014**, *53*, 38.

(91) Ong, W.-J.; Gui, M. M.; Chai, S.-P.; Mohamed, A. R. *RSC Adv.* **2013**, *3*, 4505.

(92) Hou, W.; Hung, W. H.; Pavaskar, P.; Goeppert, A.; Aykol, M.; Cronin, S. B. *ACS Catal.* **2011**, *1*, 929.

(93) Neaţu, Ş.; Maciá-Agulló, J. A.; Concepción, P.; Garcia, H. *J. Am. Chem. Soc.* **2014**, *136*, 15969.

(94) Zhou, Y.; Tian, Z.; Zhao, Z.; Liu, Q.; Kou, J.; Chen, X.; Gao, J.; Yan, S.; Zou, Z. *ACS Appl. Mater. Interfaces* **2011**, *3*, 3594.

(95) Liu, Q.; Zhou, Y.; Tian, Z.; Chen, X.; Gao, J.; Zou, Z. *J. Mater. Chem.* **2012**, *22*, 2033.

(96) Zhang, N.; Ouyang, S.; Kako, T.; Ye, J. *Chem. Commun.* **2012**, *48*, 1269.

(97) Yu, J.; Jin, J.; Cheng, B.; Jaroniec, M. *J. Mater. Chem. A* **2014**, *2*, 3407.

(98) Ong, W.-J.; Tan, L.-L.; Chai, S.-P.; Yong, S.-T. *Chem. Commun.* **2015**, *51*, 858.

(99) Ong, W.-J.; Tan, L.-L.; Chai, S.-P.; Yong, S.-T. *Dalt. Trans.* **2015**, *44*, 1249.

(100) Neaţu, Ş.; Maciá-Agulló, J. A.; Garcia, H. *Int. J. Mol. Sci.* **2014**, *15*, 5246.

(101) Pan, P.-W.; Chen, Y.-W. *Catal. Commun.* **2007**, *8*, 1546.

(102) Wang, Z. Y.; Chou, H. C.; Wu, J. C. S.; Ping Tsai, D.; Mul, G.; Engineering, C. *Appl. Catal. A Gen.* **2010**, *380*, 172.

(103) Tsai, C.; Chen, H. M.; Liu, R.; Asakura, K.; Chan, T. *J. Phys. Chem. C* **2011**, *115*, 10180.

(104) Lee, D.-S.; Chen, H.-J.; Chen, Y.-W. *J. Phys. Chem. Solids* **2012**, *73*, 661.

(105) Li, X.; Chen, J.; Li, H.; Li, J.; Xu, Y.; Liu, Y.; Zhou, J. *J. Nat. Gas Chem.* **2011**, *20*, 413.

(106) Liu, J.-Y.; Garg, B.; Ling, Y.-C. *Green Chem.* **2011**, *13*, 2029.

(107) Xie, Y. P.; Liu, G.; Yin, L.; Cheng, H.-M. *J. Mater. Chem.* **2012**, *22*, 6746.

(108) Mao, J.; Peng, T.; Zhang, X.; Li, K.; Zan, L. *Catal. Commun.* **2012**, *28*, 38.

(109) Arai, T.; Sato, S.; Uemura, K.; Morikawa, T.; Kajino, T.; Motohiro, T. *Chem. Commun. (Camb).* **2010**, *46*, 6944.

(110) Arai, T.; Tajima, S.; Sato, S.; Uemura, K.; Morikawa, T.; Kajino, T. *Chem. Commun.* **2011**, *47*, 12664.

(111) Chen, Q.; Zhou, M.; Ma, D.; Jing, D. *J. Nanomater.* **2012**, *2012*.

(112) Reece, S. Y.; Hamel, J. a; Sung, K.; Jarvi, T. D.; Esswein, A. J.; Pijpers, J. J. H.; Nocera, D. G. *Science* **2011**, *334*, 645.

(113) Rongé, J.; Bosserez, T.; Martel, D.; Nervi, C.; Boarino, L.; Taulelle, F.; Decher, G.; Bordiga, S.; Martens, J. a. *Chem. Soc. Rev.* **2014**, *43*.

(114) Jeon, H. S.; Koh, J. H.; Park, S. J.; Jee, M. S.; Ko, D.-H.; Hwang, Y. J.; Min, B. K. *J. Mater. Chem. A* **2014**, *3*, 5835.

(115) Makowski, P.; Thomas, A.; Kuhn, P.; Goettmann, F. *Energy Environ. Sci.* **2009**, *2*, 480.

(116) Alberico, E.; Nielsen, M. *Chem. Commun.* **2015**, *51*, 6714.

(117) Palo, D. R.; Dagle, R. a; Holladay, J. D. **2007**, 3992.

(118) Yamamoto, H.; Shinoda, S.; Saito, Y. *J. Mol. Catal.* **1985**, *30*, 259.

(119) Shinoda, S.; Itagaki, H.; Saito, Y. *J. Chem. Soc. Chem. Commun.* **1985**, *8*, 860.

(120) Itagaki, H.; Shinoda, S.; Saito, Y. *Bulletin of the Chemical Society of Japan*, **1988**, *61*, 2291.

(121) Smith, T. a.; Aplin, R. P.; Maitlis, P. M. *J. Organomet. Chem.* **1985**, *291*, c13.

(122) Morton, D.; Cole-Hamilton, D. J. *J. Chem. Soc. Chem. Commun.* **1988**, *2*, 1154.

(123) Yamakawa, T.; Hiroi, M.; Shinoda, S. *J. Chem. Soc. Dalt. Trans.* **1994**, 2265.

(124) Einaga, H.; Yamakawa, T.; Shinoda, S. *J. Coord. Chem.* **1994**, *32*, 117.

(125) Delgado-Lieta, E.; Luke, M. A.; Jones, R. F.; Cole-Hamilton, D. J. ***Polyhedron***, 1982, *1*, 836.

(126) Bertoli, M.; Choualeb, A.; Lough, A. J.; Moore, B.; Spasyuk, D.; Gusev, D. G. *Organometallics* **2011**, *30*, 3479.

(127) Nielsen, M.; Kammer, A.; Cozzula, D.; Junge, H.; Gladiali, S.; Beller, M. *Angew. Chemie - Int. Ed.* **2011**, *50*, 9593.

(128) Kowalska, E.; Rau, S.; Ohtani, B. *J. Nanotechnol.* **2012**, *2012*.

(129) Rodriguez, J.; Thivel, P. X.; Puzenat, E. *Int. J. Hydrogen Energy* **2013**, *38*, 6344.

(130) Lalitha, K.; Reddy, J. K.; Phanikrishna Sharma, M. V.; Kumari, V. D.; Subrahmanyam, M. *Int. J. Hydrogen Energy* **2010**, *35*, 3991.

(131) Kim, J.; Kang, M. *Int. J. Hydrogen Energy* **2012**, *37*, 8249.

(132) Sabio, E. M.; Chamousis, R. L.; Browning, N. D.; Osterloh, F. E. *J. Phys. Chem. C* **2012**, *116*, 3161.

(133) Jana, P.; Mata Montero, C.; Pizarro, P.; Coronado, J. M.; Serrano, D. P.; De La Peña O'Shea, V. a. *Int. J. Hydrogen Energy* **2014**, *39*, 5283.

(134) Nielsen, M.; Alberico, E.; Baumann, W.; Drexler, H.-J.; Junge, H.; Gladiali, S.; Beller, M. *Nature* **2013**, *495*, 85.

(135) Alberico, E.; Sponholz, P.; Cordes, C.; Nielsen, M.; Drexler, H. J.; Baumann, W.; Junge, H.; Beller, M. *Angew. Chemie - Int. Ed.* **2013**, *52*, 14162.

(136) Rodríguez-Lugo, R. E.; Trincado, M.; Vogt, M.; Tewes, F.; Santiso-Quinones, G.; Grützmacher, H. *Nat. Chem.* **2013**, *5*, 342.

(137) Hu, P.; Diskin-Posner, Y.; Ben-David, Y.; Milstein, D. *ACS Catal.* **2014**, *4*, 2649.

(138) Monney, A.; Barsch, E.; Sponholz, P.; Junge, H.; Ludwig, R.; Beller, M. *Chem. Commun. (Camb).* **2014**, *50*, 707.

(139) Campos, J.; Sharninghausen, L. S.; Manas, M. G.; Crabtree, R. H. *Inorg. Chem.* **2015**, *54*, 5079.

(140) Heim, L. E.; Schlörer, N. E.; Choi, J.-H.; Prechtl, M. H. G. *Nat. Commun.* **2014**, *5*, 3621.

(141) Loew, O. *Ber der Deutchen Chem. Geselschaft* **1887**, *20*, 144.

(142) Ashby, E. C.; Doctorovich, F.; Liotta, C. L.; Neumann, H. M.; Barefield, E. K.; Konda, A.; Zhang, K.; Hurley, J.; Siemer, D. D. *J. Am. Chem. Soc.* **1993**, *115*, 1171.

(143) Kapoor, S.; Naumov, S. *Chem. Phys. Lett.* **2004**, *387*, 322.

(144) Bi, Y.; Lu, G. *Int. J. Hydrogen Energy* **2008**, *33*, 2225.

(145) Bi, Y.; Hu, H.; Li, Q.; Lu, G. *Int. J. Hydrogen Energy* **2010**, *35*, 7177.

(146) Hu, H.; Jiao, Z.; Ye, J.; Lu, G.; Bi, Y. *Nano Energy* **2014**, *8*, 103.

(147) Li, Y.; Chen, T.; Wang, T.; Zhang, Y.; Lu, G.; Bi, Y. *Int. J. Hydrogen Energy* **2014**, *39*, 9114.

(148) Pan, X.; Wang, L.; Ling, F.; Li, Y.; Han, D.; Pang, Q.; Jia, L. *Int. J. Hydrogen Energy* **2015**, *40*, 1752.

(149) Chowdhury, P.; Malekshoar, G.; Ray, M. B.; Zhu, J.; Ray, A. K. *Ind. Eng. Chem. Res.* **2013**, *52*, 5023.

(150) Wang, L.; Pang, Q.; Song, Q.; Pan, X.; Jia, L. *Fuel* **2015**, *140*, 267.

(151) Gao, H.; Zhang, J.; Wang, R.; Wang, M. *Appl. Catal. B Environ.* **2015**, *172-173*, 1.

(152) Suenobu, T.; Isaka, Y.; Shibata, S.; Fukuzumi, S. *Chem. Commun.* **2015**, *51*, 1670.

(153) Boddien, A.; Federsel, C.; Sponholz, P.; Mellmann, D.; Jackstell, R.; Junge, H.; Laurenczy, G.; Beller, M. *Energy Environ. Sci.* **2012**, *5*, 8907.

(154) Hull, J. F.; Himeda, Y.; Wang, W.-H.; Hashiguchi, B.; Periana, R.; Szalda, D. J.; Muckerman, J. T.; Fujita, E. *Nat. Chem.* **2012**, *4*, 383.

(155) Keller, S. G.; Ringenberg, M. R.; Häussinger, D.; Ward, T. R. *Eur. J. Inorg. Chem.* **2014**, *2014*, 5860.

(156) Kothandaraman, J.; Czaun, M.; Goeppert, A.; Haiges, R.; Jones, J.-P.; May, R. B.; Prakash, G. K. S.; Olah, G. A. *ChemSusChem* **2015**, *8*, 1442.

(157) Gao, Y.; Kuncheria, J. K.; Jenkins, H. a.; Puddephatt, R. J.; Yap, G. P. a. *J. Chem. Soc. Dalt. Trans.* **2000**, *2*, 3212.

(158) Enthaler, S.; von Langermann, J.; Schmidt, T. *Energy Environ. Sci.* **2010**, *3*, 1207.

(159) Yoshida, T.; Ueda, Y.; Otsuka, S. *J. Am. Chem. Soc.* **1978**, *100*, 3941.

(160) Loges, B.; Boddien, A.; Junge, H.; Beller, M. *Angew. Chemie - Int. Ed.* **2008**, *47*, 3962.

(161) Fellay, C.; Dyson, P. J.; Laurenczy, G. *Angew. Chemie - Int. Ed.* **2008**, *47*, 3966.

(162) Coffey, R. S. *Chem. Commun.* **1967**, 923b.

(163) Strauss, S. H.; Whitmire, K. H.; Shriver, D. F. *J. Organomet. Chem.* **1979**, *174*, C59.

(164) Himeda, Y.; Onozawa-Komatsuzaki, N.; Sugihara, H.; Arakawa, H.; Kasuga, K. *Organometallics* **2004**, *23*, 1480.

(165) Boddien, A.; Loges, B.; Junge, H.; Beller, M. *ChemSusChem* **2008**, *1*, 751.

(166) Boddien, A.; Loges, B.; Junge, H.; Gärtner, F.; Noyes, J. R.; Beller, M. *Adv. Synth. Catal.* **2009**, *351*, 2517.

(167) Gan, W.; Snelders, D. J. M.; Dyson, P. J.; Laurenczy, G. *ChemCatChem* **2013**, *5*, 1126.

(168) Fellay, C.; Yan, N.; Dyson, P. J.; Laurenczy, G. *Chem. - A Eur. J.* **2009**, *15*, 3752.

(169) Thevenon, A.; Frost-Pennington, E.; Weijia, G.; Dalebrook, A. F.; Laurenczy, G. *ChemCatChem* **2014**, *6*, 3146.

(170) Himeda, Y. *Green Chem.* **2009**, *11*, 2018.

(171) Wang, W.-H.; Xu, S.; Manaka, Y.; Suna, Y.; Kambayashi, H.; Muckerman, J. T.; Fujita, E.; Himeda, Y. *ChemSusChem* **2014**, *7*, 1976.

(172) Oldenhof, S.; De Bruin, B.; Lutz, M.; Siegler, M. a.; Patureau, F. W.; Van Der Vlugt, J. I.; Reek, J. N. H. *Chem. - A Eur. J.* **2013**, *19*, 11507.

(173) Himeda, Y.; Miyazawa, S.; Hirose, T. *ChemSusChem* **2011**, *4*, 487.

(174) Oldenhof, S.; Lutz, M.; de Bruin, B.; van der Vlugt, J. I.; Reek, J. N. H. *Chem. Sci.* **2014**, *6*, 1027.

(175) Boddien, A.; Mellmann, D.; Gärtner, F.; Jackstell, R.; Junge, H.; Dyson, P. J.; Laurenczy, G.; Ludwig, R.; Beller, M. *Science* **2011**, *333*, 1733.

(176) Mellmann, D.; Barsch, E.; Bauer, M.; Grabow, K.; Boddien, A.; Kammer, A.; Sponholz, P.; Bentrup, U.; Jackstell, R.; Junge, H.; Laurenczy, G.; Ludwig, R.; Beller, M. *Chem. - A Eur. J.* **2014**, *20*, 13589.

(177) Yu, W. Y.; Mullen, G. M.; Flaherty, D. W.; Mullins, C. B. *J. Am. Chem. Soc.* **2014**, *136*, 11070.

(178) Wang, Z. L.; Yan, J. M.; Ping, Y.; Wang, H. L.; Zheng, W. T.; Jiang, Q. *Angew. Chemie - Int. Ed.* **2013**, *52*, 4406.

(179) Qin, Y.; Liu, Y.; Liang, F.; Wang, L. *ChemSusChem* **2015**, *8*, 260.

(180) Su, J.; Yang, L.; Lu, M.; Lin, H. *ChemSusChem* **2015**, *8*, 813.

(181) Chen, Y.; Zhu, Q.-L.; Tsumori, N.; Xu, Q. *J. Am. Chem. Soc.* **2015**, *137*, 106.

(182) Navlani-García, M.; Martis, M.; Lozano-Castelló, D.; Cazorla-Amorós, D.; Mori, K.; Yamashita, H. *Catal. Sci. Technol.* **2015**, *5*, 364.

(183) Feng, C.; Hao, Y.; Zhang, L.; Shang, N.; Gao, S.; Wang, Z.; Wang, C. *RSC Adv.* **2015**, *5*, 39878.

(184) Dai, H.; Xia, B.; Wen, L.; Du, C.; Su, J.; Luo, W.; Cheng, G. *Appl. Catal. B Environ.* **2015**, *165*, 57.

(185) Cai, Y.-Y.; Li, X.-H.; Zhang, Y.-N.; Wei, X.; Wang, K.-X.; Chen, J.-S. *Angew. Chem. Int. Ed. Engl.* **2013**, *52*, 11822.

(186) Bulut, A.; Yurderi, M.; Karatas, Y.; Zahmakiran, M.; Kivrak, H.; Gulcan, M.; Kaya, M. *Appl. Catal. B Environ.* **2015**, *164*, 324.

Chapter 2: Activity and decomposition of $BiVO_4$ as a reverse combustion photocatalyst

2.1 Introduction

The idea of using water as an electron source for organic products, and for CO_2 in particular, is fascinating and potentially ground breaking vis-à-vis the implications for using organic materials as hydrogen carriers. Honda *et al* were the first to demonstrate CO_2 photoreduction coupled with water oxidation using TiO_2 and UV light in 1979[1], and ever since, many groups have begun to study a wide spectrum of wide and narrow band gap semiconductors capable of both oxidizing water and reducing CO_2. Titanium dioxide is a well-studied catalyst, and has been modified to control size, conductivity and sensitivity to visible light[2–5]. Ideally, the production of small organic fuels, especially methanol and methane, will use catalysts that can efficiently absorb visible light, including, but not limited to, catalysts based on WO_3, CdS, TaON, and $BiVO_4$[6–12].

$BiVO_4$ has gained popularity as a water oxidation catalyst in hydrogen production and photodegradation of organic waste[13–16]. Monoclinic $BiVO_4$ has conduction and valence bands which are well suited for water oxidation coupled with CO_2 reduction and hydrogen evolution (Figure 2.1.1). Its usage is theoretically advantageous over common water oxidation catalysts including TiO_2, due to its narrow band gap of ~2.4 eV, which allows it to readily absorb visible light.

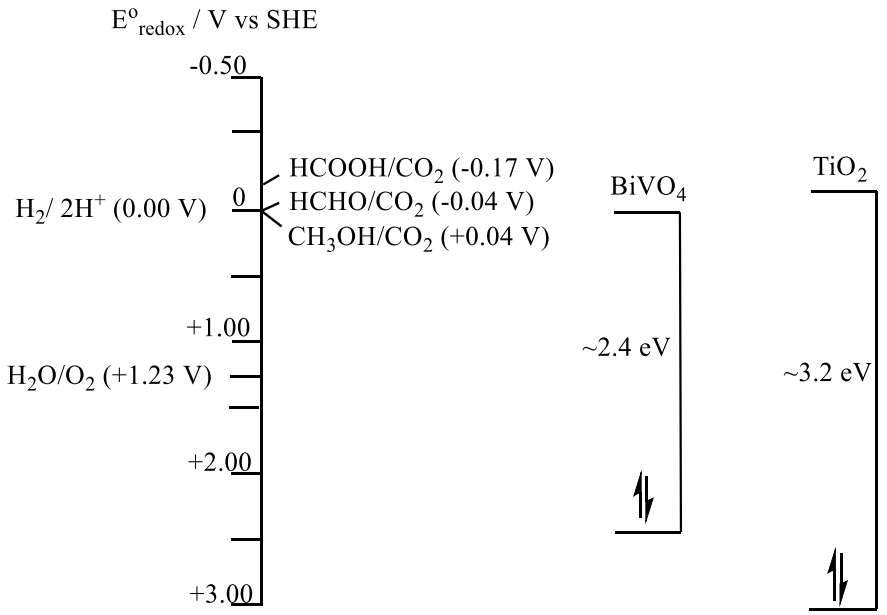

Figure 2.1.1. Band structure of monoclinic $BiVO_4$ and anatase TiO_2 demonstrating filled valence bands on the bottom (more positive) and empty conduction bands at the top (more negative).

$BiVO_4$ has also been demonstrated as a photosemiconductor in the reduction of CO_2 into methanol and ethanol[11,12]. The authors of these studies have claimed promising hydrocarbon yields, and the ability to recycle $BiVO_4$ although, the recovered $BiVO_4$ does not retain its full activity. Furthermore, the deactivation of $BiVO_4$ might possibly entail from decomposition triggered by the required reaction conditions. This important issue has not been sufficiently explored, if ignored at all. Herein, we report the cause and products of $BiVO_4$ deactivation during CO_2 reduction.

In addition, by studying the side products of $BiVO_4$ catalyzed photoreduction of CO_2, we can explore the possible pathways for CO_2 reduction, as described in section 1.3.1 (Figure 1.3.1.2). To the best of our knowledge, side products from CO_2 photoreduction over $BiVO_4$ are examined for the first time.

2.2 Experimental

Materials. Bismuth(III) nitrate ($Bi(NO_3)_3 \bullet 5H_2O$) and ammonium metavanadate (NH_4VO_3) were acquired from Strem Chemicals. Hexadecyltrimethylammonium bromide (CTAB), paraformaldehyde, formaldehyde, sodium formate, acetylacetone, deuterium oxide, and sodium deuteroxide were obtained from Sigma Aldrich. Sodium sulphate, sodium hydroxide, citric acid, acetic acid, isopropanol, and methanol were obtained from Fisher. Acetamide was purchased from Fluka. Formic acid was purchased from Acros Organics. Acetic anhydride was purchased from VWR. Ammonium acetate was purchased from Alfa Aesar. Chemicals were used without further purification. If not specifically mentioned, all reactions were carried out in distilled water without degassing or other modifications.

Characterization of Materials. Powder XRD diffractograms were obtained on a Rigaku Ultima IV diffractometer. UV-Vis spectra were obtained on a Specmate UV-1100 spectrometer. Scanning electron microscopy (SEM) and energy dispersive x-ray analysis (EDX) was performed with a JSM-7500F SEM instrument by JEOL, Inc.

NMR. ^{51}V NMR spectra were recorded on a Bruker Avance II 300 MHz spectrometer. Chemical shifts are reported in p.p.m. Spectra were recorded at 298 K.

GC Select Volatile Organic Chemical (VOC) detection and identification was carried out with an Agilent 7820A GC equipped with a flame ionization detector (FID), using a Restek Rt-U-Bond column with helium as the carrier gas. Gas detection and identification was carried out with an Agilent 7820A GC equipped with a thermal conductivity detector (TCD), using the Agilent Select Permanent Gases columns with argon as the carrier gas. Concentrations of were compared with prepared standard curves of the pure materials.

2.2.1 Synthesis of Semiconductors

Synthesis of *m*-$BiVO_4$ hyperbranched crystals: Monoclinic $BiVO_4$ was prepared by a CTAB-assisted hydrothermal method from a modified preparation from Liu *et al*, 2009.[11] In a typical synthesis, 1 eq of $Bi(NO_3)_3 \cdot 5H_2O$ was dissolved in concentrated HNO_3 under magnetic stirring. In succession, 1.1 eq of NH_4VO_3 and 0.015 eq of CTAB were added to the solution. The pH of the above mixture was adjusted to 8.00 with an ammonia solution. The tan solution was transferred to a stainless steel autoclave maintained at 200°C for 5 hours followed by aging for 12 hours without stirring. The supernatant was discarded and the resulting yellow powder was filtered and washed with three successive treatments of water and ethanol then dried under vacuum at room temperature. The product fingerprint was analyzed by powder x-ray diffraction (XRD) and compared to literature sources. The product morphology was then analyzed by scanning electron microscopy (SEM)

Synthesis of *m*-$BiVO_4$ polyhedral crystals: $Bi(NO_3)_3.5H_2O$, NH_4VO_3 and Na_2SO_4 were added to water in a molar ratio 1:1:1.1, respectively. The mixture was stirring allowing the formation of a yellow solid. Both, solution and solid were quantitatively transfer with water into a glass vessel autoclave reactor and sealed. The reactor was put at 180^{o}C 24h. Once the reaction time is fulfilled, the solid is filtered and wash with three portions of cold water to remove all unreacted materials and the Na_2SO_4. The solid was dried at 140^{o}C 12h. The product fingerprint was analyzed by powder x-ray diffraction (XRD) and compared to literature sources. The product morphology was then analyzed by scanning electron microscopy (SEM)

2.2.2 Catalytic Test Results

CO_2 Reduction. Reduction of CO_2 was performed in a homemade closed gas system. In a typical reaction, 0.4 g of catalyst and 1.0 M NaOH were added to 200 mL of distilled water in a

quartz flat bottom flask adjacent to a water cooled quartz jacket containing a 300 W Xe arc-lamp. Prior to light irradiation, the reaction mixture was thoroughly degassed through vacuum and refill cycles to remove air and CO_2 was flowed into the system for 30 minutes at a pressure of 1.0 atm.

Formaldehyde quantification. Concentration of formaldehyde (as methanediol) concentration was determined by a modified colorimetric procedure by Nash.[17] A test solution was prepared with 2M ammonium acetate, 52.5 mM glacial acetic acid, and 20 mM acetylacetone. 2 mL of the test solution was added to 2 mL of the reaction solution containing formaldehyde and was heated at 60ºC for 10 minutes. The reaction mixture was allowed to cool to room temperature for 10 minutes before measured spectrophotometrically at 412 nm. The concentration was determined against a standard curve.

Formate quantification Concentration of dissolved formate was determined by a modified colorimetric procedure by Sleat and Mah.[18] 0.5 mL of the reaction mixture was added to 2 mL of 10% acetamide and .05% citric acid dissolved in a 1:1 mixture of isopropanol and water. To the test mixture, 0.1 mL of 30% sodium acetate and 7 mL of acetic anhydride are added. The test mixture is shaken and incubated at room temperature for 60 minutes and measured spectrophotometrically at 510 nm. The concentration was determined against a standard curve.

2.3 Results

Decomposition of $BiVO_4$

Monoclinic bismuth vanadate has been produced in a wide variety of isoforms, ranging from highly crystalline polyhedral crystals, nano-rods, and hyperbranched structures, with many

others in between[11–16,19–24]. In our study, we focused on using polyhedral crystals (*p*-$BiVO_4$) and hyperbranched structures (*h*-$BiVO_4$), as seen in Figure 2.3.1.

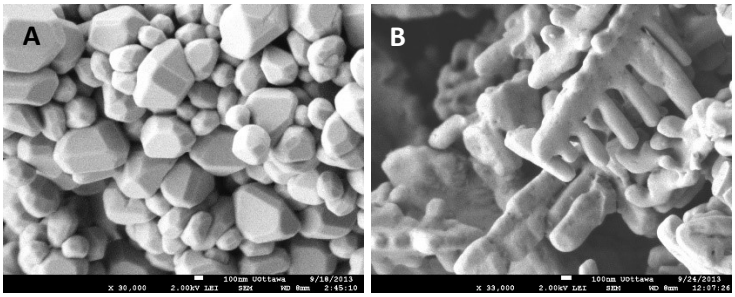

Figure 2.3.1. a) Polyhedral crystals of monoclinic $BiVO_4$ and b) hyperbranched crystals of monoclinic $BiVO_4$.

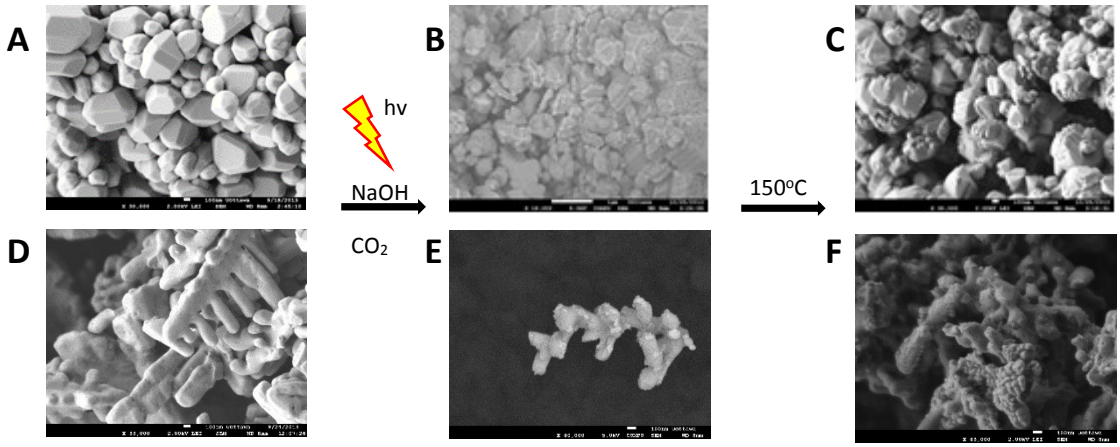

Figure 2.3.2. SEM images of (a) pristine, (b) inactive, and c) reactivated *p*-$BiVO_4$, and (d) pristine, (e) inactive and (f) reactivated *h*-$BiVO_4$.

In a 1M NaOH aqueous solution and under 1 atm of CO_2, $BiVO_4$ will become etched, and nanoparticles are deposited on the surface vertices of the catalyst as seen in Figure 2.3.2 b and e. In this state, the catalyst has become deactivated. The catalyst can be reactivated by heating to 130°C in an oven. Heated recovery will remove the electron rich deposits from the surface, although the catalyst remains irreversibly etched. This reactivated catalyst was tested for activity

and was shown to have reduced activity compared to pristine $BiVO_4$, which can be seen in Figure 2.3.5.

Energy dispersive x-ray spectroscopy (EDS) was used to identify the effect of etching and particle deposition on the surface of the catalyst, with the results shown in Table 2.3.1

Table 2.3.1. Energy dispersive spectroscropy (EDS) derived molar % of bismuth, vanadium and oxygen on the surface of *h*-$BiVO_4$. Results are average of three or more samples, $\pm$ SD.

Sample	% Bi	% V	% O
Pristine *h*-$BiVO_4$	15.3 $\pm$ 1.4	15.2 $\pm$ 1.5	69.5 $\pm$ 2.7
Inactive *h*-$BiVO_4$	17.6 $\pm$ 0.7	13.52 $\pm$ 0.4	69.4 $\pm$ 1.1
Reactivated *h*-$BiVO_4$	16.7 $\pm$ 0.3	13.92 $\pm$ 0.02	68.8 $\pm$ 0.4
Dried *h*-$BiVO_4$ filtrate	0.00	19.0 $\pm$ 2.4	81.0 $\pm$ 2.4

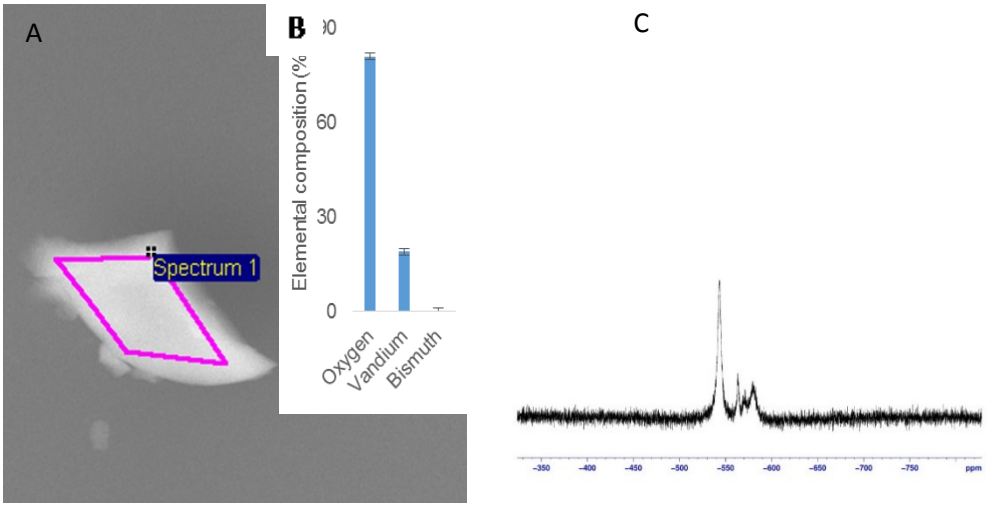

Figure 2.3.3. a) SEM image of dried filtrate after $BiVO_4$ was etched, b) elemental composition of particle obtained by EDS, and c) ^{51}V NMR of post-reaction filtrate.

The leeching of vanadium was confirmed by drying a sample of the filtrate and taking EDS measurements of the filtrate, which shows up as only vanadium and oxygen (Figure 2.3.3b). This is further confirmed by ^{51}V NMR of the filtrate which shows multiple peaks, characteristic of a mixture of aqueous vanadium oxides (Figure 2.3.3c).

In addition to visual modifications and vanadium leeching, the bulk inactive catalyst undergoes changes in its crystal structure, as indicated by powder x-ray diffraction (XRD) patterns in Figure 2.3.4.

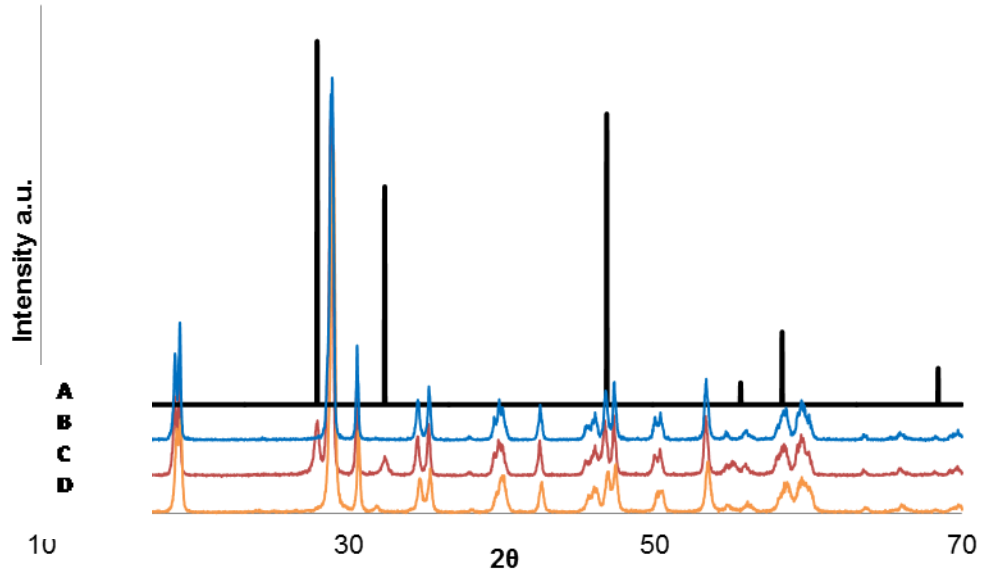

Figure 2.3.4. Powder X-ray Diffraction (XRD) patterns of (b) pristine, (c) inactive, and (d) reactivated *h*-$BiVO_4$. (a) Represents literature pattern of Bi_2O_{4-x}.

Reoxidation of organic products

In our hands, both *h*-$BiVO_4$ and *p*-$BiVO_4$ are indeed capable of reducing carbon dioxide into methanol. As expected, and previously described, the production rate of methanol slows down until it is zero.[12] However, in our hands, after production of methanol halts, we observe the

decrease loss of methanol, as well as the proposed formaldehyde intermediate, over time (Figure 2.3.5). Formate concentrations appear to stabilize after 3 hours without loss in activity. Formaldehyde and methanol activity decreases after recovery of the $BiVO_4$ catalyst, although the activity in formate formation does not appear to be effected by catalyst recovery.

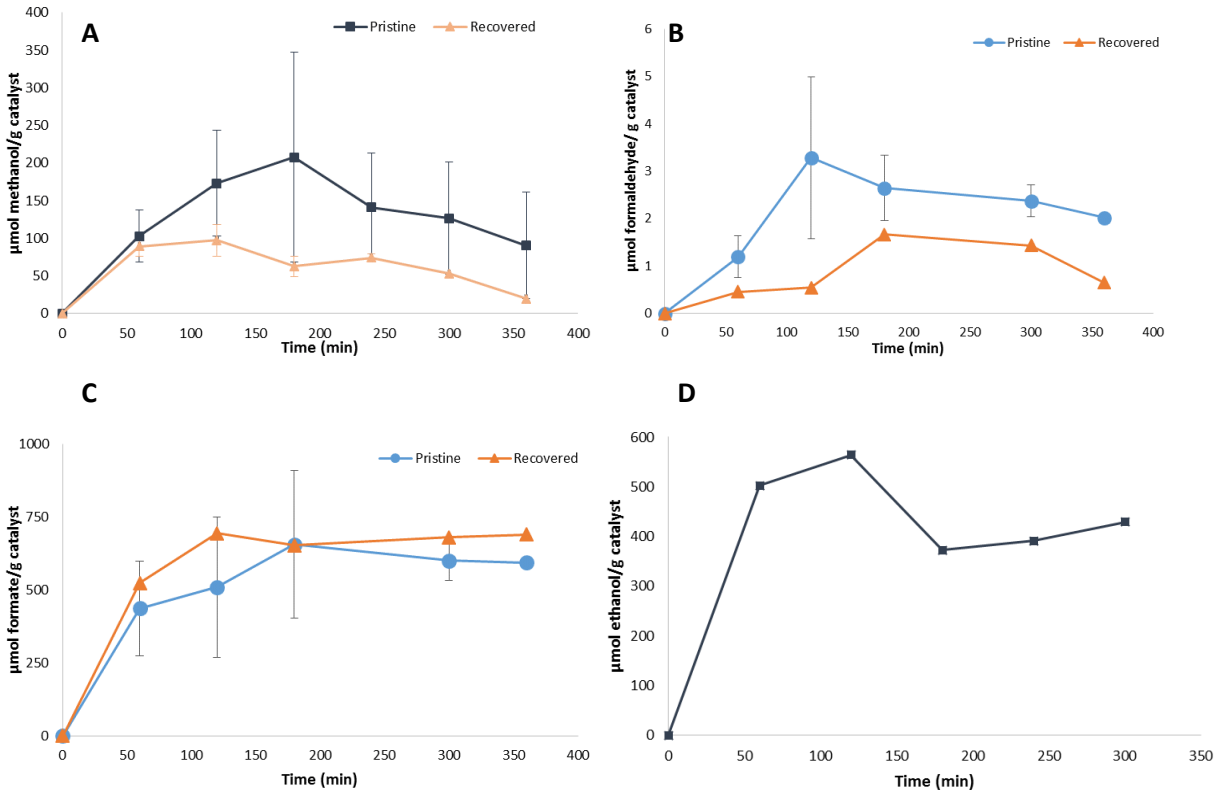

Figure 2.3.5. Concentration of a) methanol by GC-FID, b) formaldehyde by colorimetric analysis, and c) formate by colorimetric analysis over time. Results are average of two or more samples, $\pm$ SD. Concentration of ethanol, d), is provided as the results from a single experiment, without repetition.

No additional products were detected in these samples, although it must be noted that the photoreduction of CO_2 using $BiVO_4$ is an inconsistent process. On one occasion, ethanol was detected, although not in sufficient quantity to reliably quantify and repeat.

Potential oxidation products of 1M methanol, formaldehyde, and sodium formate (Table 2.3.2) in a 1M solution of NaOH were studied to help decipher the pathway for methanol reoxidation. In no cases were methane, carbon monoxide or other organic products observed.

Table 2.3.2. Quantitative analysis of oxidation and reduction of CO_2 reduction products with $BiVO_4$ after 24 hr. All reactions were performed with 150 μmoles $BiVO_4$, 180 mmoles starting material, 180 mmoles NaOH in a sealed glass vial up to 18 mL of liquid volume. Results are average of two samples.

Starting Material	MeOH (mmol)	CH_2O (μmol)	$HCOO^-$(μmol)	H_2 (μmol)
Methanol		28	13.4	3.6
Formaldehyde*	$4.0x10^2$		70.6	25.4
Sodium formate	0.3	n.d.		n.d.

*Formaldehyde was sourced from a commercial formalin solution containing 10-15% MeOH w/v.

Interestingly, when the deactivated catalyst from the CH_2O spiked reaction is observed by XRD and SEM, the evidence for the formation of Bi_2O_{4-x} nanoparticles becomes more pronounced than seen in typical experimental conditions (Figure 2.3.6). This effect is also seen with methanol, although to a lesser extent.

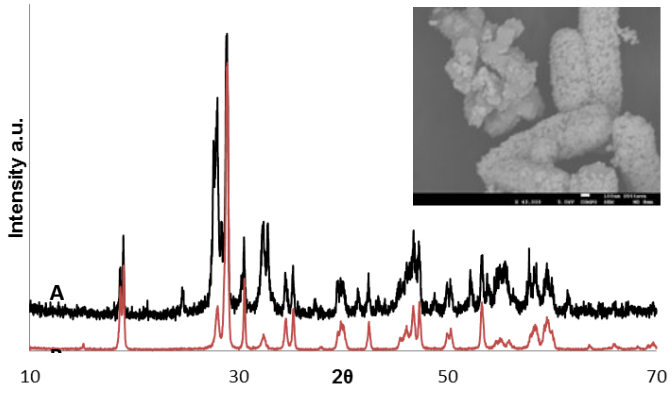

Figure 2.3.6. Comparison of powder XRD patterns of a) inactive *h*-$BiVO_4$ from formaldehyde spiked conditions and b) inactive *h*-$BiVO_4$ from typical conditions. SEM photo of *h*-$BiVO_4$ from formaldehyde spiked conditions is inset.

Vanadium-spiked $BiVO_4$ photoreduction of CO_2

To test the effect of vanadium in the stabilization and activation of $BiVO_4$, soluble vanadium species were added to the photochemical reaction solution. First, pristine *h*-$BiVO_4$ was added to a solution of vanadium oxides obtained from the filtrate of a previous *h*-$BiVO_4$ reaction. Second, pristine *h*-$BiVO_4$ was added to a solution of 15 mM NH_4VO_3 with 1M NaOH. Both solutions were degassed and filled with CO_2 followed by illumination, although neither was capable of CO_2 reduction.

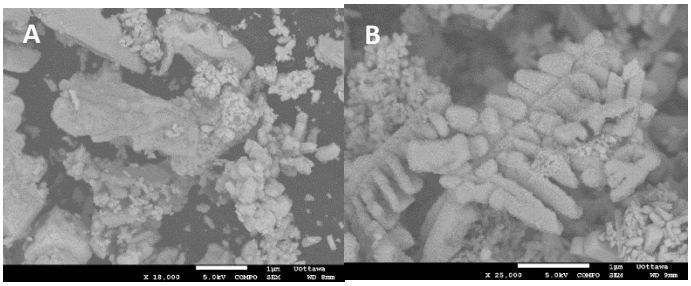

Figure 2.3.7. Comparison of post-reaction SEM images for *h*-$BiVO_4$ reactions spiked with a) ammonium vanadate and b) vanadium filtrate from previous reaction.

After filtration and drying the post-reaction catalysts, the ammonium vanadate doped catalyst exhibited a color change to tan, in contrast to the yellow of pristine *h*-$BiVO_4$, and the catalysts reacted in the presence of the vanadium filtrate. Both the structure and morphology of $BiVO_4$ was modified in two different ways, as shown in Figures 2.3.7 and 2.3.8.

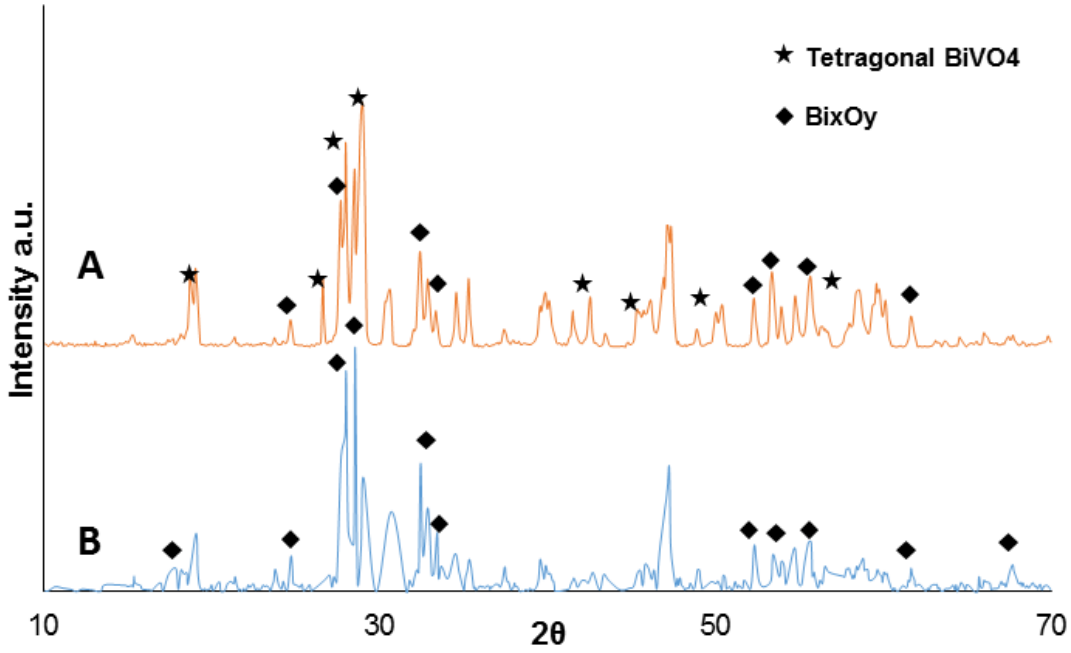

Figure 2.3.8. Comparison of post-reaction powder XRD patterns for *h*-$BiVO_4$ reactions spiked with a) ammonium vanadate and b) vanadium filtrate from previous reaction.

2.4 Discussion

In our hands, the activity of $BiVO_4$ for CO_2 photoreduction requires the use of base, specifically sodium hydroxide. Predictably, this results in the etching of the catalyst surface.[20] In fact, the etching of the catalyst surface occurs in neutral conditions as well, although to a lesser extent. After being exposed to 1M NaOH with and without illumination, the surface of the catalyst becomes etched along a single facet of the crystal. By using a backscatter filter to determine

surface electron density, deposited nanoparticles are revealed to be very dense, compared to the bulk $BiVO_4$ it has been deposited on (see Figures 2.3.2b and 2.3.2e).

In Table 2.3.1, we see that molar percent of oxygen does not change much from sample to sample, although vanadium and bismuth percentages are greatly altered in post-reaction. Pristine *h*-$BiVO_4$ has a ratio of 0.99 V/Bi, by surface molar percentage. This is compared to the inactive ratio of 0.77 and the recovered ratio of 0.83. This suggests that a large amount of surface vanadium is irreversibly lost during the reaction, likely caused by leeching in the alkaline conditions. This is confirmed by the presence of a series of vanadium oxides in the filtrate (Figure 2.3.3)

XRD data in Figure 2.3.4 reveals the formation of a new, crystalline, material contaminating the sample of $BiVO_4$. The contamination peaks correspond with literature samples of a mixed valence bismuth oxide, denoted as Bi_2O_{4-x}.[25] Attempts to separate this contaminant from the bulk $BiVO_4$, as well as attempts to synthesize Bi_2O_{4-x} as a reference have been unsuccessful. The assignment of Bi_2O_{4-x} corresponds to the electron rich deposits seen in Figure 2.3.2 (b,e).

In Figure 2.3.5a, the loss of methanol could theoretically be attributed to the further reduction to methane, although we have never detected methane down to a detection limit of ~10 p.p.m. from an enclosed vial with a headspace of 1 mL. The methanol loss can otherwise come from re-oxidation into lower value organics, including formaldehyde, formate, and full re-oxidation to carbon dioxide (or carbonate).

In no cases were any of methane, carbon monoxide, glyoxal, glycoaldehyde or acetaldehyde detected. This provides evidence for CO_2 photoreduction to initiate via monodentate binding, with stepwise proton coupled electron transfers producing methanol as a final product (Figure

1.3.1.2A). However, both formic acid and formaldehyde can be produced via reoxidation of methanol in either pathway, and the production of ethanol as reported by by Huang *et al*, and one time production by our lab, suggests the glyoxal pathway (Figure 1.3.1.2C) is favorable. Ultimately, we cannot provide any conclusive evidence to prove or disprove any proposed reduction pathway.

The heavy coating of the active surface of $BiVO_4$, which is present only in inactive samples, suggests that this coating is at least partially responsible for the deactivation of the catalyst. Furthermore, the extreme example of coating in the sample in Figure 2.3.6 suggests the deposition of Bi_2O_{4-x} is caused by a reaction with formaldehyde at the surface of the catalyst, one of the key intermediates in the reduction to methanol.

When $BiVO_4$ is illuminated in the presence of the vanadium filtrate, the catalyst was not etched and retained the same morphology, with the slight exception of a layer of nano-particulate matter was deposited on the surface of the catalyst (Figure 2.3.7b). Conversely, the addition of ammonium vanadate resulted in a notable change in catalyst morphology. Instead of regular hyperbranched crystals, the ammonium vanadate-doped catalyst underwent phase changes to a complex mixture of hyperbrached crystals, irregular plates and nanoparticles.

Interestingly, powder XRD analysis of both vanadium doped samples show signs of phase changes. The filtrate doped samples produce a mixture of monoclinic $BiVO_4$ as well as a series of bismuth oxides (e.g. Bi_2O_3), although no tetragonal or orthorhombic $BiVO_4$ was formed. Conversely, ammonium vanadate doped $BiVO_4$ matches well tetragonal $BiVO_4$, in addition to monoclinic $BiVO_4$ and series of Bi_xO_y species.

2.5 Concluding remarks

This work has provided valuable insight into the decay mechanism of $BiVO_4$ as a photocatalyst for CO_2 photoreduction. Unfortunately, for the long-term prospects of $BiVO_4$, it appears that catalytic decay is caused by reoxidation of its own products of CO_2 reduction. In this case, even as the catalyst activity is improved (by improving charge separation, decreasing recombination rates, etc.) $BiVO_4$ will rapidly decay and will require constant recovery by heating. However, vanadium leeching and catalyst etching are irreversible processes, and after every catalytic cycle of photoreduction/recovery, a portion of the initial catalyst will be lost, until the cycle is halted.

The major and minor products formed in this reaction do provide some insight into the mechanism of CO_2 photoreduction for $BiVO_4$ (and likely some other photosemiconductors). While formaldehyde, formate and methanol are all possible products in all three proposed CO_2 reduction pathways, the lack of other key intermediates detected (CO, glyoxal, etc.) suggests the formaldehyde pathway is the most likely pathway for CO_2 reduction, at least when catalyzed by $BiVO_4$.

2.6 References

(1) Inoue, T.; Fujishima, A.; Konishi, S.; Honda, K. *Nature* **1979**, *227*, 637–638.

(2) Qin, G.; Zhang, Y.; Ke, X.; Tong, X.; Sun, Z.; Liang, M.; Xue, S. *Appl. Catal. B Environ.* **2013**, *129*, 599–605.

(3) Qin, S.; Xin, F.; Liu, Y.; Yin, X.; Ma, W. *J. Colloid Interface Sci.* **2011**, *356*, 257–261.

(4) Wang, W. N.; An, W. J.; Ramalingam, B.; Mukherjee, S.; Niedzwiedzki, D. M.; Gangopadhyay, S.; Biswas, P. *J Am Chem Soc* **2012**, *134*, 11276–11281.

(5) Yang, H. C.; Lin, H. Y.; Chien, Y. S.; Wu, J. C. S.; Wu, H. H. *Catal. Letters* **2009**, *131*, 381–387.

(6) Xie, Y. P.; Liu, G.; Yin, L.; Cheng, H.-M. *J. Mater. Chem.* **2012**, *22*, 6746.

(7) Li, X.; Chen, J.; Li, H.; Li, J.; Xu, Y.; Liu, Y.; Zhou, J. *J. Nat. Gas Chem.* **2011**, *20*, 413–417.

(8) Kisch, H.; Lutz, P. *Photochem. Photobiol. Sci.* **2002**, *1*, 240–245.

(9) Sekizawa, K.; Maeda, K.; Domen, K.; Koike, K.; Ishitani, O. *J. Am. Chem. Soc.* **2013**, 4596–4599.

(10) Suzuki, T. M.; Tanaka, H.; Morikawa, T.; Iwaki, M.; Sato, S.; Saeki, S.; Inoue, M.; Kajino, T.; Motohiro, T. *Chem. Commun. (Camb).* **2011**, *47*, 8673–8675.

(11) Liu, Y.; Huang, B.; Dai, Y.; Zhang, X.; Qin, X.; Jiang, M.; Whangbo, M. H. *Catal. Commun.* **2009**, *11*, 210–213.

(12) Mao, J.; Peng, T.; Zhang, X.; Li, K.; Zan, L. *Catal. Commun.* **2012**, *28*, 38–41.

(13) Choi, S. K.; Choi, W.; Park, H. *Phys. Chem. Chem. Phys.* **2013**, *15*, 6499–6507.

(14) Lin, F.; Wang, D.; Jiang, Z.; Ma, Y.; Li, J.; Li, R.; Li, C. *Energy Environ. Sci.* **2012**, *5*, 6400.

(15) Gawande, S. B.; Thakare, S. R. *Int. Nano Lett.* **2012**, *2*, 11.

(16) Xi, G.; Ye, J. *Chem. Commun.* **2010**, *46*, 1893–1895.

(17) Nash, T. *Biochem. J.* **1953**, *55*, 416–421.

(18) Sleat, R.; Mah, R. a. *Appl. Environ. Microbiol.* **1984**, *47*, 884–885.

(19) Zhou, Y.; Vuille, K.; Heel, A.; Probst, B.; Kontic, R.; Patzke, G. R. *Appl. Catal. A Gen.* **2010**, *375*, 140–148.

(20) Seabold, J. a; Choi, K.-S. *J. Am. Chem. Soc.* **2012**, *134*, 2186–2192.

(21) Su, J.; Guo, L.; Bao, N.; Grimes, C. a. *Nano Lett.* **2011**, *11*, 1928–1933.

(22) Su, J.; Guo, L.; Yoriya, S.; Grimes, C. a. *Cryst. Growth Des.* **2010**, *10*, 856–861.

(23) Chen, Q.; Zhou, M.; Ma, D.; Jing, D. *J. Nanomater.* **2012**, *2012*.

(24) Wang, M.; Liu, Q.; Che, Y.; Zhang, L.; Zhang, D. *J. Alloys Compd.* **2013**, *548*, 70–76.

(25) Begemann, B.; Jansen, M. *J. Less Common Met.* **1989**, *156*, 123–135.

Chapter 3: Light-switchable catalyst for rapid release of H_2 from *p*-formaldehyde

3.1 Introduction

Compared to formic acid and methanol dehydrogenation, production of H_2 directly from formaldehyde (and not as an intermediate in methanol dehydrogenation) is a young pursuit. Only two homogeneous catalysts have been described thus far in the literature,[1,2] while only a few of heterogeneous catalysts have been described with turnover frequencies greater than 1 h^{-1}.[3–6] Among all of these catalysts, the most efficient dehydrogenation catalyst (Ag/γ-Al_2O_3) is capable of a mere TOF of 113 h^{-1}. This pales in comparison to the state of the art methanol (up to 4700 h^{-1}) and formic acid (up to 158 000 h^{-1}) catalysts, so a substantial amount of research will be required for formaldehyde dehydrogenation to become industrially relevant.

In addition to maximizing TOFs, a formaldehyde catalyst (or any dehydrogenation catalyst) will be limited by cost. The most effective dehydrogenation catalysts are typically dependant on Ru and Ir metals, and/or expensive ligand systems. If these catalysts are either inefficient, or not long lasting, the cost of the precious metals (and ligands) will be prohibitive for industrial relevance. In addition, catalysts which require inert atmospheric conditions to prevent catalyst decay add cost to future applications. Therefore, it is beneficial to develop a dehydrogenation catalyst using cheap and abundant metals, cheap ligands (if any) and that is active in ambient air and temperatures. Finally, the most important process for the catalytic system to be relevant in H_2 production (as opposed to only H_2 storage) is the cost and ability to recover the storage substrate.

The most active dehydrogenation catalysts previously reported in the literature will fully oxidize the hydrogen carrier into carbon dioxide (or carbonate in solution). As demonstrated previously, current yields and efficiency of carbon dioxide photoreduction into hydrogen storage molecules are low. A significant cause of this is due to the high energy cost to activate CO_2. Interestingly, the Crabtree group has reported a series of iridium catalysts which preferentially dehydrogenate methanol into formate, although some total oxidation to carbonate is still observed.[7] Although, to our knowledge, there is no active research in water oxidation coupled to formate reduction, it provides an interesting target for an organic shuttle for H_2 production if an effective dehydrogenation catalyst that selectively oxidizes one of methane, methanol or formaldehyde into formate (or formic acid) may be developed.

Notably, a series of heterogeneous catalysts are reported to selectively produce hydrogen and formate from formaldehyde, although the active catalysts are based on palladium or silver nanocatalysts.[4–6]

As previously noted, both homogenous catalysts appear to have metal-hydroxide ligands in the catalytically active species.[1,2] From here, a search for stable catalysts with a metal-hydroxide bond for formaldehyde dehydrogenation can be started. Other members of the Gambarotta lab have demonstrated simple metal salts in alkaline solutions to be active in selective formaldehyde dehydrogenation to formate (including iridium and ruthenium, among others). These catalysts work at room temperature without any external stimulus as the dehydrogenation is thermodynamically favorable. An additional challenge would be to develop a dehydrogenation catalyst which can be activated by an abundant external source to release hydrogen on demand.

Ferrocyanide is a cheap and readily available iron(II) hexacyano catalyst. When irradiated with ~ 375 nm light in water, the ferrocyanide dissociates a single cyanide ligand (equation 1), which is replaced by a water ligand (or hydroxide in basic conditions).

$$[Fe(CN)_6]^{4-} + H_2O \leftrightarrow [Fe(CN)_5OH_2]^{3-} + CN^- \quad (1)$$

In this work, a light-switchable and inexpensive system based on Fe is highlighted and explored, efficiently producing H_2 gas from *p*-FA at room temperature, while selectively generating the formate anion as the only co-product. The system is oxygen-resilient and chemically robust. Therefore, it could be in principle combined with a formate reduction cycle to design a tandem catalyst for water splitting.

3.2 Materials and Methods

Materials. Paraformaldehyde, 37% formaldehyde solution, and sodium ferrocyanide decahydrate, were purchased from Sigma Aldrich. Formic acid was purchased from Acros Organics. Sodium thiosulfate was purchased from Oakwood Chemicals. Iodine was purchased from Strem. Acetamide was purchased from Fluka. Citric acid was purchased from Fisher Scientific. Acetic anhydride was purchased from VWR. Chemicals were used without further purification. If not specifically mentioned, all reactions were carried out in distilled water without degassing or other modifications.

Analytical Equipment. pH measurements were taken with a Hanna HI 2210 benchtop pH meter with a general purpose combination pH electrode, both purchased from Sigma-Aldrich. Powder XRD diffractograms were obtained on a Rigaku Ultima IV diffractometer set to 2 $2\theta^o$/min from 10-70 $2\theta^o$. UV-Vis spectra were obtained on a Specmate UV-1100 spectrometer. H_2, CO_2, CO and O_2 gas detection and identification was carried out with an Agilent 7820A GC equipped with

a thermal conductivity detector (TCD), using an Agilent GS-CarbonPlot column (for CO_2) or an Agilent HP-Molesieve column (for all other gasses).

Computational details. Molecular geometries of the model complexes were optimized without constraints via DFT calculations using the B3LYP[10] functional and TZVP[11] basis set for all atoms. Frequency calculations at the same level of theory have also been performed to confirm all of possible transition states (one imaginary frequency), and to provide free energies at 298.15 K, which include entropic contributions by taking into account the vibrational, rotational, and translational motions of the species under consideration. Transition states were located using the Berny algorithm. The Polarizable Continuum Model (PCM) was used to correct the energies taking into account the reaction occurs in water. All calculations were performed with the Gaussian 09 software package.[12]

3.2.1 Catalytic Test Results

Dehydrogenation of *p*-FA. In a typical experiment, 50 mmol of *p*-FA were added to 250 mmol of NaOH in H_2O, in a round bottomed flask connected to the volumetric apparatus at which point 0.5 mmol of $Na_4Fe(CN)_6 \bullet (H_2O)_{10}$ was added. The reaction mixture was illuminated with a 300 W Xe arc-lamp to yield 825 mL of H_2 in 300 min (67% yield). This protocol was repeated for use with numerous *p*-FA, NaOH and catalyst concentrations, as well as commercial 37% FA solutions to replace *p*-FA. This protocol was repeated for further additions of substrate when appropriate. This protocol was also repeated at various starting temperatures, where appropriate.

Determination of reaction kinetics. In a typical experiment, 50 mmol of *p*-FA were added to 250 mmol of NaOH in H_2O, in a round bottomed flask connected to the volumetric apparatus at which point 0.5 mmol of $Na_4Fe(CN)_6 \bullet (H_2O)_{10}$ was added. The reaction mixture was irradiated

with a 300 W Xe lamp and the gaseous outflow of the solution was hooked up to a Restek ProFLOW 6000 Electronic Flowmeter connected to a computer.

3.2.2 Product Analysis

Determination of formate concentration. Concentration of dissolved formate was determined according to a modified colorimetric procedure by Sleat and Mah.[8] An aliquot of 0.5 mL of the reaction mixture was added to 2 mL of 10% acetamide and 0.05% citric acid dissolved in a 1:1 mixture of isopropanol and water. To the test mixture, 0.1 mL of 30% sodium acetate and 7 mL of acetic anhydride are added. The test mixture was shaken and incubated at room temperature for 60 minutes and measured spectrophotometrically at 510 nm. The concentration was determined against a standard curve.

Determination of formaldehyde concentration. Formaldehyde concentrations were determined through iodine / sodium thiosulphate titrations.[9] To a 10 mL sample of the reaction mixture, de-ionised water (20 mL), iodine (25 mL, 0.05M/L in methanol) and sodium hydroxide (10 mL, 1.0M) were added and stirred for 10 minutes followed by the addition of sulphuric acid (15 mL, 1.0M). The sample solution was then titrated with sodium thiosulphate, with addition of a 1% starch solution as an indicator once the solution turned light yellow. The concentration of formaldehyde was then calculated by a standard curve.

Isolation of iron oxide. Iron oxide was collected after allowing a standard reaction to continue for 5 days with a continuous addition of pFA and NaOH. A brown-red precipitate slowly formed which was centrifuged, washed and dried prior to XRD.

3.3 Results

Fundamentals

Figure 3.3.1 demonstrates the dependence of light on the dehydrogenation of formaldehyde by ferrocyanide in basic, aqueous media. Clearly, the catalyst is wholly inactive in the dark, and can be easily restarted after several hours (or days) in the dark simply by re-illuminating the reaction mixture.

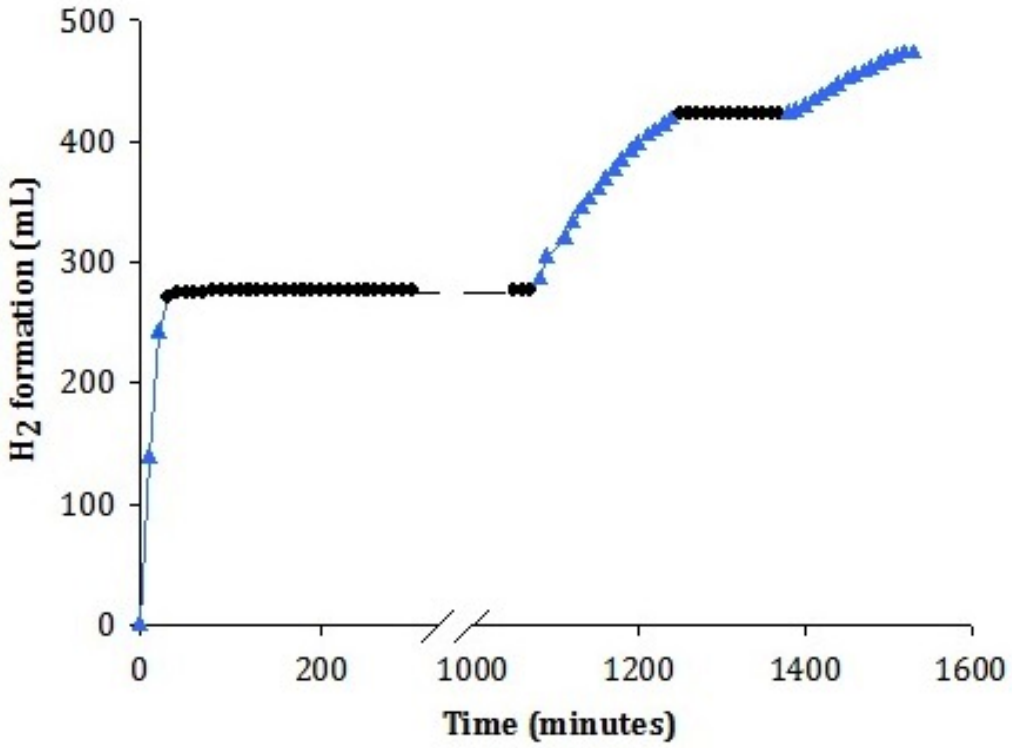

Figure 3.3.1. Effect of illumination on hydrogen evolution catalysis over time from single addition of 66.6 mmoles of *p*-FA, 325 mmoles of NaOH and 2 mmoles of $Na_4Fe(CN)_6$ at room temperature. (Δ) represents periods when catalyst is illuminated and (●) represents periods when catalyst is in the dark.

When paraformaldehyde is dissolved in a 1M NaOH aqueous solution, a majority of formaldehyde will be converted to the hydrated form (methanediol). Methanediol, in basic media, will spontaneously disproportionate into methanol and a formate anion, by the mechanism of the Cannizzaro reaction (equation 2).

$$2\ CH_2O_{(l)} + NaOH_{(aq)} \rightarrow HCOONa_{(aq)} + CH_3OH_{(l)} \qquad (2)$$

The rate of this reaction is concentration and temperature dependent. Figure 3.3.2 shows the reaction rate of this reaction using standard conditions.

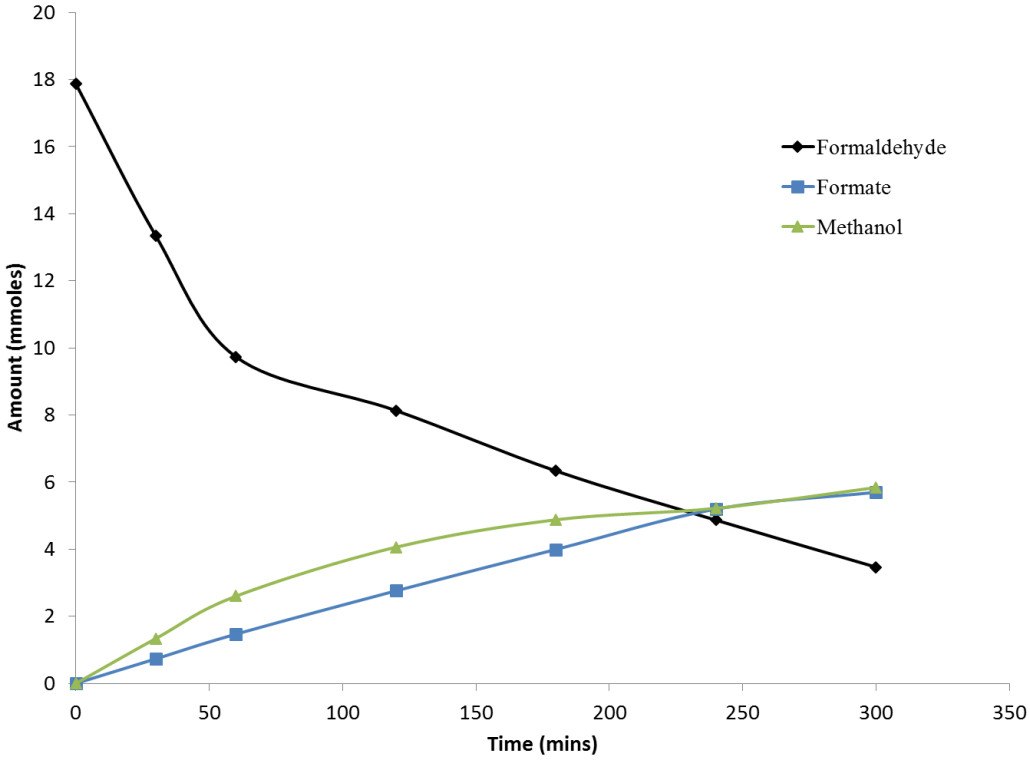

Figure 3.3.2. Formation of formate and methanol versus formaldehyde consumption via the Cannizzaro reaction at room temperature.

The plot of methanol in Figure 3.3.2 is the value of methanol produced after time zero. The actual moles of methanol present is far greater than that produced by the Cannizzaro reaction, as

every molecule of *p*-FA (8-100 FA monomers) contains one molecule of methanol. Commercial solutions of methanediol also contain 15 wt% methanol as a stabilizing agent.

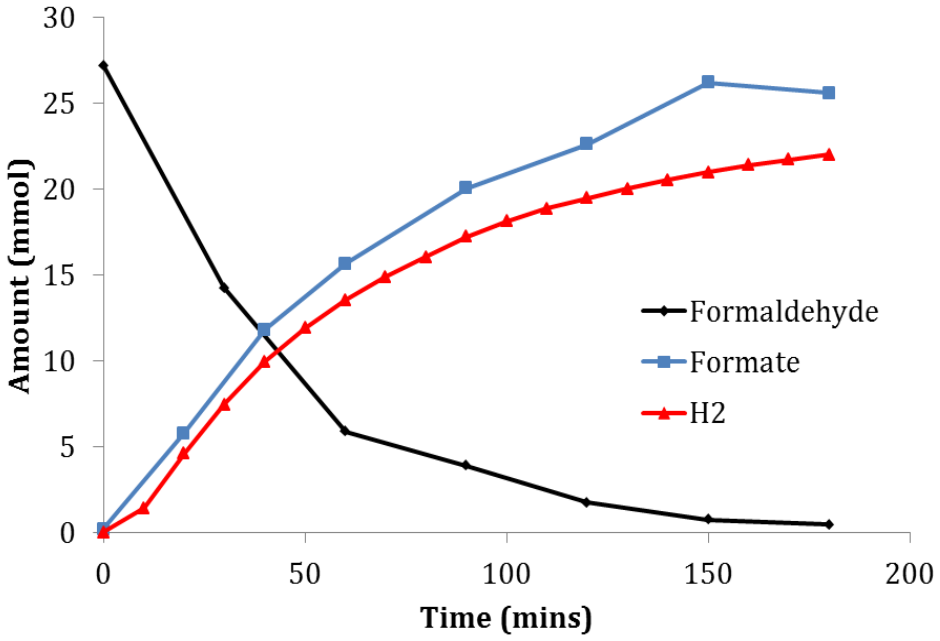

Figure 3.3.3. Formation of hydrogen and sodium formate compared to formaldehyde consumption when irradiated with light in the presence of $Na_4Fe(CN)_6$ at room temperature. Reaction occurs according to equation 2.

The consumption of formaldehyde traces well with the production of the formate anion. However, the hydrogen production occurs at a slightly reduced yield, which is the result of the aforementioned Cannizzaro reaction parasitizing formaldehyde and producing formate and methanol (Figure 3.3.2). Hydrogen was quantified by collecting the gasses in a graduated cylinder, and analysed for purity by gas chromatography, which can be seen in Figure 3.3.4.

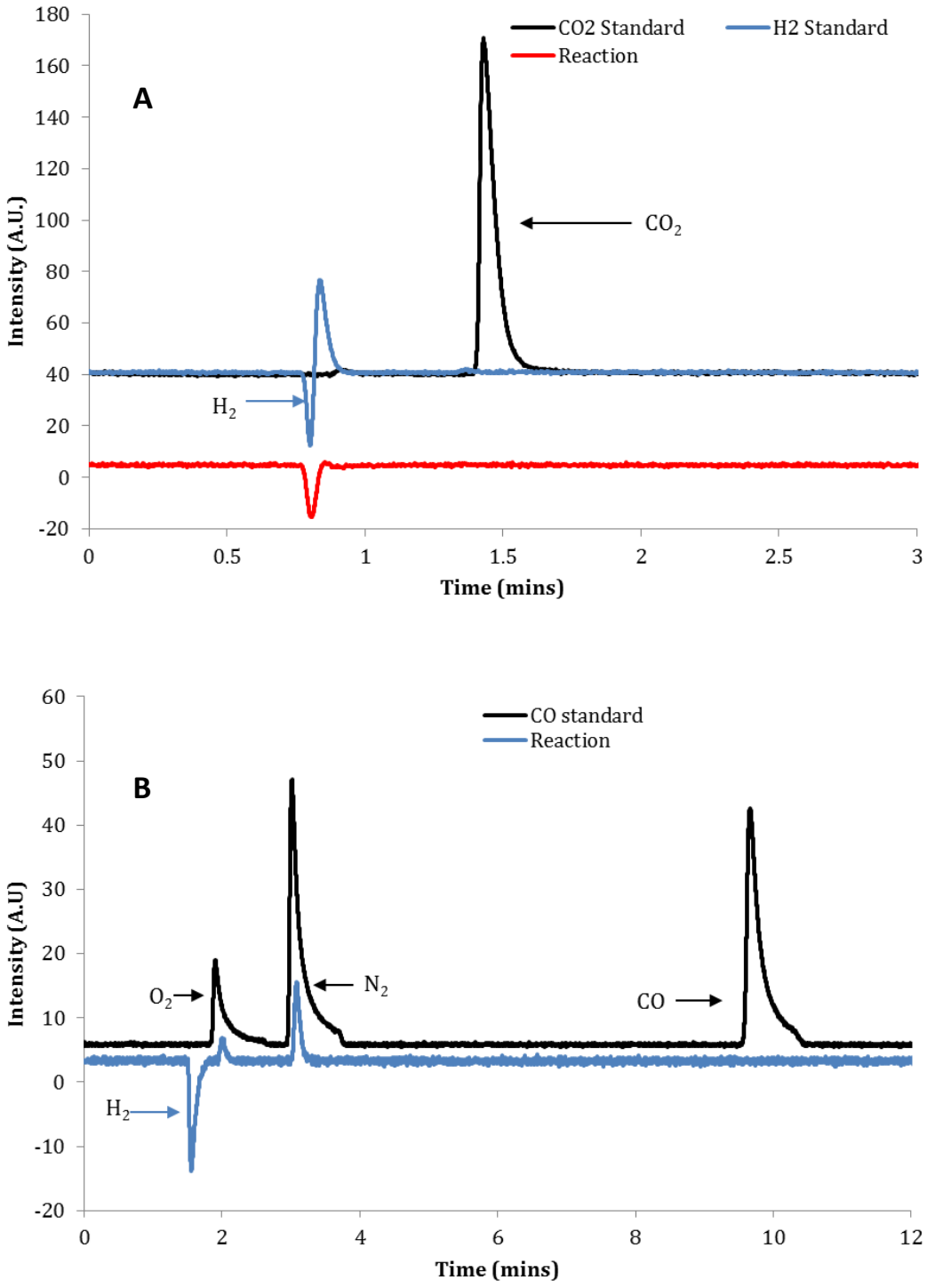

Figure 3.3.4. GC traces of collected gas using a) a GS-CarbonPlot column for the detection of H_2 and CO_2, and b) an HP-Molesieve column for the detection of H_2, O_2, N_2 and CO. CO_2 detection is sensitive to 10 ppm, and CO detection is sensitive to 1 ppm.

Reaction Rates

While the temperature dependence of the Cannizzaro reaction is well described, the effect of the initial temperature for formaldehyde dehydrogenation was also tested (Figure 3.3.5). The starting temperature was used as a model for the effect of temperature on the total reaction, due to the inability to continuously control the reaction temperature without inhibiting the pathway of light. The final temperature in all cases was 23 ˚C (± 0.5 ˚C).

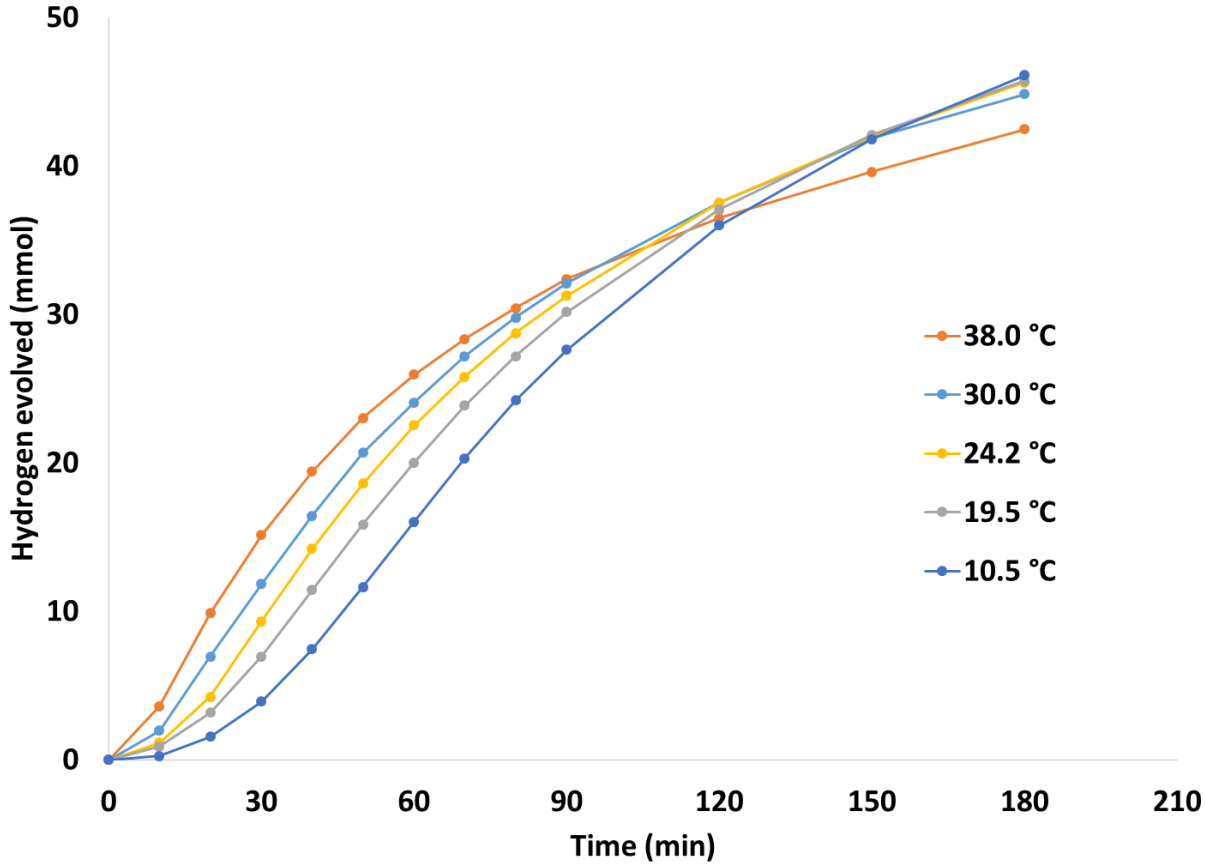

Figure 3.3.5. Effect of initial temperature on the dehydrogenation of formaldehyde by $Na_4Fe(CN)_6$. The final reaction temperature was 23 ˚C (± 0.5 ˚C) for all reactions. All reactions were carried out with 250 mmoles *p*-FA, 500 mmoles NaOH, and 0.5 mmoles $Na_4Fe(CN)_6$.

High temperatures enhanced the initial catalytic activity of the catalyst. The catalytic activity after 20 minutes for catalysis at 38 °C was 58 mL min^{-1} g^{-1}_{cat} (TOF = 60 h^{-1}), compared to just 15 mL min^{-1} g^{-1}_{cat} (TOF = 15.5 h^{-1}) at 10.5 °C. The final reaction rate of lower temperature reactions exceeded the higher temperature reactions. This is expected as the concentration of formaldehyde is higher at the end of the reaction for the lower temperature reactions. However, it was unexpected that the final volume of lower (and slower) initial temperatures exceeded the higher (and faster) reactions.

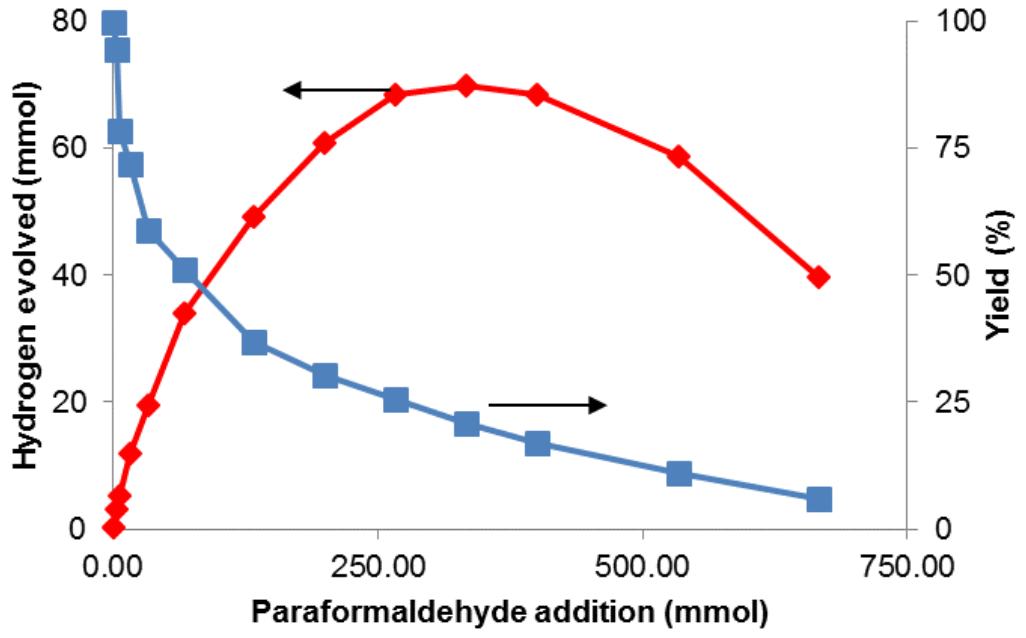

Figure 3.3.6. Production of hydrogen and yield of H_2 with variable initial concentration of p-FA. All reactions were carried out with 325 mmoles of NaOH and 0.5 mmoles of $Na_4Fe(CN)_6$ at room temperature.

Figure 3.3.6 demonstrates the dependence of both total hydrogen volume and yield of H_2 on the relative concentration of NaOH to formaldehyde. Total production peaks when NaOH is in a slight excess of formaldehyde (1.1 eq NaOH), although yield is low at 21%. Quantitative yields

of H_2 can be obtained, although this occurs when NaOH is in great excess (>1,000 eq) and the catalyst is also in excess of substrate (1.7 eq). High yields of > 90% are still available with 112.5 eq of NaOH and 0.17 eq of catalyst.

Figure 3.3.7 indicates the tradeoff between high TON and yield. At very low catalyst loadings (0.005 mol%), very high turnovers are obtained (>8000), although the yield drops below 40%. At higher loadings (>0.5 mol%) turnovers continue to drop although the yield begins to stabilize at approximately 50%.

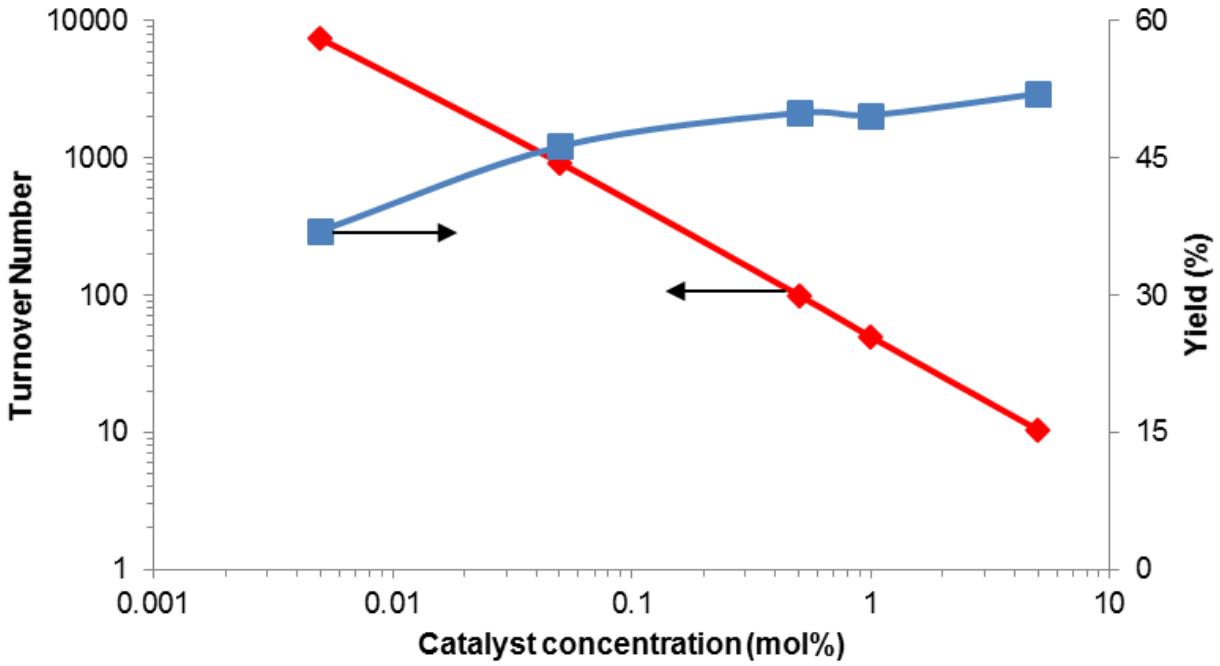

Figure 3.3.7. Catalytic turnover number (TON) and yield of H_2 with variable $Na_4Fe(CN)_6$ concentration relative to *p*-FA. All reactions were carried out with 50 mmoles of *p*-FA and 250 mmoles of NaOH at room temperature

The effect of several hydroxide bases on the activity of the catalyst was investigated, with NaOH and KOH used in Figure 3.3.8. Lithium, calcium, magnesium and barium hydroxide were also tested, but yielded zero activity. Non-metal hydroxide bases were also tested, including

ammonium hydroxide, sodium (bi)carbonate, pyridine, and trimethylamine, all of which yielded zero hydrogen.

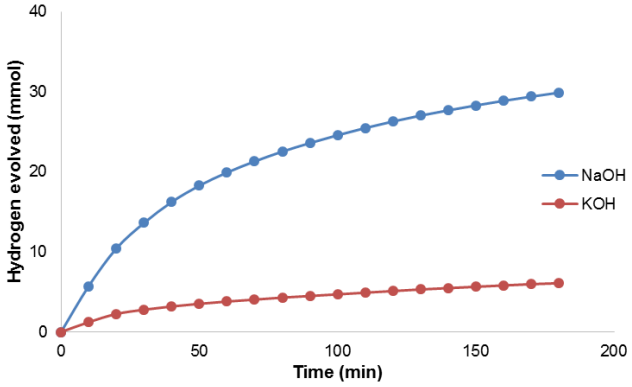

Figure 3.3.8. Production of H_2 over time using either NaOH or KOH as a base. In each reaction, 500 mmoles of either NaOH or KOH was used with 250 mmoles of *p*-FA and 0.5 mmoles of $Na_4Fe(CN)_6$.

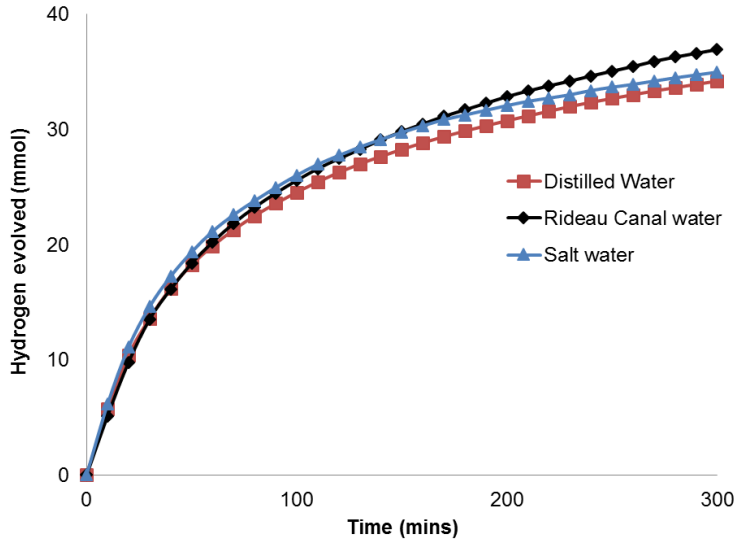

Figure 3.3.9. Production of H_2 over time taking place in various water sources. All reactions were carried out with 66.6 mmoles of *p*-FA, 375 mmoles of NaOH and 2 mmoles $Na_4Fe(CN)_6$ at room temperature.

The effect of water purity on catalytic activity was investigated in water taken from three sources. Regardless of whether the reaction occurred in distilled water, 3.5% NaCl (to match the average salinity of the ocean), or water taken directly from canal water, there was no significant difference in the activity of the catalyst. Figure 3.3.9 shows the nearly identical reaction rates and final production from the three sources. In order to further elucidate the effect of additives on dehydrogenation efficiency, a series of metal salts and oxides were added to a standard dehydrogenation reaction.

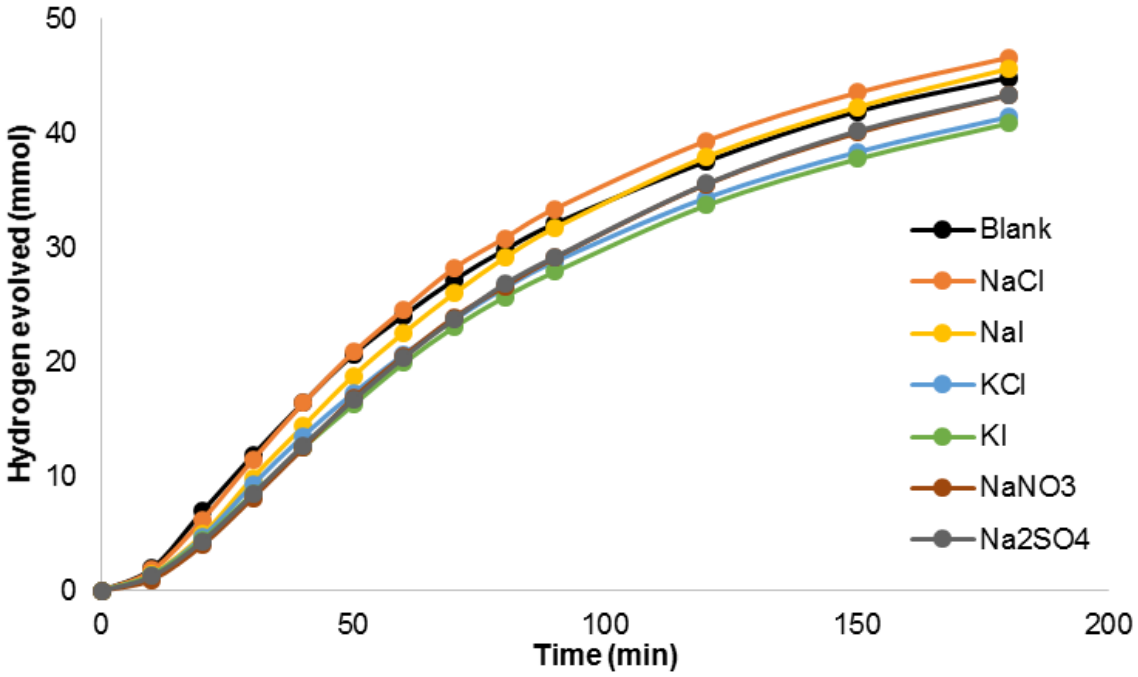

Figure 3.3.10. Production of hydrogen over time in the presence of a series of metal salts. All reactions were performed with 250 mmoles *p*-FA, 500 mmoles NaOH, 0.5 mmoles $Na_4Fe(CN)_6$ and 20 mmoles of additive (if applicable) at room temperature.

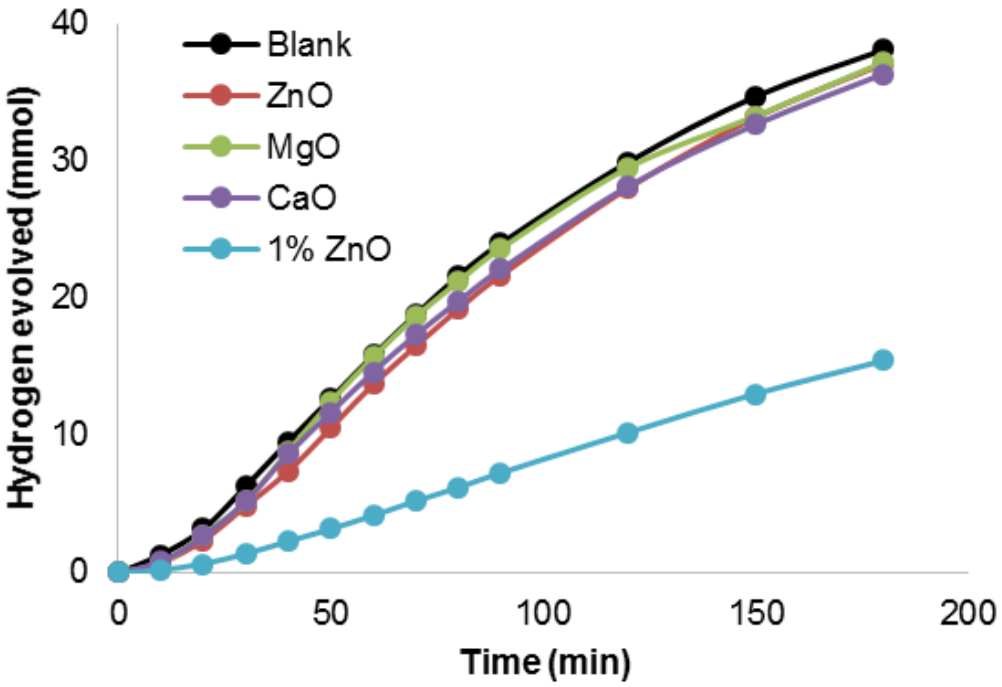

Figure 3.3.11. Production of hydrogen over time in the presence of a series of metal oxides. All reactions were performed with 250 mmoles *p*-FA, 500 mmoles NaOH, 0.5 mmoles $Na_4Fe(CN)_6$ and 250 mg (0.1 wt%) of additive (if applicable) unless otherwise noted, at room temperature.

The production of hydrogen was tested with a regular addition of *p*-FA and sodium hydroxide. The first experiment utilized the addition of a 1:5 molar ratio of *p*-FA and NaOH (Figure 3.3.12). This was expected to obtain a rapid reaction rate, and moderate yields (as expected from Figure 3.3.6). The reaction was also tested with the addition of a 1:1 molar ratio of *p*-FA and NaOH, after the initial addition of 250 mmoles of NaOH and 50 mmoles of *p*-FA (Figure 3.3.13).

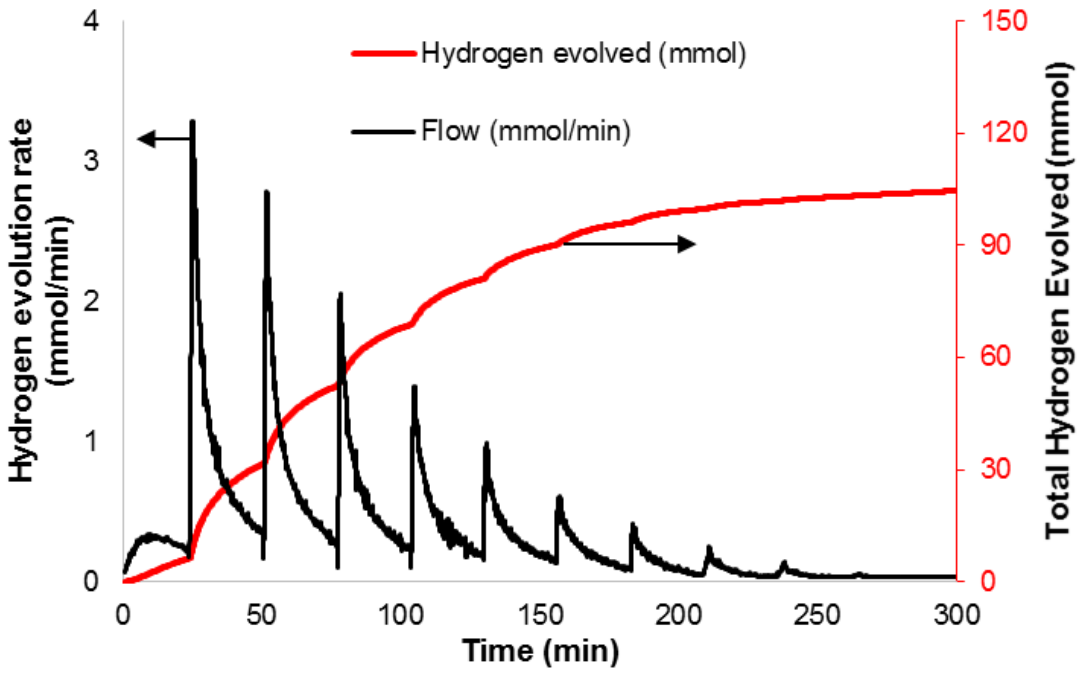

Figure 3.3.12. Rate of hydrogen formation and productivity of H_2 with regular additions of NaOH/*p*-FA. The reaction rate is visualized as a moving average trendline (n = 50, equivalent to 25 seconds) for clarity. The initial reaction mixture contained 50 mmoles *p*-FA, 250 mmoles NaOH and 0.5 mmoles of $Na_4Fe(CN)_6$. Every 30 minutes, 50 mmoles *p*-FA and 250 mmoles NaOH were added.

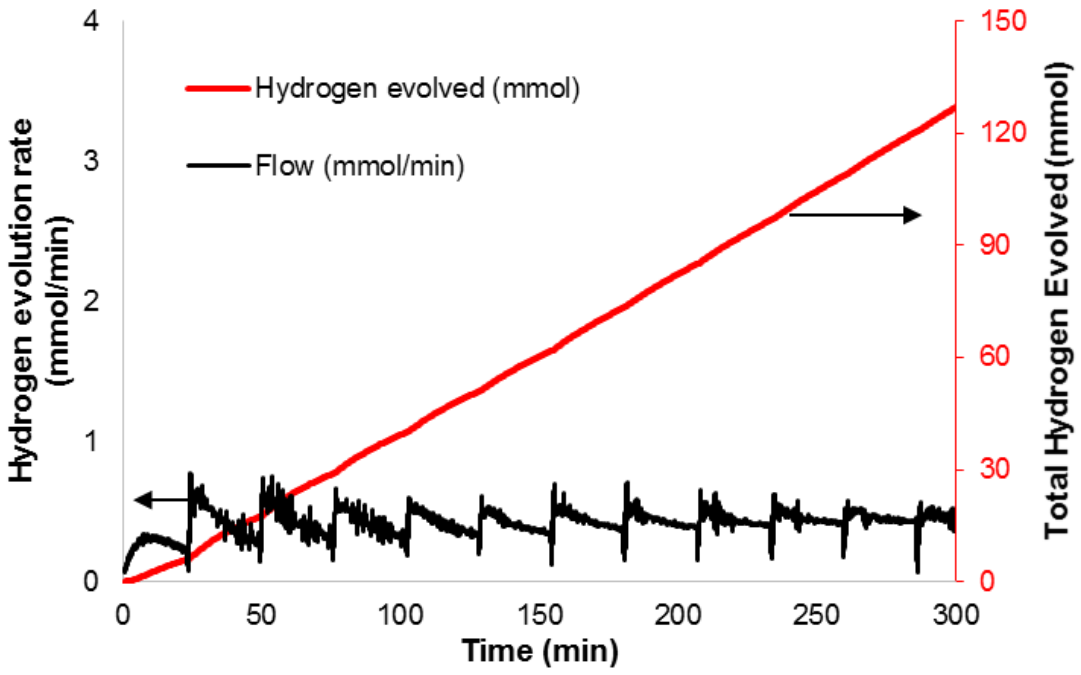

Figure 3.3.13. Rate of hydrogen formation and productivity of H_2 with regular additions of NaOH/*p*-FA. The reaction rate is visualized as a moving average trendline (n = 50, equivalent to 25 seconds) for clarity. The initial reaction mixture contained 50 mmoles *p*-FA, 250 mmoles NaOH and 0.5 mmoles of $Na_4Fe(CN)_6$. Every 30 minutes, 50 mmoles *p*-FA and 50 mmoles NaOH were added.

Deactivation and Decomposition

After demonstrating the stability of hydrogen evolution after the regular addition 1:1 *p*-FA:NaOH, long term experiments were devised to study the lifetime of the catalyst after continuous additions. Figure 3.3.14 demonstrates the decaying activity of the catalyst after 1:1 additions of *p*-FA and NaOH. Figures 14-16 demonstrate attempts to prolong catalyst activity by modifying the quantity and rate of substrate additions, as well as cycling light.

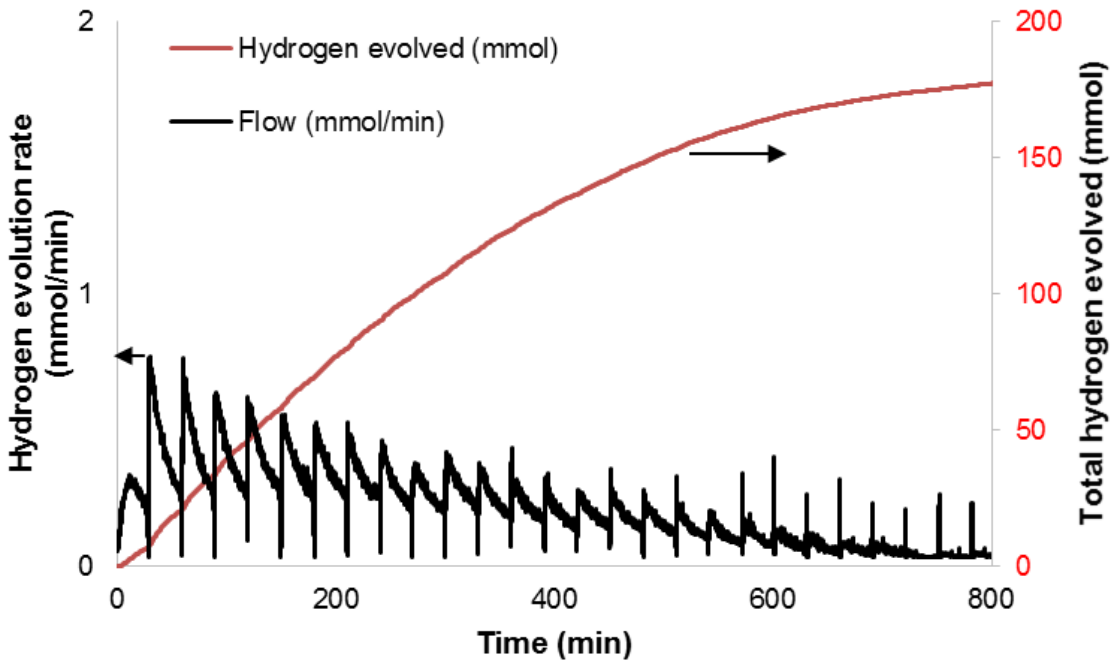

Figure 3.3.14. Rate of hydrogen formation and productivity of H_2 with regular additions of NaOH/*p*-FA over an extended time period. The reaction rate is visualized as a moving average trendline (n = 50, equivalent to 25 seconds) for clarity. The initial reaction mixture contained 50 mmoles *p*-FA, 250 mmoles NaOH and 0.5 mmoles of $Na_4Fe(CN)_6$. Every 30 minutes, 50 mmoles *p*-FA and 50 mmoles NaOH were added.

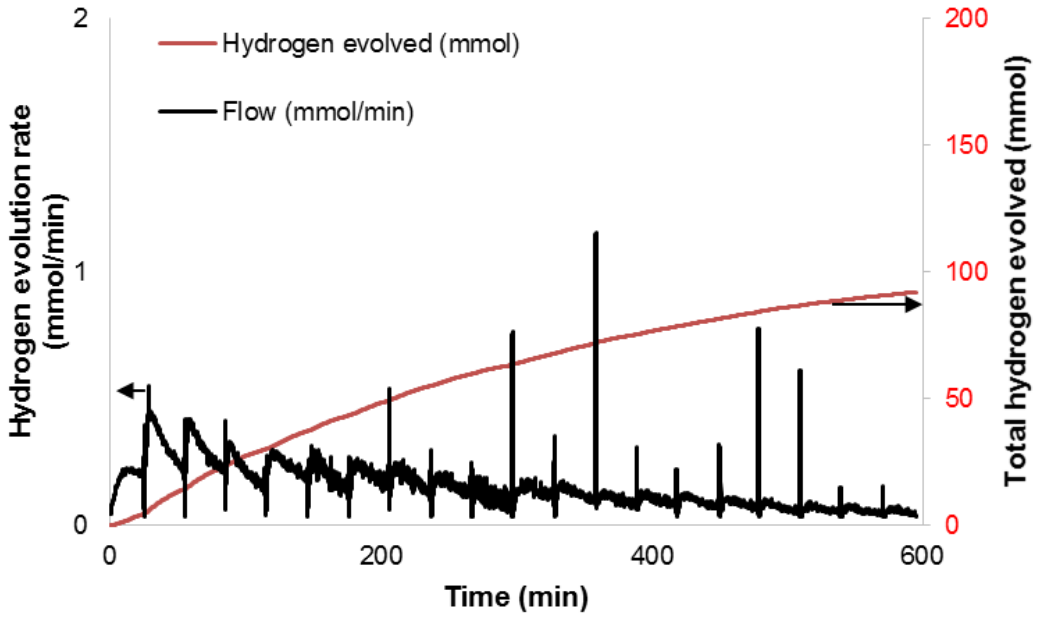

Figure 3.3.15. Rate of hydrogen formation and productivity of H_2 with regular additions of NaOH/*p*-FA over an extended time period with a 2:1 ratio of *p*-FA:NaOH. The reaction rate is visualized as a moving average trendline (n = 50, equivalent to 25 seconds) for clarity. The initial reaction mixture contained 50 mmoles *p*-FA, 250 mmoles NaOH and 0.5 mmoles of $Na_4Fe(CN)_6$. Every 30 minutes, 50 mmoles *p*-FA and 25 mmoles NaOH were added.

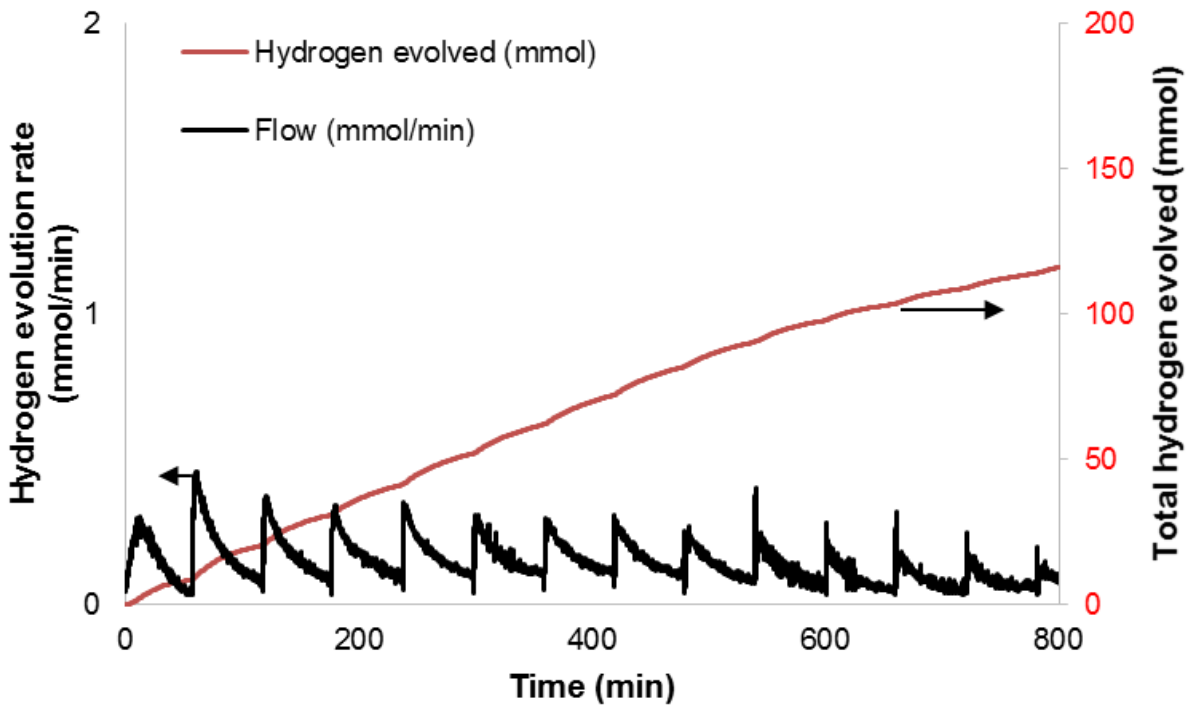

Figure 3.3.16. Rate of hydrogen formation and productivity of H_2 with regular additions of NaOH/*p*-FA over an extended time period with additions reduced to every hour. The reaction rate is visualized as a moving average trendline (n = 50, equivalent to 25 seconds) for clarity. The initial reaction mixture contained 50 mmoles *p*-FA, 250 mmoles NaOH and 0.5 mmoles of $Na_4Fe(CN)_6$. Every 60 minutes, 50 mmoles *p*-FA and 50 mmoles NaOH were added.

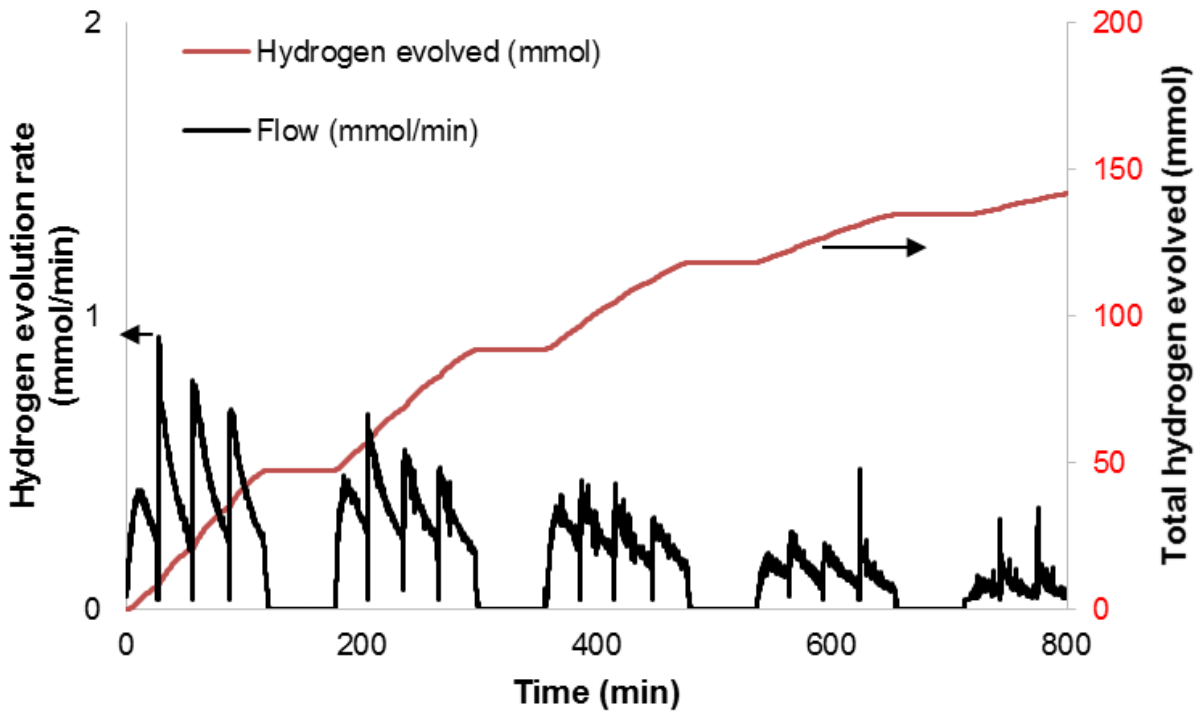

Figure 3.3.17. Rate of hydrogen formation and productivity of H_2 with regular additions of NaOH/*p*-FA over an extended time period with illumination shuttling between two hours on and one hour off. The reaction rate is visualized as a moving average trendline (n = 50, equivalent to 25 seconds) for clarity. The initial reaction mixture contained 50 mmoles *p*-FA, 250 mmoles NaOH and 0.5 mmoles of $Na_4Fe(CN)_6$. Every 30 minutes, 50 mmoles *p*-FA and 50 mmoles NaOH were added.

In all long-term reactions, the activity of the catalyst decayed, although the rate of deactivation changed for different reactions. After allowing the catalyst to react until gas evolution ceased (several days when adding 250 mmoles of *p*-FA and 500 mmoles of NaOH once per day), a brown precipitate formed in the reaction mixture. The precipitate was dried and analyzed by powder X-ray diffraction, which showed it to be a mixture of several iron oxides and hydroxides, in both iron(II) and iron(III) states.

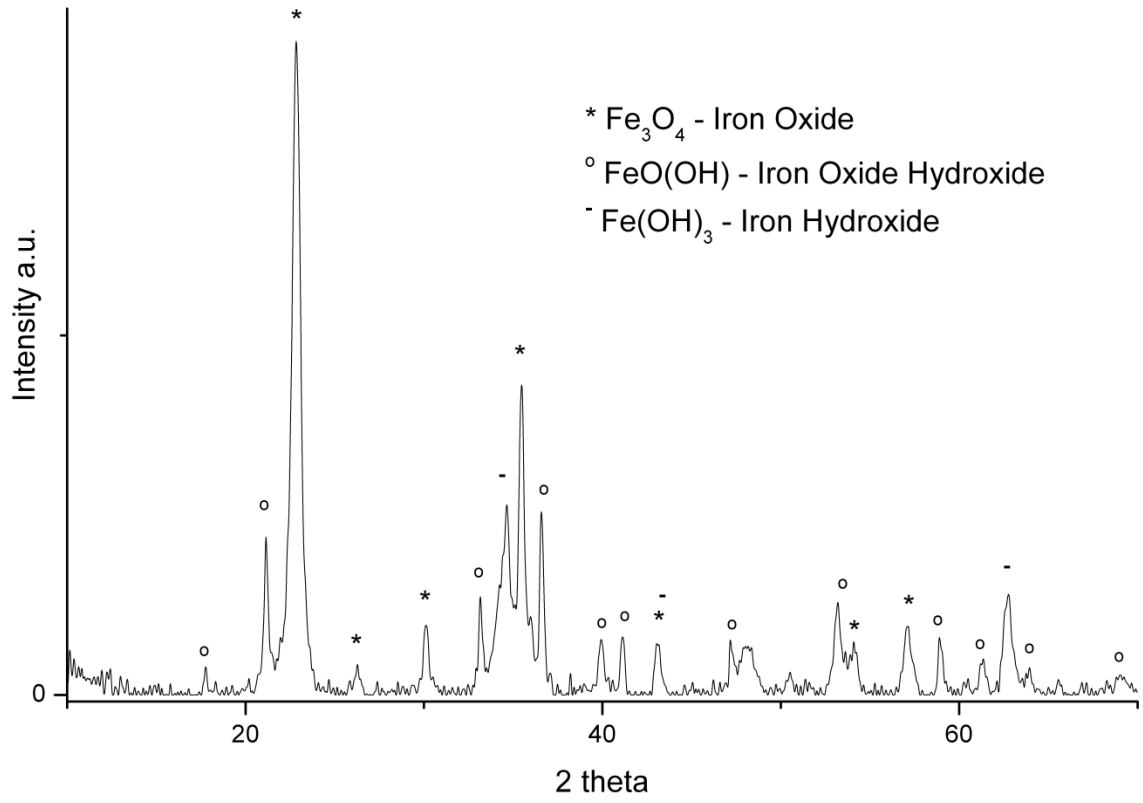

Figure 3.3.18. Powder X-ray diffraction (XRD) data for recovered precipitate. Precipitate is shown to be a heterogeneous mixture of at least three crystalline iron oxides.

In addition to catalyst death as detailed in Figure 3.3.18, the effect of potential side products in the reaction solution on catalytic activity was tested. Standard reactions were initiated without any addition of tested side products. After 15 minutes, sodium formate, methanol, sodium cyanide, or sodium cyanate was added to the reaction mixture to test the resulting activity of the catalyst.

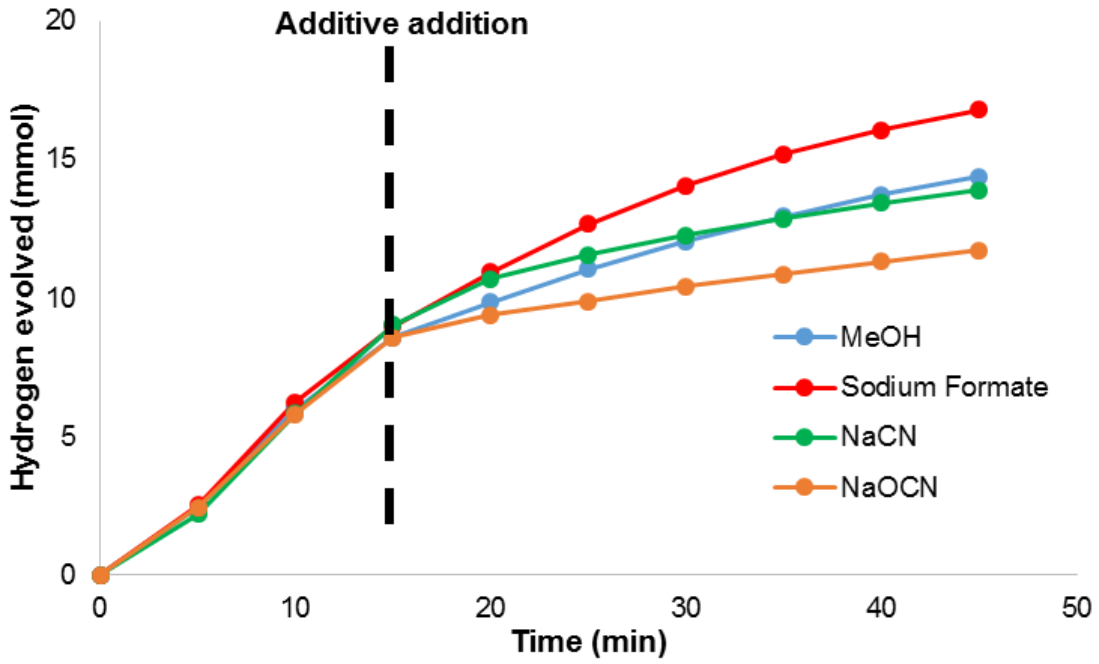

Figure 3.3.19. Effect of spiking standard dehydrogenation solution with potential side products and decomposition products. Initial reaction contains 250 mmoles NaOH, 50 mmoles *p*-FA and 0.5 mmoles $Na_4Fe(CN)_6$. After 15 minutes of illumination, a 5 mL aqueous solution containing one of 100 mmoles MeOH, 250 mmoles of sodium formate, 50 mmoles of NaOCN or 50 mmoles of NaCN were added to the solution to keep the concentration of formaldehyde and catalyst identical between the spiked samples.

3.4 Discussion

Formaldehyde dehydrogenation with iron-cyanide is limited to the iron(II) salts. When placed in NaOH, dehydrogenation with $Fe(CN)_6^{4-}$ is not limited to sodium salts. Both sodium and potassium salts of ferrocyanide appear to be equally active, while activity is reduced for other non-transition metal cations we tested, including calcium and bismuth. Transition metal cations form colloidal complexes analogous to Prussian Blue ($Fe_4[Fe(CN)_6]_3$) and show trace activity towards *p*-FA dehydrogenation.

However, cations do also plays a role in base selection. While the cause for this discrepancy is unknown, it may be due to effect of ionic environment on the pKa of methanediol. When studied in 1M solutions including Li^+, Na^+ and K^+, the pKa of methanediol is at a minimum in Na^+ solutions (13.05) while Li^+ and K^+ are notably greater (13.45 and 13.30, respectively).[13] The high pKa of methanediol may play a key role in the requirement for basic environments for dehydrogenation of formaldehyde. All non-hydroxide bases we tested provided zero activity towards dehydrogenation. This is not unexpected, as most nucleophilic bases are highly active towards methanediol and/or formaldehyde, or are unable to provide a sufficiently high pKa to deprotonate methanediol. Figure 3.3.10 demonstrates a similar effect as concentrated solutions of potassium halides are detrimental for dehydrogenation, although sodium halides have either no effect or a slightly beneficial one.

The Cannizzaro parasite reaction detracts this reaction in two ways. First, by removing some of the available formaldehyde from solution, the maximum yield of hydrogen is immediately reduced. Secondly, Figure 3.3.19 demonstrates the addition of methanol to have a detrimental effect on hydrogen evolution.

This problem is compounded by the native methanol present in both *p*-FA and methanediol solutions. Methanol-free solutions may be acquired by bubbling gaseous formaldehyde directly into an aqueous solution, although this was not tested (although the NaOH requirements will still produce MeOH via disproportionation).

An interesting property of the selective dehydrogenation of *p*-FA to formate salts provides an alternative (albeit unsustainable) method for the production of carbon monoxide. When concentrated sulfuric acid is added to the reaction mixture, formaldehyde dehydrogenation will halt, while formic acid decomposes into carbon monoxide and water. Interestingly, this reaction

does not decompose the catalyst, and subsequent addition of NaOH will restart the dehydrogenation reaction. One can envision the cycled addition of NaOH and sulfuric acid to alternatively and separately produce pure H_2 and CO from formaldehyde. While the stoichiometric addition of base and acid renders this reaction both unsustainable and likely industrially relevant, there may be applications for the laboratory production of both gases.

A promising aspect of ferrocyanide-catalyzed *p*-FA dehydrogenation is its stability in unclean conditions (Figure 3.3.9). The catalyst is similarly active in distilled water, salt water (at average ocean salinity), and dirty water from the downtown section of a canal. The light requirement is also flexible, as it is active with high intensity arc lamps, but also (albeit slowly) active in fluorescent lighting, sunlight and the light from a cell phone LED flashlight. The ability to harvest saltwater likely allows the catalyst to be active in sea water, which limits the stresses on fresh water, which would become an expensive and unsustainable option in large scale energy or industrial applications for H_2 production. Furthermore, the catalyst is entirely air stable, showing no signs of degradation when resting in air, or reactions without air purification.

The maximum measured catalytic activity is shown in Figure 3.3.12, with a TOF of 387 h^{-1}. To our knowledge, this is the highest TOF ever measured for formaldehyde dehydrogenation (see section 1.5 of this thesis). Unfortunately, this activity is not stable, as the catalyst activity quickly becomes wholly inactive after 300 minutes of regular additions of both NaOH and *p*-FA in a 5:1 ratio.

Figure 3.3.13 provides some insight into the decomposition of the catalyst. By reducing the NaOH:*p*-FA ratio of additions to 1:1, the maximum TOF is reduced (110 h^{-1}), although the activity is wholly stable through 300 minutes, at approximately 50 h^{-1}.The stable 50 h^{-1} is still greater than all but Ag nanoparticles on γ-Al_2O_3 described by Lu and Bi.[6] The only change

between the two reactions is the quantity of NaOH added every 30 minutes. With the assumption that for every mole of methanediol dehydrogenated, one mole of NaOH is required to deprotonate (and activate) the substrate, there will be a large excess of NaOH within a few additions. In very highly basic environments (pH $\geq$ 14), ferrocyanide is susceptible to photolysis and decomposition to $Fe(OH)_3$, as well as free cyanide and cyanate which are catalyst poisons (Figure 3.3.19).[14]

From a combination of prior literature on ferrocyanide and the photon dependence of this reaction (Figures 1 and 17), we are confident that the first step for dehydrogenation is the photosubstitution of cyanide for hydroxide. In addition, the pH dependence, effect of sodium vs potassium in metal hydroxides (Figures 8 and 10), and requirement for stoichiometric quantities of NaOH (Figure 3.3.6) suggest the deprotonation of methanediol is critical for catalyst activity. Unfortunately, any attempt to isolate or identify reactive intermediates by crystallization, *in situ* ESI-MS and *in situ* NMR have been unsuccessful. In every attempt to isolate and grow crystals, sodium ferrocyanide and sodium hydroxide were the only clearly identifiable compounds obtained. Finally, in NMR experiments, no changes in spectra were identified (beyond growth of formate and methanol peaks combined with reduction of methanediol peaks). Failure to detect any activity by NMR is not unexpected, as the rapid and photodependent nature of formaldehyde dehydrogenation makes it difficult to test by NMR.

Preliminary DFT calculations were performed to gather insight into possible reaction pathways (Figure 3.4.20). All atoms are retained for the entirety of the calculation, although some are omitted from the figure for clarity. The first step involves a 2.51 kcal/mol increase in energy, which is provided by the aforementioned photodissociation reaction. The next key intermediate appears to be the substitution of a hydroxyl ligand with deprotonated methanediol.

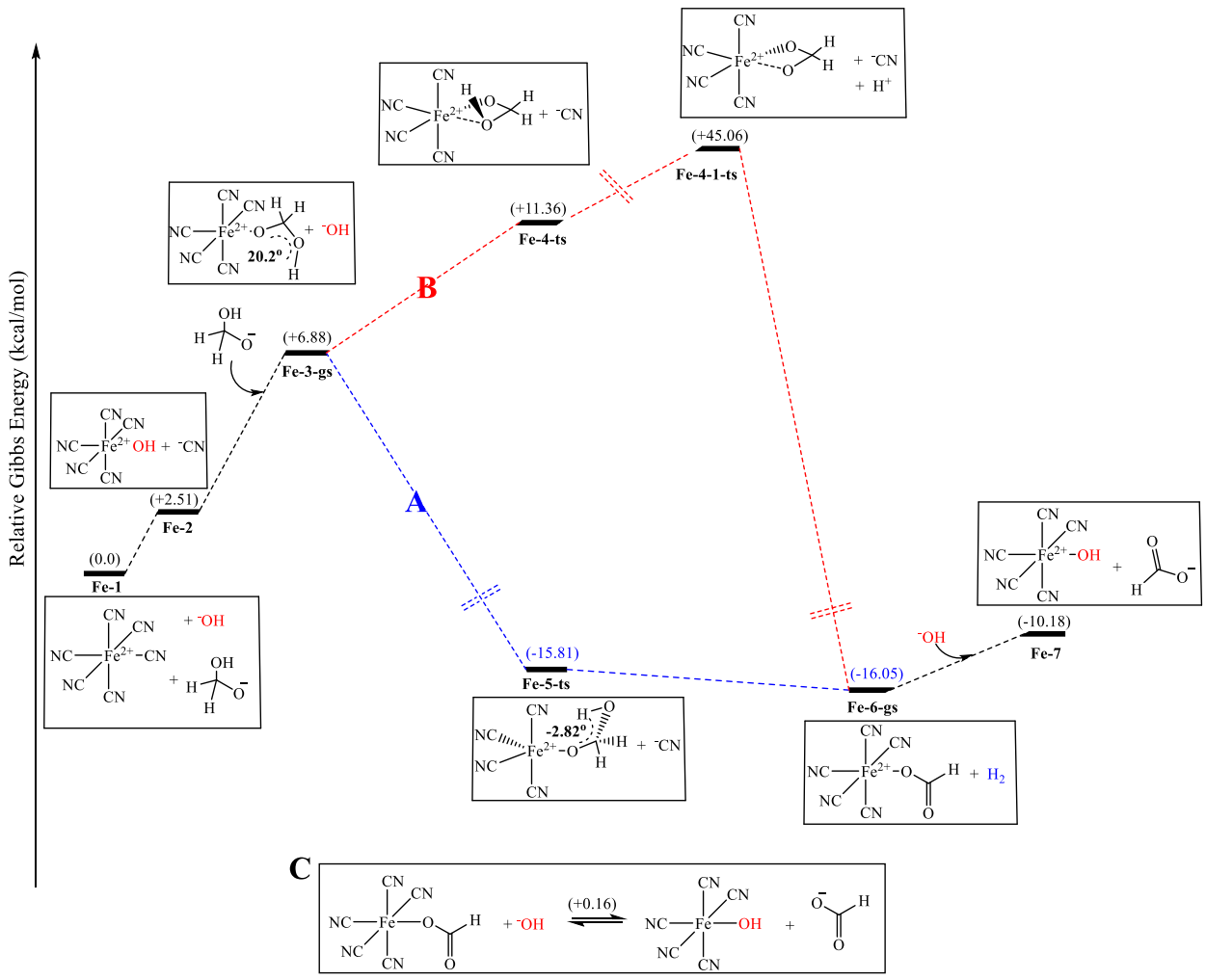

Figure 3.4.20. Preliminary energy profile calculated for dehydrogenation of formaldehyde with sodium hydroxide and ferrocyanide. The cycle is broken down into two possible pathways, A (blue) and B (red). C) DFT calculations describing the energy required to restart the catalytic cycle. B3LYP/TZVP was used for all atoms, and iron was presumed to be in oxidation state of 2+ for all calculations.

From the resulting intermediate, the catalytic cycle diverges into two pathways. In the most likely pathway (A), the next stable molecule, shown as Fe-5-ts, exists as a trigonal bipyrimidal with only 4 cyanide ligands. At some point in the reaction, a cyanide ligand temporarily

dissociates, and the O-C-O-H dihedral angle is -2.82° (as opposed to 20.2° in the previous intermediate). It is currently unknown if any external stimulus (possibly a second photon) is required to initiate this pathway. This transition state rapidly decomposes and picks up another cyanide ligand, releasing hydrogen in the process, while methanediol is oxidized to formate.

In pathway B, the release of a second cyanide ligand is maintained, although instead of forming a 5-coordinate trigonal bipyrimidal structure, the second hydroxide of methanediol coordinates with Fe^{2+}. A large increase in energy is required to deprotonate the coordinated hydroxide, releasing a proton. This transition state rapidly collapses, releasing hydrogen gas, re-coordinating the 5^{th} cyanide ligand, and producing formate. Due to the very large energy requirement for the second deprotonation of methanediol, and little external stimulus to push the reaction in this direction, this pathway is highly unlikely.

The full system, including hydrogen gas has an energy of -16.05 kcal per mol. In both pathways, after hydrogen is released from the system the formate ligand can readily interchange with hydroxide (Figure 3.4.2°C), restarting the catalytic system.

From our DFT calculations, suggesting pathway A as the most likely pathway, we can propose a simplified catalytic cycle (Figure 3.4.21), with methanediol and sunlight as the input, and formate and hydrogen as the only output.

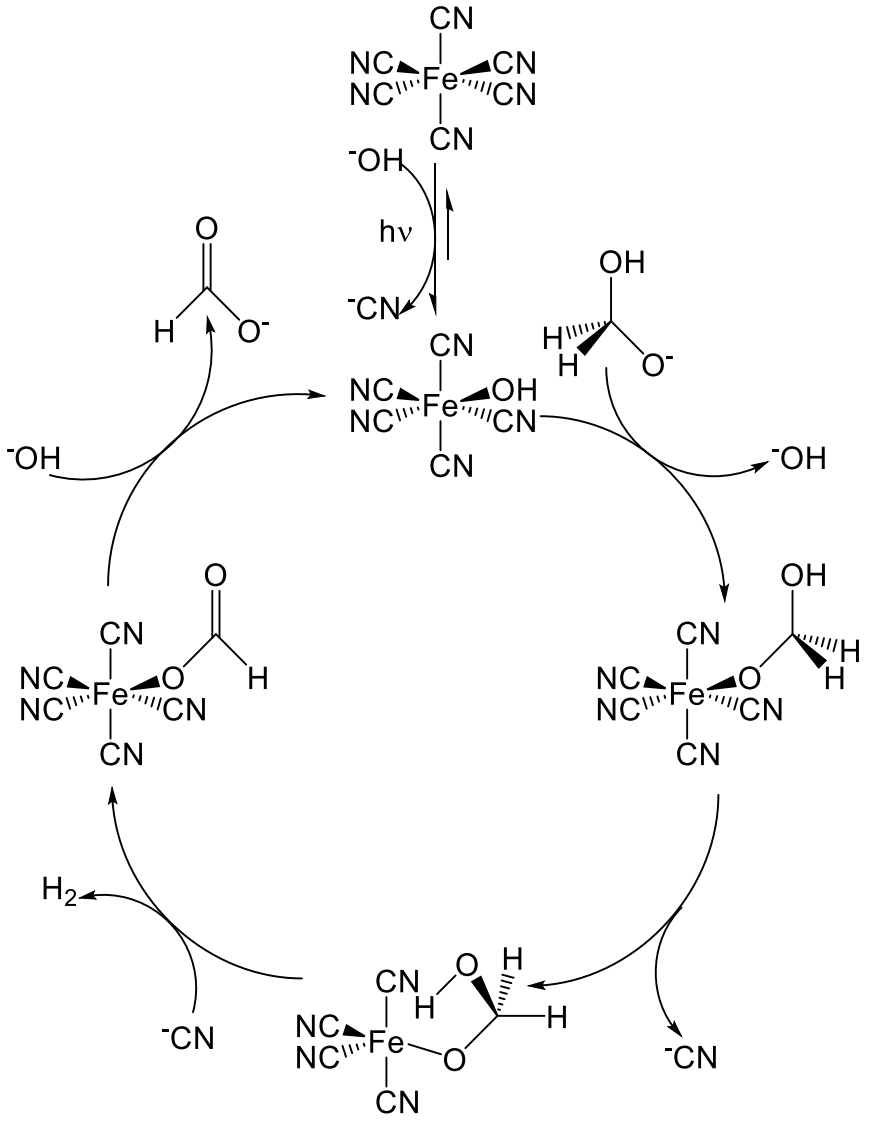

Figure 3.4.21. Proposed catalytic pathway for the dehydrogenation of methanediol.

3.5 Concluding remarks

In this work, we have reported an unprecedented homogeneous photocatalyst for the room temperature dehydrogenation of formaldehyde. The catalyst is capable of releasing pure H_2 without the use of any filters. The cheap, abundant, ferrocyanide catalyst is capable of producing turnover numbers in excess of 8000, and turnover frequencies of 387 h^{-1}, both of which are the highest recorded in the literature, to our knowledge.

The ability to selectively produce formate instead of CO_2, as seen in other homogeneous LOHC dehydrogenation systems, may benefit future attempts to provide overall water splitting using LOHCs as a storage medium and shuttle.

Further work to reduce the requirement of base, and further insights into mechanistic details of this catalyst are required to if using ferrocyanide (or similar catalysts) for formaldehyde dehydrogenation is to be industrially relevant for hydrogen production (or storage).

3.6 References

(1) Heim, L. E.; Schlörer, N. E.; Choi, J.-H.; Prechtl, M. H. G. *Nat. Commun.* **2014**, *5*, 3621.

(2) Suenobu, T.; Isaka, Y.; Shibata, S.; Fukuzumi, S. *Chem. Commun.* **2015**, *51*, 1670–1672.

(3) Bi, Y.; Lu, G. *Int. J. Hydrogen Energy* **2008**, *33*, 2225–2232.

(4) Bi, Y.; Hu, H.; Li, Q.; Lu, G. *Int. J. Hydrogen Energy* **2010**, *35*, 7177–7182.

(5) Hu, H.; Jiao, Z.; Ye, J.; Lu, G.; Bi, Y. *Nano Energy* **2014**, *8*, 103–109.

(6) Li, Y.; Chen, T.; Wang, T.; Zhang, Y.; Lu, G.; Bi, Y. *Int. J. Hydrogen Energy* **2014**, *39*, 9114–9120.

(7) Campos, J.; Sharninghausen, L. S.; Manas, M. G.; Crabtree, R. H. *Inorg. Chem.* **2015**, 150123093031007.

(8) Sleat, R.; Mah, R. a. *Appl. Environ. Microbiol.* **1984**, *47*, 884–885.

(9) Cooley, R. B.; Dubbels, B. L.; Sayavedra-Soto, L. a; Bottomley, P. J.; Arp, D. J. *Microbiology* **2009**, *155*, 2086–2096.

(10) Becke, A. *J. Chem. Phys.* **1993**, *98*, 5648–5652.

(11) Schäfer, A.; Huber, C.; Ahlrichs, R. *J. Chem. Phys.* **1994**, *100*, 5829–5835.

(12) Frisch, M. J. et al. Gaussian 09, Revision D.01, 2013.

(13) Norkus, E.; Pauliukaite, R.; Vaskelis, A. *J. Chem. Res.(S ...* **1998**, *4*, 320–321.

(14) Arellano, C. A. P.; Martinez, S. S. *Sol. Energy Mater. Sol. Cells* **2010**, *94*, 327–332.

Chapter 4: Conclusion and Future Work

4.1 Summary of Thesis Findings

The two sections of this thesis demonstrate a proof of concept for photochemical production of hydrogen from water via a formaldehyde-formate couple. In the hydrogen evolution half-reaction, ferrocyanide salts were observed to efficiently dehydrogenate formaldehyde into hydrogen and formate. This reaction is notable in the field of formaldehyde dehydrogenation for having 1) the greatest observed TOF (387 h^{-1} vs 113 h^{-1})[1], 2) the greatest calculated TON (8000 vs 346)[2], and 3) for using a widely available, and cheap, photocatalyst. Furthermore, the dehydrogenation of formaldehyde halts at formate, which provides an opportunity to develop carbon reduction catalysts which may skip the energetically unfavorable CO_2 reduction step.

In the second portion of this thesis, the mechanism for CO_2 photoreduction on $BiVO_4$ is examined. This work demonstrates, for the first time, the decomposition of both the reduction product (methanol into formaldehyde and formate) and the catalyst (etching of the surface and deposition of bismuth oxides). The two decay pathways demonstrates the lack of viability of using $BiVO_4$ in photochemical CO_2 reduction, as the combination of the catalyst and the product appears to cause the death of both. As a proof of concept to couple with formaldehyde dehydrogenation, $BiVO_4$ was capable of reducing sodium formate into methanol, which can be reoxidized into formaldehyde for use with ferrocyanide.

4.2 Future Work

Ferrocyanide-catalysed formaldehyde dehydrogenation should be further studied to understand the catalytic mechanism. The proposed mechanism in Chapter 3 was developed with little direct evidence. Due to the low NMR sensitivity of iron-cyanide, and inability to isolate crystals of

intermediates, it has been difficult to determine key structures in the catalytic cycle. Understanding the catalytic structure may provide insight into the requirement for high concentrations of NaOH, which may provide an opportunity to reduce the requirement for the stoichiometric addition of NaOH and reduce reaction costs and improve sustainability. Furthermore, the decay mechanism into iron oxide is not understood. Understanding the decay may provide an opportunity to protect ferrocyanide from decay and increase turnovers.

The formate reduction half reaction is currently very inefficient and requires much research. Focusing on $BiVO_4$, further insight into the CO_2 photoreduction mechanism can be elucidated. Precise time-resolved detection of CO_2 reduction can follow the production of organic products to determine if the reaction follows successive PCET reduction steps from CO_2 into methanol, or if an alternate pathway is preferred. The reaction rate of photoreduction will likely need to improve for sensitive time-resolved spectroscopy to be possible.

4.3 References

(1) Li, Y.; Chen, T.; Wang, T.; Zhang, Y.; Lu, G.; Bi, Y. *Int. J. Hydrogen Energy* **2014**, *39*, 9114.

(2) Heim, L. E.; Schlörer, N. E.; Choi, J.-H.; Prechtl, M. H. G. *Nat. Commun.* **2014**, *5*, 3621.